Fermi National Accelerator Laboratory

FN-470

Analytical and Numerical Studies of the Landau Cavity

Longitudinal Coupled Bunch Instabilities in the Fermilab Booster

Yu-Chiu Chao and King-Yuen Ng
Fermi National Accelerator Laboratory
P.O. Box 500, Batavia, Illinois 60510

April 1988

FN-470

ANALYTICAL AND NUMERICAL STUDIES OF THE LANDAU CAVITY

LONGITUDINAL COUPLED BUNCH INSTABILITIES IN THE FERMILAB BOOSTER

Yu-Chiu Chao and King-Yuen Ng

Fermi National Accelerator Laboratory, Batavia, IL 60510*

(April 1988)

*Operated by the Universities Research Association Inc., under contracts with the U. S. Department of Energy.

ABSTRACT

Analytical initial-value method is used to study the growth of longitudinal coupled bunch instability in the Fermilab Booster, both under ordinary harmonic potential and Landau cavity potential. A general result is given for any resonance mode. The numerical evaluation is done using computer programs developed especially for such a purpose. The merit of the Landau cavity is discussed.

CONTENTS

1 Introduction

In this note we will discuss the result of our attempt to understand the coupled bunch instability[1] currently observed in the Fermilab Booster, as well as to evaluate possible cure by using Landau cavity. In the following we briefly describe the motivation for the study, the techniques used, the results and comments.

1.1 Longitudinal coupled bunch instability in the Fermilab Booster

With the development of the Tevatron project in Fermilab aimed at colliding beam experiments, emphasis has been given to luminosity requirements of the beams. This in turn made important the limitation on the beam size in both the Booster and the Main Ring of Fermilab at high intensity. About ten bunches of protons are coalesced in the Main Ring to enhance the luminosity before injection into the Tevatron. A significant loss in this coalescing process due to the size of the individual bunches in the Main Ring led to a reduction in the luminosity in the Tevatron collider. To trace the origin of the large bunch area coming out of the Booster, a series of experiments have been carried out. Since these will serve as the basis of our later analysis, we elaborate on them in the following (The names mentioned below do not exhaust all the experimenters involved in these studies.) :

Figure 1-1 shows the measurements done by Crisp[2] showing an increase in the Booster bunch area right after transition. This is partly due to space charge effects[3]. Figure 1-2(a) shows the equilibrium bunch length with and without space charge for the Booster, where η_0 is the ratio of space charge force to the linearized rf force, θ is the normalized bunch length in rf radian, and x is normalized time with transition at $x = 0$. For a bunch having the right equilibrium bunch length before transition, the bucket becomes too short after transition, and the bunch length starts executing oscillations about the equilibrium position as shown in Figure 1-2(b). This is essentially a quadrupole oscillation and can be seen from the mountain range pictures of Figure 1-3(a). This "bunch tumbling" is practically eliminated with the installation of the γ_t-jump system in the Fermilab Booster (Figure 1-3(b)). The elimination of the quadrupole oscillations helped highlighting the dipole mode of the longitudinal coupled bunch instability, as is clearly visible in Figure 1-3(b). A further set of measurements was carried out by Cornacchia and Crisp [4] to identify the cause of the large beam size. The transverse beam size was measured with a flying wire and, at the same time, the bunch length was also measured with the longitudinal pick-up. Figure 1-4 shows the measured beam half size as a function of time in the acceleration cycle. Four of the 18 rf cavities were disconnected but not shorted. The beam intensity at high energies was 1.5×10^{12} protons for a total of 84 bunches. We observe an increase in beam size at transition ($\sim$19 msec after injection). We also observe that the horizontal beam size increases at high energies. The measured beam size is compared with the calculated value, obtained by adding quadratically the contribution of the momentum spread and the horizontal emittance. The momentum spread was inferred from the measured bunch length and the known rf parameters, while a normalized transverse emittance of 8π mm-mrad was assumed. The good agreement between the two curves indicates that, at this intensity, no betatron blow up occurs, and that the longitudinal instability only is responsible for the observed increase in beam size. The half

beam size was next measured with the four disconnected cavities shorted and is plotted in Fig. 1-5. The increase in beam size at high energies was reduced showing that the growth is driven by the rf cavities. The calculated bunch size assuming a constant normalized emittance of 8π mm-mrad and a constant bunch area of 0.025 eV-sec does not agree with the measured value. This demonstrates again that the discrepancy is due to an increase in bunch area at higher energies. Figure 1-6 shows the bunch area inferred from the measured bunch length as a function of time with four of the rf cavities shorted and also with the cavities unshorted. The growth in bunch area at high energies reveals clearly a longitudinal instability and that the cavities were responsible for the instability. We suspect that this is a longitudinal coupled-bunch instability driven by the parasitic modes of the cavities. Figure 1-7(a) shows the beam spectrum taken over the range up to the third harmonic of the rf frequency. Various peaks corresponding to the coupled bunch modes are clearly visible. Notice that due to the fact that the picture is taken by sweeping a "window" of finite band width over the whole range of the frequency in finite time, the relative amplitude among the peaks does not necessarily correspond to their real relative amplitude at a given time. We can also single out one mode and look at its behavior in the course of time by filtering out all the frequencies other than the one corresponding to this mode on the spectrum analyzer and sweeping this "window" of narrow bandwidth throughout the cycle. Figure 1-7(b) shows such a picture of the coupled bunch mode 16 (frequency 115 MHz) for the last 20 msec of the cycle. We can see an increase in amplitude near 22 msec. (The crossing time for this mode is 22.3 msec). Finally we show a series of measurements taken by Roland Garoby and Steve Holmes where, similar to the usual phase detection technique, a selectable integral multiple of the revolution frequency signal is used to sample the beam signal when the latter displays a coupled bunch mode with the selected mode number. The resulting signal displays a frequency equal to the difference of the two frequencies. This pattern is spectrally analyzed to determine the synchrotron mode. This also helps in determining more reliably the strengths of individual modes. As we can see from Figure 1-8, all coupled bunch modes are dominantly dipole modes with a typical sideband separation of 2000 Hz, the synchrotron frequency after transition in the Booster.

Figures 1-7 and 1-8 seem to indicate a real problem with mode 16 (or 68 since we have 84 bunches). The similar situation was observed in mode 31 (or 53) as can be seen from Figure 1-7(a). Table 1 lists 14 resonances of the rf cavities measured by Crisp.[5] The correct shunt impedances and Q's were calculated by taking the known shunt impedance and Q of the fundamental as a reference. We will refer to these resonances frequently by their serial numbers as appear in Table 1. These resonances will be crossed by one or more spectral lines as the particle is accelerated and coupled-bunch growth of some modes will be excited. Table 2 shows the average growth rate of each mode driven by the resonances, the principal one being bold-faced. However, the two modes mentioned above were the most important ones. We conjecture that only resonances number 2 and 4 have been crossed by the spectral lines therefore exciting modes near 16 and 53. The frequencies of the other resonances increase as the rf cavities are tuned gradually to accommodate higher energies. As a result, these resonances may not be crossed by any spectral lines except near extraction where many other coupled modes have been observed. It was actually observed that resonances number 2 and

4 do not have their frequencies changed during acceleration.

1.2 Remarks on the calculational techniques

The purpose of our work is to first seek a reliable computational method which faithfully reflects the coupled bunch instability in the Fermilab Booster, and then use this method to study the effect of a Landau cavity. Our choice is a combination of analytic and numerical techniques aimed at optimizing the efficiency and accuracy of the outcome. We adopt Landau's celebrated treatment[6] of the singularities in the Vlasov equation. The dispersion relation is obtained while the system is treated with initial-value-problem techniques, namely, in obtaining the frequency domain representations of the quantities, contours in the integral transforms are so chosen that the growth is always zero before the onset of the disturbance. On the other hand, since the tune spread is of great interest in Landau cavity, we decide not to neglect this contribution in the dispersion relation, as opposed to the practice in some cases where tune spread is neglected due to its arguable insignificance and the problem is greatly simplified. In terms of actual calculation, this amounts to solving the analytically continued dispersion relation exactly. Our task is further complicated in the case of the Landau cavity because the degeneracy of different coupled bunch modes right in the beginning forbids one from singling out one special mode over the others as was pointed out by Krinsky and Wang.[7] The system has to be addressed as a self-coupled eigenvalue problem.

The fact that we solve the self consistent dispersion relation means that the exponential growth rate as a *multiplicative* factor at any instant is governed only by the impedance and a few other machine parameters, but not by the instantaneous magnitude of either the perturbed particle distribution or the perturbed voltage. Therefore the neglect (in fact lack of need) of these quantities at every point of our calculation is justified, the only relevant quantity being the exponential growth rate itself.

The treatment of the problem as an initial value problem everywhere in the whole time interval avoids the possible mistake which may result from a calculation in the frequency domain using Fourier transforms everywhere. The problem of the latter method is that the often non-negligible transient effects during the turn-on time is missed.[8] If a tracking simulation is pursued in such a manner, transient effects from both the previous turn and the current turn could be overlooked. Such is the problem facing, for example, an ESME calculation, where the sum over contributions from previous revolutions is not properly reflected in the voltage seen by the particle. This is important when the growth time is long enough to demand accurate evaluation of the transient effects. (We were informed of plans to add features that account for such effects in the ESME code.[9]) The use of Laplace transform in the calculation presented in this paper ensures the absence of this worry. The Fourier transform used in Eq. (2.14) and later equations below in Section 2.1 are just mathematical intermediate steps, the inverse Fourier transform being performed later in Eq. (2.34) along the causal contour with the correct pole structure of $Z(\omega)$ as indicated in the same section.

We attempt to follow the analytical treatment outlined above. Simplifications are still possible and desired whenever made judicially. We then leave the actual solution, both for the normal harmonic cavity and for Landau cavity to numerical algorithms outlined in detail

in Section 3-1 and Appendix A.

One merit of our approach is the speed, since a large part of it is done analytically and special attention is paid to speeding up the numerical process. This is reflected in the fact that the calculation needed for the growth rate in harmonic rf potential throughout the latter half cycle (calculated at 1500 points) takes about 40 CPU seconds on a VAX 8650. The case for the Landau cavity takes considerably more time due to the absence of equivalent mathematical simplifications. (See Section 3-1 and Appendix A) But even in this case the calculation is done at a reasonable expense of CPU time.

1.3 Remarks on the result

The result of this work is detailed in Sections 3 and 4. The sharp-peak nature of the parasitic resonances puts a limit on the effectiveness of the Landau cavity. We see in cases where Eq. (4.6) is satisfied Landau cavity cuts down the growth significantly. But the typical impedances and Q's in the Booster do not always lead to such cases. Our conviction is that the merit of the Landau cavity would have been better realized if the impedances were either lower or higher. This seems to be supported by the simulations we show near the end of Section 4. We believe a Landau cavity would have been more effective also in the case of broad band impedances. The above argument however does not intend to categorically preclude the use of Landau cavities in the Fermilab Booster, as some resonances do satisfy Eq.(4.6) and are suppressed by Landau cavities. In the event of actual implementation, studies of the major offending resonances on a mode by mode basis with various realizations of the Landau cavity should be performed. The techniques developed here should be well suited for such a task.

2 Analytical Treatment

The purpose of the two following sections is to derive the dispersion relations for the longitudinal motion in the presence of driving resonances, under the harmonic or the quartic (Landau) potentials. Readers uninterested in technical details should proceed directly to the dispersion relations (2.44) in Section 2-1 and (2.79) in Section 2-2.

2.1 The Harmonic Cavity

We begin by considering the Fermilab Booster with parameters as listed in Table 3. Now for a particle arriving ahead of the synchronous one by a time τ we have

$$\frac{d\tau}{ds} = -\frac{R}{v^2}\frac{\eta\omega_0}{\beta^2}\delta = -\frac{\eta}{\beta^3 c}\delta, \tag{2.1}$$

where $\delta = \Delta E/E$ is the fractional energy deviation from the synchronous particle, η is the frequency dispersion factor and ω_0 the revolution frequency. We also have the other equation of motion

$$\frac{d\delta}{ds} = g(\tau),$$

where

$$g(\tau) = \frac{\omega_s^2 \beta}{\eta c} \tau$$

is the unperturbed longitudinal linear restoring force, ω_s being the synchrotron frequency.

Defining

$$\overline{\tau} = -\frac{\beta^3 c}{\eta} \tau$$

we get

$$\frac{d\overline{\tau}}{ds} = \delta.$$

Then $\overline{\tau}$ and δ become canonical variables in the Hamiltonian which reads

$$H = \frac{\delta^2}{2} + \frac{\beta^3 c}{\eta} \int^{\tau} g(\tau') d\tau' \tag{2.2}$$

If we take $\Psi(s, \tau, \delta)$ as the particle distribution for one bunch, Vlasov equation becomes

$$\frac{\partial \Psi}{\partial s} + \frac{d\overline{\tau}}{ds} \frac{\partial \Psi}{\partial \overline{\tau}} + \frac{d\delta}{ds} \frac{\partial \Psi}{\partial \delta} = 0$$

or

$$\frac{\partial \Psi}{\partial s} - \frac{\eta \delta}{\beta^3 c} \frac{\partial \Psi}{\partial \tau} + g(\tau) \frac{\partial \Psi}{\partial \delta} = 0. \tag{2.3}$$

At this point we need to look at the undisturbed particle distribution. If we take the distribution in δ-space to be a gaussian one

$$\Psi(\delta, \tau) = \frac{1}{\sqrt{2\pi}\sigma_\delta} e^{-\delta^2/2\sigma_\delta^2} \rho(\tau), \tag{2.4}$$

then in the steady state case,

$$\rho(\tau) = A_0 \exp\left[-\frac{\beta^3 c}{\eta \sigma_\delta^2} \int_0^{\tau} g(\tau') d\tau' \right], \tag{2.5}$$

where A_0 is subject to the normalization

$$\int \rho(\tau) d\tau = N.$$

In the presence of longitudinal impedance we have an extra term for $g(\tau)$

$$g(\tau) = \frac{\omega_s^2 \beta}{\eta c} \tau - \frac{eV(\tau)}{T_0 \beta c E}, \tag{2.6}$$

where $V(\tau)$ and T_0 are the voltage induced by the longitudinal impedance and the revolution period respectively. Using the explicit form (2.6) the Vlasov equation (2.3) becomes

$$\frac{\partial \Psi}{\partial s} - \frac{\eta \delta}{\beta^3 c} \frac{\partial \Psi}{\partial \tau} + \frac{\omega_s^2 \beta \tau}{\eta c} \frac{\partial \Phi}{\partial \delta} - \frac{eV(\tau)}{T_0 \beta c E} \frac{\partial \Psi}{\partial \delta} = 0. \tag{2.7}$$

In the following we will use interchangeably the coordinates (τ, δ) and the action-angle

coordinates (r,φ) according to

$$\tau = r\cos\varphi,$$
$$\frac{\eta}{\beta^2\omega_s}\delta = r\sin\varphi \tag{2.8}$$

where φ is the azimuthal angle in the longitudinal phase space of the bunch. Equation(2.7) becomes

$$\frac{\partial\Psi}{\partial s} + \frac{\omega_s(r)}{\beta c}\frac{\partial\Psi}{\partial\varphi} - \frac{eV}{T_0\beta cE}\frac{\partial\Psi}{\partial\delta} = 0$$

and, after the standard procedure of linearizing,

$$\frac{\partial\Psi_1}{\partial s} + \frac{\omega_s(r)}{\beta c}\frac{\partial\Psi_1}{\partial\varphi} - \frac{e\eta V}{T_0\beta^3 cE\omega_s}\sin\varphi\frac{d\Psi_0}{dr} = 0, \tag{2.9}$$

where Ψ_0 and Ψ_1 stand for the equilibrium and perturbed distributions respectively. Here we used the fact that $\Psi_0 = \Psi_0(r)$ only and note there is no $\partial\Psi_1/\partial r$ term in Eq. (2.9).

The remaining task until equation (2.24) is to construct the integral equation in the frequency domain for Ψ_1 by first establishing two independent relations between Ψ_1 and the wake potential $V(\tau)$: one from Vlasov equation and the other from considering the resonant interaction between the beam and the cavity impedances. Then $V(\tau)$ is eliminated from these two equations. To proceed, we make Laplace transformations on the quantities Ψ_1 and V while at the same time preserve the causal nature of the problem, namely, Ψ_1 and V should be zero before the onset of the instability, $s = 0$. This can be done by the Fourier decomposition of the synchrotron motion into various modes combined with a Laplace transformation in the time domain.

$$\tilde{R}_l(r,\omega) = \int_{-\pi}^{\pi}\frac{d\varphi}{2\pi}e^{-il\varphi}\int_0^\infty\frac{d(s/c)}{2\pi}e^{i\omega s/c}\Psi_1(r,\varphi,s)$$

$$\tilde{V}_l(r,\omega) = \int_{-\pi}^{\pi}\frac{d\varphi}{2\pi}e^{-il\varphi}\int_0^\infty\frac{d(s/c)}{2\pi}e^{i\omega s/c}V(r,\varphi,s)\sin\varphi \tag{2.10}$$

We grouped V with a $\sin\varphi$ here for later convenience. The inverse Laplace transformations for $\tilde{R}_l$ and $\tilde{V}_l$ are

$$R_l(r,s) = \int_W d\omega e^{-i\omega s/c}\tilde{R}_l(r,\omega),$$
$$V_l(r,s) = \int_W d\omega e^{-i\omega s/c}\tilde{V}_l(r,\omega) = \int_{-\pi}^{\pi}\frac{d\varphi}{2\pi}e^{-il\varphi}V(r,\varphi,s)\sin\varphi. \tag{2.11}$$

The integration path W is taken so that it traverses the complex plane above all poles of R_l or V_l and the real axis as depicted in Figure 2-1. From Eqs. (2.10) and (2.11) we can see the following:

The values of $R_l(r,s)$ and $V_l(r,s)$ (and therefore $\Psi_1(r,\varphi,s)$ and $V(r,\varphi,s)$) do go to zero when $s < 0$, which is desired.

The values of $\tilde{R}_l(r,\omega)$ and $\tilde{V}_l(r,\omega)$ are undefined by this transformation for $Im(\omega) < 0$ due to the integration range. Their values have to be obtained through analytic continuation across the real axis in the ω-plane.

Now let us look into the structure of the potential $V(\tau, s)$. It is the voltage induced in the ring through the wake potential $W(\tau)$ by previous passages of the beam,[10]

$$V(\tau, s) = eL \int_{-\infty}^{\infty} d\tau' \int_{-\infty}^{\infty} d\delta' \Psi_1(\tau', \delta', s) W(\tau' - \tau), \tag{2.12}$$

where we show the voltage seen by a test particle ahead of the synchronous particle by τ, due to the preceding particles averaged over one revolution. Notice only the perturbative part is considered. L is the length of the structure which generates the wake field. Note here we demand $W(\tau) = 0$ for $\tau < 0$. Equation (2.12) can be taken as the definition of the wake potential. If we are looking at long range wake field effects, with all the previous turns affecting the induced voltage, we have

$$V(\tau, s) = eL \int_{-\infty}^{\infty} d\tau' \sum_k \int d\delta' \Psi_1(\tau', \delta', s - vkT_0) W(kT_0 + \tau' - \tau), \tag{2.13}$$

where the sum goes over all turn numbers k, with corresponding displaced variables $s \to s - vkT_0$ and $\tau' \to kT_0 + \tau'$. Note the causal nature is still kept since $W(\tau) = 0$ for $\tau < 0$.

It is worth noting that $W(\tau)$ is related to the usual complex impedance $Z(\omega)$ through

$$W(\tau) = \int \frac{d\omega}{2\pi L} Z(\omega) e^{-i\omega\tau}. \tag{2.14}$$

Note that $Z(\omega)$ defined in this way will inherit the causal property of $W(\tau)$ through its pole structures in the ω-plane. The example of a resonance at ω_c, $Z(\omega) = 1/\left[1 + i\left(\frac{\omega_c}{\omega} - \frac{\omega}{\omega_c}\right)\right]$, bears this structure.

Substituting Eqs. (2.10), (2.12), and (2.14) into Eq. (2.13) we get the following result (remembering the variables (τ, δ) and (r, φ) are used interchangeably):

$$V(\tau, \omega) = \int_0^{\infty} \frac{ds/c}{2\pi} e^{i\omega s/c} V(\tau, s) \sin\varphi$$

$$= e \int_{-\infty}^{\infty} d\tau' \int d\delta' \int_0^{\infty} \frac{ds/c}{2\pi} \sum_{kl'} R_{l'}(r', s - vkT_0) \sin\varphi \int \frac{d\omega'}{2\pi} Z(\omega') e^{il'\varphi'} e^{i\omega s/c} e^{-i\omega'(kT_0 + \tau' - \tau)}. \tag{2.15}$$

Since $R_l(r, s) = 0$ for $s < 0$, we can extend the lower limit of the ds/c integration from 0 to $-\infty$.

$$V(\tau, \omega) = e \int_{-\infty}^{\infty} d\tau' \int d\delta' \sum_{kl'} \tilde{R}_{l'}(r', \omega) e^{i\omega V k T_0/c} \sin\varphi \int \frac{d\omega'}{2\pi} Z(\omega') e^{il'\varphi'} e^{-i\omega'(kT_0 + \tau' - \tau)}. \tag{2.16}$$

using

$$\frac{1}{2\pi} \sum_k e^{ikT_0(\omega v/c - \omega')} = \frac{1}{T_0} \sum_p \delta(\omega' - \omega v/c - 2\pi p/T_0). \tag{2.17}$$

We get

$$V(\tau, \omega) = \frac{e}{T_0} \int_{-\infty}^{\infty} d\tau' \int d\delta' \sum_{l'} \sum_p e^{il'\varphi'} \tilde{R}_{l'}(r', \omega) Z(\omega(v/c) + p\omega_0) e^{-i(\omega v/c + p\omega_0)(r' \cos\varphi' - \tau)}. \tag{2.18}$$

Equation (2.18) gives the expression if there is only one bunch in the ring. For multibunch cases with M equal bunches spaced T_0/M in time from each other, we need to replace τ by $(\tau - kT_0/M)$ and multiply each contribution by a phase factor $e^{2\pi iks/M}$ where $k = 1, 2, ...M$ and s is the coupled-bunch mode number, and then sum over k. The net effect of the above is to dilute the sum over p in Eq. (2.18) by M times and a multiplication of M:

$$\tilde{V}_l(r,\omega) = \int_{-\pi}^{\pi} \frac{d\varphi}{2\pi} e^{-il\varphi} V(\tau,\omega) =$$
$$\frac{eM}{T_0} \int_{-\infty}^{\infty} d\tau' \int d\delta' \sum_{l'} \sum_{p} \int \frac{d\varphi}{2\pi} e^{-il\varphi + il'\varphi'} \tilde{R}_{l'}(r',\omega) \sin\varphi Z(\omega_p) e^{-i\omega_p(r'\cos\varphi' - \tau\cos\varphi)} \tag{2.19}$$

where $\omega_p = \frac{\omega v}{c} + p\omega_0$, and

$$\sum_p = \sum_{j=-\infty, p=Mj+s}^{\infty}.$$

Remembering that

$$\frac{\eta}{\beta^2\omega_s} d\tau d\delta = r dr d\varphi$$

we have from Eq. (2.19)

$$\tilde{V}_l(r,\omega) = \frac{2\pi e\beta^2\omega_s M}{\eta T_0} \int_0^{\infty} r' dr' \sum_{l'} \sum_{p} \tilde{R}_{l'}(r',\omega)$$
$$\otimes Z(\omega_p) \int \frac{d\varphi}{2\pi} e^{-il\varphi + i\omega_p r\cos\varphi} \sin\varphi \int \frac{d\varphi'}{2\pi} e^{il'\varphi' - i\omega_p r'\cos\varphi'} \tag{2.20}$$

Integrating over φ and φ' using

$$\frac{1}{2\pi} \int_{-\pi}^{\pi} d\varphi e^{il\varphi - ix\cos\varphi} = i^{-l} J_l(x) \tag{2.21}$$

where $J_l(x)$ is the Bessel function, we get

$$\tilde{V}_l(r,\omega) = \frac{2\pi e\beta^2\omega_s M}{\eta T_0} \int_0^{\infty} r' dr' \sum_{l'} \sum_{p} \tilde{R}_l(r',\omega)$$
$$\otimes \frac{Z(\omega_p)}{\omega_p} \frac{(-l) i^{l-l'}}{r} J_l(\omega_p r) J_{l'}(\omega_p r'). \tag{2.22}$$

Now we can try to use the result we have gotten so far. We multiply the whole Eq. (2.9) by

$$e^{-il\varphi} e^{i\omega s/c}$$

and integrate over

$$\int_{-\pi}^{\pi} \frac{d\varphi}{2\pi} \int_0^{\infty} \frac{ds/c}{2\pi}$$

and use Eq. (2.22). After lengthy but straightforward manipulations, we get

$$\tilde{R}_l(r,\omega) = \frac{1}{\omega - \frac{l\omega_s}{\beta}}\left[iR_{l0}(r) + \frac{ie^2\omega_0 M}{\beta T_0 E}\frac{\Psi_0'(r)}{r}\sum_p\sum_{l'}(-li^{l-l'})\right.$$

$$\left.\otimes\int_0^\infty r'dr'\tilde{R}_{l'}(r',\omega)J_l(\omega_p r)J_{l'}(\omega_p r')\frac{Z(\omega_p)}{\omega_p}\right] \tag{2.23}$$

where

$$R_{l0}(r) = \int\frac{d\varphi}{(2\pi)^2}e^{-il\varphi}\Psi_1(r,\varphi,0) \tag{2.24}$$

where $\Psi_1(r,\varphi,0)$ is the perturbed distribution at $t=0$.

This is actually an eigenvalue problem with the dimensionality equal to the number of possible values for the index l, which is countably infinite. We cannot solve such a problem exactly. However, we notice that if we ignore the usually small coupling between modes with different absolute values of l, for example, coupling between dipole and quadrupole modes, we can reduce the problem to one consisting of many eigenvalue problems each corresponding to a finite dimensional space approximately decoupled from each other. In the following we will limit ourselves to such practice. To go further, we need to use small bunch approximation, namely

$$J_{-l}(z) \simeq (-1)^l\frac{1}{l!}(\frac{z}{2})^l$$

$$J_l(z) \simeq \frac{1}{l!}(\frac{z}{2})^l \tag{2.25}$$

for small z and positive integer l. In the small bunch case we need to retain only the lowest synchrotron modes. These are the $l=1$ and $l=-1$ modes. Thus Eq. (2.23) becomes

$$\tilde{R}_l(r,\omega) = \frac{1}{\omega - \frac{l\omega_s}{\beta}}\left[iR_{l0}(r) - \frac{ie^2\omega_0\Psi_0'(r)M}{4\beta T_0 E}\sum_p\sum_{l'=\pm1}l'i^{l-l'}\omega_p Z(\omega_p)\int_0^\infty r'^2dr'\tilde{R}_{l'}(r',\omega)\right] \tag{2.26}$$

Multiplying Eq. (2.26) by r^2 and integrating over dr, we get

$$\tilde{R}_l(\omega) = \Phi_l(\omega) - iA\sum_{l'}\int\frac{\Psi_0'r^2dr}{\omega_\beta - l\omega_s}l'i^{l-l'}\tilde{R}_{l'}(\omega) \tag{2.27}$$

where

$$\Phi_l(\omega) = \int_0^\infty drr^2\frac{iR_{l0}(r)}{\omega - \frac{l\omega_s}{\beta}}$$

$$\tilde{R}_l(\omega) = \int_0^\infty drr^2\tilde{R}_l(r,\omega)$$

$$A = \frac{e^2\omega_0 M}{4T_0 E}\sum_p\omega_p Z(\omega_p).$$

Note $\sum_p$ still follows the definition given in Eq. (2.19). Equation (2.27) can be put in the following form by considering the 2-space spanned by the two modes $l = 1$ and $l = -1$

$$\begin{pmatrix} 1 + iA\int \frac{\Psi_0' r^2 dr}{\omega\beta - \omega_s} & iA\int \frac{\Psi_0' r^2 dr}{\omega\beta - \omega_s} \\ -iA\int \frac{\Psi_0' r^2 dr}{\omega\beta + \omega_s} & 1 - iA\int \frac{\Psi_0' r^2 dr}{\omega\beta + \omega_s} \end{pmatrix} \begin{pmatrix} \tilde{R}_1(\omega) \\ \tilde{R}_{-1}(\omega) \end{pmatrix} = \begin{pmatrix} \Phi_1(\omega) \\ \Phi_{-1}(\omega) \end{pmatrix} . \tag{2.28}$$

Let

$$S_\pm = \int \frac{\Psi_0' r^2 dr}{\omega\beta \pm \omega_s}.$$

The above equation can be written

$$\mathcal{A}\mathcal{R} = \Phi \tag{2.29}$$

or

$$\begin{pmatrix} 1 + iAS_- & iAS_- \\ -iAS_+ & 1 - iAS_+ \end{pmatrix} \begin{pmatrix} \tilde{R}_1(\omega) \\ \tilde{R}_{-1}(\omega) \end{pmatrix} = \begin{pmatrix} \Phi_1(\omega) \\ \Phi_{-1}(\omega) \end{pmatrix} . \tag{2.30}$$

We want to find the eigensolutions for this system by diagonalizing the matrix $\mathcal{A}$. The eigenvalues λ can be found to be

$$\lambda = \begin{cases} 1 \\ 1 + iA(S_- - S_+) \end{cases} \tag{2.31}$$

and the diagonalized form of Eq. (2.30) is

$$\begin{pmatrix} 1 & 0 \\ 0 & 1 + iA(S_- - S_+) \end{pmatrix} \begin{pmatrix} -S_+\tilde{R}_1 - S_-\tilde{R}_{-1} \\ \tilde{R}_1 + \tilde{R}_{-1} \end{pmatrix} = \begin{pmatrix} -S_+\Phi_1 - S_-\Phi_{-1} \\ \Phi_1 + \Phi_{-1} \end{pmatrix} \tag{2.32}$$

where we dropped the arguments ω in the $\tilde{R}$'s and Φ's. The dispersion relation is contained in one of the above equations, to wit

$$[1 + iA(S_- - S_+)]\tilde{R}(\omega) = \Phi(\omega) \tag{2.33}$$

where

$$\tilde{R}(\omega) = \tilde{R}_1(\omega) + \tilde{R}_{-1}(\omega)$$
$$\Phi(\omega) = \Phi_1(\omega) + \Phi_{-1}(\omega).$$

Therefore we have for the perturbed particle distribution

$$R(s/c) = \int_W d\omega \tilde{R}(\omega) e^{-i\omega s/c} = \int_W d\omega \frac{\Phi(\omega) e^{-i\omega s/c}}{1 + iA(S_- - S_+)} \tag{2.34}$$

and finally we arrive at the dispersion relation for this eigenmode:

$$H(\omega) = 1 + iA(S_- - S_+) = 1 + iA\int_0^\infty \Psi_0'(r)r^2 dr \left(\frac{1}{\omega\beta - \omega_s} - \frac{1}{\omega\beta + \omega_s}\right) = 0. \qquad (2.35)$$

Note that our problem is defined so far only for $\mathrm{Im}(\omega) > 0$. If we want to investigate the behavior for $s > 0$ in Eq. (2.34), we need to analytically continue $H(\omega)$ across the real axis and down to $\mathrm{Im}(\omega) < 0$. This can be accomplished by

$$H(\omega) = 1 + iA\int_0^\infty \Psi_0'(r)r^2 dr \left(\frac{1}{\omega\beta - \omega_s} - \frac{1}{\omega\beta + \omega_s}\right) \qquad \text{for} \qquad \mathrm{Im}(\omega) > 0$$

$$H(\omega) = 1 + iA\int_0^\infty \Psi_0'(r)r^2 dr \left(\frac{1}{\omega\beta - \omega_s} - \frac{1}{\omega\beta + \omega_s}\right)$$

$$-2\pi A\left\{\left(\Psi_0'(r)r^2\frac{dr}{d\omega_s}\right)\Big|_{\omega_s(r)=\omega\beta} - \left(\Psi_0'(r)r^2\frac{dr}{d\omega_s}\right)\Big|_{\omega_s(r)=-\omega\beta}\right\}$$

$$\text{for} \qquad \mathrm{Im}(\omega) < 0 \qquad (2.36)$$

In the case of ordinary rf potential ω_s is related to r through

$$\omega_s(r) = \omega_{s0}\left[1 - s(hr\omega_0)^2\right].$$

$$s = \frac{1}{16}\frac{1+\Gamma^2}{1-\Gamma^2} \qquad (2.37)$$

where $\Gamma = \sin\varphi_s$ and φ_s is the rf phase of the synchronous particle. The spread in ω_s is due to the anharmonic part of the sinusoidal rf potential. Note here $hr\omega_0$ is in rf radian. Now we are in the position of finding out the expression for $\Psi_0'(r)$. The equilibrium distribution $\Psi_0(r)$ is given, for example, in Ref. 7.

$$\Psi_0(r) \sim e^{\omega_s^2\omega_0^2 r^2/2\sigma^2} \qquad (2.38)$$

(Our r carries a dimension of time and is related to the r in Ref. 7 by a factor of ω_0), where σ is the spread in revolution frequency and satisfies

$$\sigma = \omega_s\left(\frac{\sigma_\varphi}{h}\right)$$

where σ_φ is the bunch length in rf radian and h is the rf harmonic. Thus we have

$$\Psi_0(r) \sim e^{-(h\omega_0 r)^2/2\sigma_\varphi^2} = e^{-r^2/2r_0^2} \qquad (2.39)$$

After normalization

$$N = \int \Psi_0(\tau,\delta)d\tau d\delta$$

$$= \frac{\beta^2\omega_s}{\eta}\int \Psi_0(r,\varphi)rdrd\varphi$$

$$= \frac{\beta^2\omega_s}{\eta}2\pi\int \Psi_0(r)rdr \tag{2.40}$$

where N is the number of particles in one bunch, we get

$$\Psi_0(r) = \frac{\eta N}{2\pi r_0^2\beta^2\omega_s}e^{-r^2/2r_0^2}$$

$$r_0 = \frac{\sigma_\varphi}{h\omega_0} \tag{2.41}$$

Changing variable from r to $x = h\omega_0 r$ and define $x_0 = \sigma_\varphi$, Eq. (2.35) becomes for $\mathrm{Im}(\omega) > 0$

$$H(\omega) = 1 + iA\frac{1}{(h\omega_0)^2}\int_0^\infty \frac{d\Psi_0}{dx}x^2dx\left[\frac{1}{\omega\beta - \omega_s(x)} - \frac{1}{\omega\beta + \omega_s(x)}\right]$$

$$\Psi_0(x) = \frac{\eta N h^2\omega_0^2}{2\pi x_0^2\beta^2\omega_s}e^{-x^2/2x_0^2} \tag{2.42}$$

Further manipulations using Eq. (2.37) give

$$H(\omega) = 1 - i\frac{\overline{A}}{s}\int_0^\infty dx x^3 e^{-\frac{x^2}{2x_0^2}}\left(\frac{1}{y+x^2} - \frac{1}{y+2/s-x^2}\right) \tag{2.43}$$

where

$$\overline{A} = \frac{e^2N\eta\omega_0^2M}{16\pi^2E\sigma_\varphi^4\beta^2\omega_s^2}\sum_p \omega_p Z(\omega_p),$$

$$y = \frac{\omega\beta - \omega_{s0}}{s\omega_{s0}}.$$

Let us concentrate on ω near ω_s. As long as $|\omega - \omega_s| \sim s\omega_s$ or $y \ll 1$, ω is far from $-\omega_s$, or $y + (2/s) \gg 1$. In such cases there is negligible coupling between the $l = 1$ and $l = -1$ modes. Thus the second term in the integral in Eq. (2.43) can be dropped. Thus finally we arrive at the dispersion relation.

$$H(\omega) = 1 - i\frac{\overline{A}x_0^2}{s}I(z) \tag{2.44}$$

where

$$z = \frac{y}{x_0^2} = \frac{\omega\beta - \omega_{s0}}{s\omega_{s0}x_0^2}$$

The $I(z)$ is given by

$$I(z) = \int_0^\infty dx x^3 e^{-\frac{1}{2}x^2}\frac{1}{z+x^2} \tag{2.45}$$

or

$$I(z) = \begin{cases} 1 - \frac{z}{2} e^{z/2} E_1(z/2) & \text{for } \mathrm{Im}(\omega) > 0 \text{ and } \mathrm{Re}(\omega) \geq 0,\ \mathrm{Im}(\omega) \leq 0 \\ 1 - \frac{z}{2} e^{z/2} E_1(z/2) + i\pi z e^{z/2} & \text{for } \mathrm{Im}(\omega) < 0,\ \mathrm{Re}(\omega) < 0. \end{cases} \tag{2.46}$$

The analytic continuation is done in the spirit of Eq. (2.36). The structure of the complex mapping and the detail of the analytic continuation will be described in Section 3. Also in the above $E_1(z)$ defined by

$$E_1(z) = e^{-z/2} \int_0^\infty dt \frac{e^{-t}}{z/2 + t}$$

is known as the complex exponential integral. The result Eq. (2.44) and that of the following section Eq. (2.79) will serve as the starting point for our computer calculations.

Before leaving this section, we examine Eq. (2.34) for the behavior of the perturbed distribution in time domain. By enclosing the contour in the lower half plane, we obtain

$$R(s/c) = \sum_{m, H(\omega_m)=0} \left[e^{-i\omega_m t} \mathrm{Res} \left(\frac{\varphi(\omega)}{H(\omega)} \right) \Big|_{\omega=\omega_m} \right] \tag{2.47}$$

which means the complex frequency shift of the perturbation at this instant is given by the root(s) of $H(\omega) = 0$. We will single out the one root with the largest imaginary part, representing the largest growth. If this resonance is further sustained over a long period of time, the total growth over time of the perturbation is given by

$$\text{Growth} \sim e^{-\int Im(\omega_m(t))dt} \tag{2.48}$$

where $\omega_m(t)$ is the root with the largest imaginary part solved at time t.

2.2 The Landau Cavity

In the case of the addition of a higher harmonic cavity, often known as the Landau cavity, the rf voltage waveform is made as flat as possible in the vicinity of the acceleration phase ϕ_s in order to enhance the frequency spread induced within a bunch. To achieve this, it is not hard to see that a higher harmonic cavity with harmonic number n with respect to the rf frequency should have an amplitude kV_0 and an acceleration phase ϕ_n satisfying

$$\begin{aligned} nk \cos n\phi_n &= -\cos \phi_s \\ n^2 k \sin n\phi_n &= -\sin \phi_s \end{aligned} \tag{2.49}$$

In order to get Eq. (2.49), we enforced the conditions that the first and second derivatives of the total voltage vanish at the crossing point of the synchronous particle

$$V'(\phi) = 0 \qquad \text{at} \qquad \phi = 0$$

$$V''(\phi) = 0 \qquad \text{at} \qquad \phi = 0$$

where

$$V(\phi) = V_0[\sin(\phi + \phi_s) + k\sin(n\phi + n\phi_n)] \tag{2.50}$$

Equation (2.49) indicates that among the three higher harmonic parameters, one is arbitrary. We will choose it as n. expanding Eq. (2.50) around ϕ_s, using Eq. (2.49), we get

$$V(\phi) = V_0\left(\frac{n^2-1}{3!}\right)\phi^3\cos\phi_s = -V_0\left(\frac{n^2-1}{3!}\right)(h\omega_0)^3\tau^3\cos\phi_s \tag{2.51}$$

where τ is the time advance as defined in the previous section. We can again pursue the problem by using a Hamiltonian like the one in Eq. (2.2), but now with the restoring force $g(\tau)$ given by

$$g(\tau) = \frac{\omega_{s0}^2\beta\tau^3}{\eta c}\left(\frac{n^2-1}{3!}\right)(h\omega_0)^2 \tag{2.52}$$

in conformity with the change of $V(\phi)$ from the harmonic cavity form of $(\omega_{s0}^2\beta\tau)/\eta c$ to that of Eq. (2.51). Keeping the form of the Hamiltonian of Eq. (2.2) unchanged, we obtain the Vlasov equation using Eq. (2.52)

$$\frac{\partial\Psi}{\partial s} - \frac{\eta\delta}{\beta^3 c}\frac{\partial\Psi}{\partial\tau} + \frac{\omega_{s0}^2\beta(n^2-1)(h\omega_0)^2}{3!\eta c}\tau^3\frac{\partial\Psi}{\partial\delta} - \frac{eV(\tau)}{T_0\beta cE}\frac{\partial\Psi}{\partial\delta} = 0. \tag{2.53}$$

We deviate here from the previous section in the choice of the new variables which will simplify the Vlasov equation since the action-angle variables corresponding to the new Hamiltonian are no longer the old τ and ϕ defined earlier.

Starting with the Hamiltonian

$$H_0 = \frac{\delta^2}{2} + \frac{\beta^3 c}{\eta}\frac{\omega_{s0}^2\beta\tau^4}{\eta c}\frac{(n^2-1)}{4!}(h\omega_0)^2 \tag{2.54}$$

δ and τ are not canonical variables, thus we choose

$$\bar{\tau} = -\frac{\beta^3 c}{\eta}\tau \tag{2.55}$$

then

$$\begin{aligned} H_0 &= \frac{\delta^2}{2} + \left(\frac{\eta}{\beta^3 c}\right)^3\frac{\omega_{s0}^2\beta}{\eta c}\frac{(n^2-1)}{4!}(h\omega_0)^2\bar{\tau}^4 \\ &= \frac{\delta^2}{2} + a\bar{\tau}^4 \end{aligned} \tag{2.56}$$

where

$$a = \frac{\omega_{s0}^2\eta^2(n^2-1)h^2\omega_0^2}{4!\beta^8 c^4}.$$

Note that $\bar{\tau}$ is related to the rf phase angle r by

$$|r| = \left| \frac{h\omega_0\eta}{\beta^3 c}\bar{\tau} \right| \tag{2.57}$$

For a fixed H_0, there exists a maximum $\bar{\tau}$, $\bar{\tau}_{\max}$, which in turn gives

$$\delta = \sqrt{2a(\bar{\tau}_{\max}^4 - \bar{\tau}^4)}. \tag{2.58}$$

The action variable I is defined to be

$$\begin{aligned} I &= \frac{1}{2\pi}\oint \delta d\bar{\tau} \\ &= \frac{4\sqrt{2a}}{2\pi}\bar{\tau}_{\max}^3 \int_0^1 \sqrt{1-x^4}dx \\ &= \frac{4\sqrt{a}}{3\pi}K\left(\frac{1}{2}\right)\bar{\tau}_{\max}^3 \end{aligned} \tag{2.59}$$

where $K(\frac{1}{2})$ denotes the complete elliptic integral of the first kind and will be denoted by K in the following. Equation (2.59) can be written equivalently:

$$\bar{\tau}_{\max} = \left(\frac{3\pi I}{4\sqrt{a}K}\right)^{1/3} \tag{2.60}$$

If we introduce a generating functional $W(I,\bar{\tau})$ such that

$$\frac{\partial W(I,\bar{\tau})}{\partial \bar{\tau}} = \sqrt{2a}\sqrt{\bar{\tau}_{\max}^4 - \bar{\tau}^4}$$

or

$$W(I,\bar{\tau}) = \sqrt{2a}\int_{\bar{\tau}_{\max}}^{\bar{\tau}} \sqrt{\bar{\tau}_{\max}^4 - \bar{\tau}'^4}d\bar{\tau}' \tag{2.61}$$

the angle variable ϕ is obtained through

$$\phi = \frac{\partial W(I,\bar{\tau})}{\partial \bar{\tau}_{\max}}\frac{d\bar{\tau}_{\max}}{dI} \tag{2.62}$$

From Eqs. (2.60) and (2.61) after some manipulations, this gives

$$-\frac{2K(\frac{1}{2})}{\pi}\phi = \int_0^{\cos^{-1}x} \frac{dt}{\sqrt{1-\frac{1}{2}\sin^2 t}}, \qquad x = \bar{\tau}/\bar{\tau}_{\max}$$

or

$$\mathrm{cn}\left[\frac{2K(\frac{1}{2})}{\pi}\Phi\right] = -\bar{\tau}/\bar{\tau}_{\max} \tag{2.63}$$

where cn(u) is the cosine of the Jacobian elliptic function.[11] Thus from Eqs. (2.58) and (2.63) we get the transformation between $(\bar{\tau}, \delta)$ and (I, ϕ):

$$\bar{\tau} = -\left(\frac{3\pi I}{4\sqrt{a}K}\right)^{1/3} \mathrm{cn}\left(\frac{2K\phi}{\pi}\right)$$

$$\delta = \sqrt{2a}\left(\frac{3\pi I}{4\sqrt{a}K}\right)^{2/3}\left[1 - \mathrm{cn}^4\left(\frac{2K\phi}{\pi}\right)\right]^{1/2}. \tag{2.64}$$

It can be explicitly shown that the Jacobian of the transformation Eq. (2.64) is unity. However, for practical calculation, we want to use some approximation to Eq. (2.64) since the series expansion of Eq. (2.64) converges quite fast. Note that

$$\mathrm{cn}\left[\frac{2}{\pi}K\left(\frac{1}{2}\right)\phi\right] = .95501\cos\phi + .00430\cos 3\phi + ...$$

We thus write

$$\bar{\tau} \approx \left(\frac{3\pi I}{4\sqrt{a}K}\right)^{1/3}\cos\phi$$

$$\delta \approx \sqrt{2a}\left(\frac{3\pi I}{4\sqrt{a}K}\right)^{2/3}[1 - \cos\phi^4]^{1/2}. \tag{2.65}$$

Now we are ready to add the perturbation due to the longitudinal coupled bunch instability to H_0. We can follow exactly the derivation in the previous section except that the variables we use are different now.

Again we have

$$H = H_0 + H_1$$

$$= a\left(\frac{3\pi I}{4\sqrt{a}K}\right)^{4/3} + \frac{\beta^3 c}{\eta}\int^{\tau} g_1(\tau')d\tau' \tag{2.66}$$

where

$$g_1(\tau) = -\frac{eV(\tau)}{T_0\beta cE}$$

just as in the previous section.

In the new variables Vlasov equation reads

$$\frac{\partial\Psi_1}{\partial s} + \frac{d\phi}{ds}\frac{\partial\Psi_1}{d\phi} + \frac{d\Psi_0}{dI}\frac{dI}{ds} = 0. \tag{2.67}$$

Keeping everything to the correct order of the perturbation, i.e.,

$$\frac{dI}{ds} = -\frac{\partial H_1}{\partial\phi} = -\frac{\partial H_1}{\partial\bar{\tau}}\frac{\partial\bar{\tau}}{\partial\phi} = \frac{eV(\tau)}{T_0\beta cE}\left(\frac{3\pi I}{4\sqrt{a}K}\right)^{1/3}\sin\phi$$

$$\frac{d\phi}{ds} = \frac{\partial H_0}{\partial I} = a\left(\frac{3\pi}{4\sqrt{a}K}\right)^{4/3}\frac{4}{3}I^{1/3}.$$

Thus the Vlasov equation is

$$\frac{\partial \Psi_1}{\partial s} + \frac{4}{3} a I^{1/3} \left(\frac{3\pi}{4\sqrt{a}K} \right)^{4/3} \frac{\partial \Psi_1}{\partial \phi} + \left(\frac{3\pi I}{4\sqrt{a}K} \right)^{1/3} \frac{eV(\tau)}{T_0 \beta c E} \sin\phi \frac{d\Psi_0}{dI} = 0 \tag{2.68}$$

We will make a final change of variables on Eq. (2.68)

$$I = \frac{4\sqrt{a}K}{3\pi(h\omega_0 b)^3} r^3 \tag{2.69}$$

where

$$r = bh\omega_0 \bar{\tau}_{\max} = h\omega_0 \tau_{\max}$$

$$b = \eta/\beta^3 c$$

r is the bunch length in rf radian.

Now the new Vlasov equation reads

$$\frac{\partial \Psi_1}{\partial s} + \frac{\omega_s(r)}{\beta c} \frac{\partial \Psi_1}{\partial \phi} - \frac{\Psi_0'}{r} \frac{\pi(h\omega_0 b)^2 eV}{T_0 \beta c E 4\sqrt{a}K} \sin\phi = 0 \tag{2.70}$$

where the synchrotron frequency is now defined as

$$\omega_s(r) \equiv \beta c \frac{d\phi}{ds} = \frac{\pi\sqrt{a}}{K} \beta c \frac{r}{h\omega_0 b}$$

and is explicitly amplitude dependent. At this point we need to calculate

$$\Psi_0' = \frac{d\Psi_0}{dr} = \frac{4\sqrt{a}K}{\pi(h\omega_0 b)^3 r^2} \frac{d\Psi_0}{dI}$$

or equivalently, find out how $\Psi_0(r)$ is normalized. As before, we have

$$N = \int \Psi_0 d\delta d\tau = \int \Psi_0 b d\delta d\bar{\tau} = \int \Psi_0 b dI d\phi \tag{2.71}$$

The distribution takes on the form

$$\Psi_0 = Ae^{-H_0/\sigma_\delta^2}$$

$$= Ae^{-\frac{a}{\sigma_\delta^2}\left(\frac{3\pi I}{4\sqrt{a}K}\right)^{4/3}}$$

$$= Ae^{-(r/r_0)^4} \tag{2.72}$$

where

$$r_0 = h\omega_0 b \left(\frac{\sigma_\delta^2}{a} \right)^{1/4}$$

σ_δ is the spread in δ - space. Then Eq. (2.71) determines A and

$$\Psi_0(r) = \frac{N(h\omega_0 b)^3}{2\sqrt{a}kbr_0^3\Gamma\left(\frac{3}{4}\right)} e^{-(r/r_0)^4} \tag{2.73}$$

Of course we still need to determine σ_δ in order to get r_0 as defined in Eq. (2.72). This can be done as follows. First observe that the RMS bunch length σ_ϕ in ring radian is given by

$$\sigma_\phi^2 = \frac{1}{h^2}\frac{\int_{-\infty}^{\infty} dr e^{-(r/r_0)^4} r^2}{\int_{-\infty}^{\infty} dr e^{-(r/r_0)^4}} = \frac{1}{h^2}\frac{\Gamma(3/4)}{\Gamma(1/4)} r_0^2. \tag{2.74}$$

Using Eq. (2.72), we get

$$\sigma_\phi = \sqrt{\frac{\Gamma(3/4)}{\Gamma(1/4)}}\left[\frac{4}{B}\left(\frac{\eta\omega_0\sigma_\delta}{\beta^2}\right)^2\right]^{1/4} \tag{2.75}$$

where

$$B = \frac{\omega_{s0}^2 h^2}{3!}(n^2 - 1).$$

On the other hand we know that the bunch area S can be given by

$$S = 6\pi\sigma_E\sigma_\phi(R/\beta c) \tag{2.76}$$

with R being the circumference. With Eqs. (2.75), (2.76) and the fact that $\sigma_\delta = \sigma_E/E$, we get

$$\sigma_\delta = \left(\frac{\beta^2 cS}{6\pi RE}\right)^{2/3}\left[\frac{\Gamma(1/4)}{\Gamma(3/4)}\right]^{1/3}\left(\frac{4}{B}\right)^{-1/6}\left(\frac{1}{\eta\omega_0}\right)^{1/3} \tag{2.77}$$

This should be inserted back into Eqs. (2.72) and (2.73). The Vlasov equation (2.70) now will be treated exactly the same as Eq. (2.9), notice however the different r-dependence in the last term.

Exactly the same transforms as Eqs. (2.10) and (2.11) will be employed. We will not repeat the elaborate derivation leading to the counterpart of Eq. (2.27) for the present case but only give the result in the following. The only material differences between the two results lie in the difference of the r - dependence of the equations and the form of $\Psi_0(r)$.

$$\tilde{R}_l(\omega) = \Phi_l(\omega) - iA\sum_{l'=\pm 1} l' i^{l-l'}\int_0^\infty \frac{\Psi_0' r^2 dr}{\omega\beta - l\omega_s(r)}\tilde{R}_{l'}(\omega) \tag{2.78}$$

where

$$A = \frac{e^2 M}{4Eh^2 T_0\omega_0}\sum_p \omega_p Z(\omega_p)$$

$$\Phi_l(\omega) = \int_0^\infty \frac{iR_{l0}(r)}{\omega - \frac{l\omega_s(r)}{\beta}} r^3 dr$$

$$\tilde{R}_l(\omega) = \int_0^\infty \tilde{R}_l(r,\omega) r^3 dr$$

$$\sum_p = \sum_{p=Mj+s, j=-\infty}^{\infty} \qquad s = \text{coupled bunch mode}$$

$\Psi_0(r)$ is given by Eqs. (2.72), (2.73) and (2.77). We again considered only the two dipole modes $l = \pm 1$ and used the short bunch approximations for the Bessel functions.

One fundamental deviation from the previous calculation arises when we realize that the two modes $l = \pm 1$ are really degenerate in the unperturbed state due to the quartic potential and we can no longer isolate one from the other but have to treat the space spanned by these two modes the way we do perturbation theory on degenerate systems[7]. In short, the practice in the previous section of dropping one mode from the final result is not allowed. Thus we proceed from the secular equation (2.78), following the line of derivation from Eq. (2.27) to Eq. (2.36), and arrive at the dispersion relation for the Landau cavity with both $l = +1$ and $l = -1$ included:

$$H(z) = \begin{cases} 1 - F\int_{-\infty}^{\infty} \dfrac{x^5 e^{-x^4}}{z-x} dx & \mathrm{Im}(z) > 0 \\ 1 - F\left[\mathcal{P}\int_{-\infty}^{\infty} \dfrac{x^5 e^{-x^4}}{z-x} dx - (\pi i z^5 e^{-z^4})\right] & \mathrm{Im}(z) = 0 \\ 1 - F\left[\int_{-\infty}^{\infty} \dfrac{x^5 e^{-x^4}}{z-x} dx - (2\pi i z^5 e^{-z^4})\right] & \mathrm{Im}(z) < 0 \end{cases}$$

with

$$F = i\sum_p \omega_p Z(\omega_p) \frac{I_b \sqrt{6} M}{\pi \Gamma(3/4)(E/e)\sigma_\delta} \frac{1}{h(n^2-1)^{1/2}\omega_{s0}} \tag{2.79}$$

$\mathcal{P}$ denotes the principle value of the integral and I_b is the electric current per bunch. z is related to ω through

$$z = \omega\beta/(\delta\omega_s)$$

$$\delta\omega_s = \frac{\pi c\beta}{K}(a\sigma_\delta^2)^{1/4} \tag{2.80}$$

In contrast had we included only the $l = +1$ mode, the dispersion relation would have been

$$H(z) = 1 - F\int_0^{\infty} \frac{x^5 e^{-x^4}}{z-x} dx \tag{2.81}$$

There is clearly a need for analytic continuation across the positive real axis in the complex z-plane in a similar fashion as Eq. (2.45), where the practice of dropping the $l = -1$ mode was acceptable, but not in the current case.

3 Numerical Techniques and Results

3.1 Numerical techniques

Our starting point is equation (2.44) in the harmonic cavity case and Eq. (2.79) in the Landau cavity case. Both of which are of the form

$$I(\omega) = A(E)Z_{\text{eff}}(E) \tag{3.1}$$

Where $I(\omega)$ is a complicated function of the complex frequency shift ω involving all the complex integrals and analytic continuations, but independent of the energy, or cycle time. It is a characteristic of the particular resonance in question. $A(E)$ is a proportional constant which varies with time, and $Z_{\text{eff}}(E)$ is a quantity which characterizes the instability-inducing impedance for a given mode.

$$Z_{\text{eff}}(E) \sim \sum_{p=Mj+s, j=-\infty}^{\infty} \omega_p Z(\omega_p)$$

$$\omega_p = p\omega_0 + \omega\beta \tag{3.2}$$

For our purpose, we will again use short bunch approximation and replace Eq. (3.2) with

$$Z_{\text{eff}} \sim \sum_p e^{-(\nu_p \sigma_l/R)^2} \omega_p Z(\omega_p) \tag{3.3}$$

in order to take advantage of existing formulae (Ref. 12). In the above $\nu_p = \omega_p/\omega_0$, (σ_l/R) is the bunch length in ring radian. We also drop the insignificant dependence of $Z(\omega_p)$ on the perturbed part of the frequency.

From the discussions at the end of section 2.1, our purpose is to find the solution $\omega_m(t)$ of equation (3.1) with the biggest imaginary part for all values of time t, or equivalently, energy E. Then we integrate this imaginary part of $\omega_m(t)$ over time.

$$\text{Growth rate} \sim Im(\omega_m(t))$$

$$\text{Total Rate} \sim \int_{t_1}^{t_2} dt Im(\omega_m(t)) = \int_{E_1}^{E_2} dE \left(\frac{dt}{dE}\right) Im(\omega_m(E)) \tag{3.4}$$

The form of Eq. (3.1) suggests the following approach. We first find the mapping

$$\omega \longrightarrow I(\omega)$$

between the complex ω-plane and the complex I-plane. This is suggested graphically in Figure 2-2(a). Next we follow the value of $A(E)Z_{\text{eff}}(E)$ in the same complex plane of I as E changes from E_1 to E_2. This is shown in Figure 2-2(b). It should be remarked that here we approximated ω with ω_s in the expression of Z_{eff}. The intersection between the curve in Figure 2-2(b) with the family of curves in Figure 2-2(a) determines the solution ω_m at every energy value E. In other words Eq. (3.1) can really be viewed as a mapping of

$$E \longrightarrow \omega_m$$

Note this is multiple valued with cuts in the mapping from ω to $I(\omega)$. We should single out the solution of ω which has the largest imaginary part and resembles a true resonance. The numerical techniques used in computing $I(\omega)$ will be described below. As for the quantity $Z_{\text{eff}}(E)$, the approximation formula of a given mode number given in Ref. 12 is used. It will not be duplicated here for economy of space. In order to simulate Booster in reality, the time dependence of the accelerating voltage V and accelerating phase ϕ_s are generated by empirical routines which give values very close to the actual Booster parameters. Figure 2-3 shows the value of V and ϕ_s as generated by the empirical formula at different energy vs. the actual values.

3.1.1 Evaluating I(ω)

From the nature of the equation (3.1), some kind of iterative root-seeking algorithm must be employed. This implies that it is very important to find fast algorithms to compute the integrals in $I(\omega)$ so that not too much time is lost in the repeated evaluation. On the other hand we want to insist on an accuracy of the solution to better than 10^{-4} in absolute value. The task is further complicated by singularities in the integrals. It turns out that we have to divide up the complex plane into patches of asymptotic regions and intermediate regions. We then use different computation methods in them to ensure accurate local behavior and fast result. The reliability and smoothness of the calculation are checked along the boundaries of these patches. A master program then combines all these patches and adds in the necessary analytic continuation. The description of the master programs can be found in Appendix A.

3.1.2 Solving for ω

The complex frequency shift ω is solved for any given E according to Eq. (3.1) once we have the necessary routines to calculate $I(\omega)$ and $A(E)Z_{\text{eff}}(E)$. An IMSL iterative routine ZANLYT is employed to solve for the roots of up to 10^{-6} accuracy. A "safety valve" is built into the program to automatically terminate the iteration and give a warning signal when exceedingly large numbers are encountered. The calculation then resumes at the next energy value. This is to prevent the program from crashing during execution when the iterations get out of control. We observe such occurrences only when the solution does not exist because of the "gap" problem discussed in the next section, or when the values given are unrealistically large as will be seen towards the end of section 4. Both problems have their origin in the limited computer capability to handle large numbers. In realistic cases we rarely encounter any numerical disaster and this practice is quite successful in affording highly accurate results.

The time it takes such a program to carry out 1500 iterative solutions for the harmonic cavity is roughly 38 CPU seconds on a VAX 8650 mainly due to the possibility of using only polynomial expansions in the routines. In comparison the same number of calculations for the Landau cavity take about 23 CPU minutes.

3.2 Physical properties from the numerical calculation

Before going on to the result of the integrated growth, we take a look at the physical pictures implied by the problem. These are much more easily elucidated once we have the computer routines at hand. Figure 2-4 shows the complex plane of $I(\omega)$ as defined in Eq. (3.1) for the harmonic cavity, the lines are contours of constant $Im(\omega)$, which is indicated by the number associated with each line. The thick line corresponds to $Im(\omega) = 0$, those below it to $Im(\omega) < 0$, and those above it to $Im(\omega) > 0$. This is actually a simplified picture since there is really a cut (see Section 2-1 and Appendix A) along the negative imaginary axis in the complex ω plane when we map ω into $I(\omega)$. This cut produces a gap which winds around the origin indefinitely. The only manifestation of it are the discontinuities in the contours seen in the first and fourth quadrants in Figure 2-4. The actual structure of the Riemann sheets is too complicated to reproduce in a single graph. This "gap", however, did not give us real problems in the computation since the solutions are in general far from it. In the cases where we run into this "gap", we are far from resonance so it is not physically interesting, nor is the contribution big since the gap is quite narrow. It should be stressed again here as in Appendix A that if the computer accepted larger numbers, this problem would not have existed.

Figure 2-5 shows the same diagram for Landau cavity. Again the thick line corresponds to $Im(\omega) = 0$, the ones inside to $Im(\omega) < 0$, and the ones outside to $Im(\omega) > 0$. Again this is only an oversimplified picture. We see however that there is no "gap" as in the previous case due to the fact that we can analytically continue the mapping to the whole ω plane. Figures 2-4 and 2-5 would be more informative if viewed next to Figure 2-6, showing the development in time (or energy) of $A(E)Z_{\text{eff}}(E)$ for a typical harmonic cavity and two given resonances. The case for Landau cavity is similar. As the energy increases, the beam goes through several resonances with the cavity modes, marked by different "circles" in Figure 2-6. The one above the real axis clearly develops a growth in the beginning. The growth rate itself grows with time, only to recede later. The other "circle" on the other hand derives nothing but damping from the resonance. If we only look at the intersection of the upper circle with Figure 2-4 and plot the time (energy) development of its imaginary part, we get Figure 2-7, in which the resonance pattern is clear. Note near the end the upper circle goes into the "gap" and the solution there becomes meaningless, as can be seen from the glitches in Figure 2-7. This is however not in the region of interest. We can also look at the real part of the intersection minus the unperturbed synchrotron frequency. This is shown in Figure 2-8, which displays the typical behavior of frequency shifts near a resonance.

Finally we check our calculations with another example. In equation (2.37) we implied a synchrotron tune spread in the harmonic cavity due to the anharmonic part of the accelerating voltage. This tune spread after all should cause a small but visible Landau damping. We on the other hand take a purely harmonic cavity and look at its dispersion relation. This amounts to some manipulation of Eq. (2.35), keeping in mind now that ω_s does not depend on r:

$$\omega\beta = \pm\sqrt{\omega_{s0}^2 + Q}$$

where

$$Q = i\frac{e^2 N \eta \omega_0^3 M}{4\pi^2 E \beta^2} Z_{\text{eff}} \tag{3.5}$$

This is a much simpler relation. If we take the growing solution and compare with the calculation done using Eq. (2.35), we get Figure 2-9. There is a small but finite damping when the tune spread due to anharmonic potential is introduced into the harmonic cavity.

3.3 Results for harmonic and Landau cavities

Figures 3-1(a)-(i) show the results of growth rate calculations in various cases. For the convenience of getting total growth later, we changed the unit of growth rate from (1/sec) to (1/MeV) by a scaling factor dE/dt. In the Booster dP/dt follows a sinusoidal pattern and is theoretically zero at the end of each cycle. This leads to undesired artifact in the above scaling practice. Looking at the real rf data of the Booster, we realized that beyond 8.8 GeV, the energy rises at an approximate average rate of 10^5 MeV/sec. Thus we choose to use the relation between dE/dt and E as depicted in Figure 3-2 for our calculation. This small discontinuity at 8.8 GeV is therefore responsible for all the non-smooth behaviors displayed in Figure 3-1 at 8.8 GeV.

In every individual graph of Figure 3-1 shown as growth rate in (1/MeV) vs. energy in MeV, the dotted curve represents the harmonic cavity. The header gives the coupled bunch mode and driving resonance number as listed in Table 1.

Table 4 lists the exponent of the total integrated growth defined in Eq. (2.48) according to Figure 3-1 for both cavities. In summing up the total growth only the positive imaginary part of ω is included.

4 Discussions

Section 3-3 contains the major results of this work. Figure 3-1(c) shows a very satisfactory effect of the Landau cavity, while Figure 3-1(h) shows the Landau cavity more as an aggravation than a relief. The rest fill all the intermediate scenarios. To better understand this, we notice that regardless of the special case in question, the behavior near the peak of the resonance has a decisive effect on the overall behavior. The correlation between the behavior at the peak and the behavior in general is quite visible from Figure 3-1 when we compare the harmonic cavity with the Landau cavity. The behavior near the peak is however much easier to grasp theoretically. Let us look at equations (2.44) to (2.46). If we assume right at the peak that the impedance is so large that the tune spread does not play any significant role, we can follow what we did at the end of Section 3-2 where the tune spread is truly absent. This amounts to taking out the x−dependence in the denominator of the integrand and we get the dispersion relation:

$$Im(\Delta\omega) = \frac{\eta M I_b \omega_0^2}{4\pi\beta^2 \omega_s (E/e)} Z_{\text{eff}} \tag{4.1}$$

where $\Delta\omega$ is the complex frequency shift and I_b the current per bunch. This equation is not exactly the same as Eq. (3.5) in that there we included both dipole modes a=−1 and a=+1 whereas here we keep only a=+1. The justification of this is mentioned in Section 2-1.

In the case of the Landau cavity, both modes have to be included. To be able to carry out the integral, we note that

$$\int_{-\infty}^{\infty} dx \frac{x^5 e^{-x^4}}{x - z} = \int_0^{\infty} dx \frac{x^6 e^{-x^4}}{x^2 - z^2} \tag{4.2}$$

and again neglecting the tune spread near the peak amounts to taking out the x-dependence in the denominator of the integrand. This gives the dispersion relation:

$$Im(\Delta\omega) = \sqrt{\frac{\eta M I_b \omega_0^2}{4\pi\beta^2 E/e} Z_{\text{eff}}} \tag{4.3}$$

where we used the approximation

$$\frac{1}{2} \frac{\pi^2 \Gamma(7/4)}{K(1/2)^2 \Gamma(3/4)} \approx 1.079 \approx 1. \tag{4.4}$$

Had we left out the $l = -1$ mode, the simplified growth of Eq. (4.3) would have become

$$Im(\Delta\omega) = \frac{\eta M I_b \omega_0^2}{4\pi\beta^2 E/e} \frac{1}{\delta\omega_s} Z_{\text{eff}} \tag{4.5}$$

with $\delta\omega_s$ given in Eq. (2.80). Note the drastic difference between Eq. (4.3) and the incorrect Eq. (4.5), especially when Z_{eff} is large.

Comparing Eq. (4.1) with Eq. (4.3), we can derive the following conclusions:

a. In the cases where Z_{eff} is very large and therefore the dominant factor, the use of Landau cavity would suppress the growth simply by power counting in Eqs. (4.1) and (4.3). However, when Z_{eff} is big enough for the difference between Eqs. (4.1) and (4.3) to be appreciable, Eq. (4.3) itself is usually too big for the Landau cavity to look attractive.

b. In the cases where Z_{eff} is small enough that the tune spread has a dominant effect even near the peak, our approximations Eqs. (4.1) and (4.3) break down and don't teach us anything about the growth rates. In this event the dominant tune spread would act to discourage any coherent pattern accumulated within the bunch and we also expect the Landau cavity to reduce the growth rate significantly.

c. In the intermediate region where none of the above applies, it requires a detailed knowledge of all the factors which have effects on $\Delta\omega$ to reach a conclusion. This could be difficult since insufficient knowledge of some factor may lead to the failure of a prediction. Some of our examples fall in this category.

The series of graphs in Figure 4-1 can best illustrate our point. Figure 4-1(a) shows the growth rate for harmonic cavity (dotted line) and Landau cavity (solid line) under the same prescribed conditions. Figures 4-1(b) through (g) shows the same graphs with the Z_{eff} scaled according to the numbers in the parentheses in the headers. When Z_{eff} is scaled by a factor either smaller than 0.2 or bigger than 5.0, Landau cavity produces less growth around the

peak, while in the intermediate region it produces more. The discontinuities in the last few graphs are results of the "safety valve" mentioned in Section 3-1-2. The general tendency however is not missed in these graphs. The unrealistic widths of the peaks in the last few graphs could be artifacts of approximations and is not understood at this point.

Among the three possibilities discussed above, (b) is where a Landau cavity will be useful. When dealing with broad band impedances or resonances with weak enough peaks, we can in general apply the Landau cavity to suppress the growth.

Generally speaking, the effectiveness of Landau damping is determined by the competition between the growth rate $\Delta\omega$ in our calculation and the extent of the synchrotron tune spread $\delta\omega_s$. The tune spread is inversely proportional to the time scale during which the particles can remain coherent. Any meaningful growth has to take place in a time scale much shorter than this one in order not to be wiped out simply by decoherence of the beam. This leads to the general criterion for Landau damping:

$$\Delta\omega \ll \delta\omega_s \tag{4.6}$$

This can rarely be satisfied at the peak in a general sense. Thus most of the time there will be some growth right at the peak even for a Landau cavity. It is also true however that this growth could have been bigger without the Landau cavity. Notice we still have the freedom to adjust the parameter n in Eq. (2.49) in favor of the inequality (4.6), although technical complication may arise from a large n.

Another point that concerns us is that as mentioned in Section 3-1, we picked the one solution with the largest imaginary frequency shift as our solution. This would be unambiguous if in the integral such as Eq. (2.34) the number of poles were finite and the integral could be represented as a finite sum of the residue contributions. Such is the case for a Lorentzian distribution, for example. However, in our current treatment a Gaussian distribution is used for the bunches and the above integral can only be represented as an infinite sum. In such a case the practice of singling out the solution with the largest imaginary part might lead to unreliable results in extreme cases. This is mentioned here pending further clarification.

To sum up, we achieved an understanding of the coupled bunch instabilities under either a harmonic potential or a quartic (Landau cavity) potential. The model we used is the Fermilab 8 GeV Booster. The result indicates that with the parameters we have, the Landau cavity lives up to its promise to various extents depending on how closely the general criterion Eq. (4.6) is followed.

A Programs for evaluating the functions I(ω)

A.1 The Harmonic Cavity

A program is written for the function $I(z)$ in Eq. (2.44). The complex z-plane is divided up as in Figure A-1. We used 8-point Gauss-Laguerre and 20-point Gauss-Laguerre approximations in the asymptotic regions together with the small argument expansion

$$\begin{aligned} I(z) &= 1 && (|z| = 0) \\ &= 1 - \frac{z}{2} e^{z/2} E_1(z/2) && (|z| \neq 0) \end{aligned}$$

$$E_1(z) = 1 - r - \ln z - \sum_{n=1}^{\infty} \frac{z^n}{nn!} \tag{A.1}$$

where $r = 0.57721566....$ is the Euler's constant. The shape of the patches is determined both to ensure satisfactory local behavior and to avoid singularities of the Gauss-Laguerre integrals on the real axis.

The expansion (A.1) already takes into account the analytic continuation onto the negative real axis. Further we will analytically continue across the negative real axis into the 3rd quadrant, and therefore push the cut down to the negative imaginary axis. We can not keep extending the analytic region in this manner since the term $exp(z)$ added in this process will sometimes exceed the computer tolerance of large numbers when an iterative process is involved. Thus we leave this cut in the negative imaginary axis since from experience it does not affect anything interesting physically. But the manifestation of this cut can be seen in some of our results, as mentioned in Section 3. The fact that we are able to use nothing but series expansions to approximate the integral proves to be advantageous in speed when the iterative root-seeking routine is applied on this program.

A.2 The Landau Cavity

A program is also written to evaluate the integrals in Eq. (2.79). Unfortunately no similar small-argument expansion formula is known to exist[13]. Thus we are forced to incorporate some numerical integration routines in the iterative algorithm, which makes the process run much slower, sometimes by a factor of 40 relative to the previous case. The complex plane of z is divided up as in Figure A-2. We again used different computation methods in different patches to ensure accuracy and efficiency. In Figure A-2, ZGAUS is the 20-point Gauss-Laguerre approximation. ZINTI is a straightforward numerical integration routine. In the routine ZPRIN we employed the principle value and residue prescription given in Eq. (2.79), which can give accurate result even off (but not far from) the real axis, if we adjust the relevant parameters carefully. Finally we also have the "back up" routine ZSM prepared for the region where the value of z is too close to the real axis for the numerical integration routine ZINTI to work reasonably well, but not close enough so that the principle

value prescription is valid numerically. Empirically this region is very small for our required accuracy of 10^{-4} and other parameters. But in order to avoid any possible adverse effects in the iterative root-seeking process and to prepare for a more general situation, we should address this problem anyway. Thus the routine ZSM is constructed which picks up the finite contributions of the functions which are even about the poles in an infinitesimal region around them, and then numerically integrate over the rest. This attempt turns out to be successful and eliminates the possibility of discontinuity in the iterative solution. We expect this practice to be more important in other cases where more accuracy is required.

The analytical continuation, however, is more straightforward in our case. Since the discontinuity in the mapping runs along the whole real axis, all we need for an analytic solution over the whole complex plane is to continue the solution across the whole real axis into the lower half plane, therefore eliminating the "gap" in the mapping which caused unpleasant effects in the previous case.

Acknowledgement

We would like to acknowledge useful discussions and comments from our colleagues, notably Chuck Ankenbrandt, Jim Crisp, Jim Griffin, and Steve Holmes.

References

1. There is a vast literature on this subject, for example, A. Hofmann, International School of Particle Accelerators, Erice, 1976, CERN 77-13, p. 139. and reference therein.

A. Chao, AIP Proceedings 105, 1983, p.353. and reference therein. This is not intended as a complete list.

2. J. Crisp, Private communications.

3. K. Y. Ng, Fermilab Report FN-436. A. Sorensen, Particle Accelerators, 6, p.141, 1975

4. M. Cornacchia, Fermilab Report TM-1442

5. J. Crisp, Private communications.

6. J.D. Jackson, Nuclear Energy Part C : Plasma Physics, 1, p.171, 1960

7. S. Krinsky and J.M. Wang, Particle Accelerators, 17, p.109, 1985. J.M. Wang, BNL 51302, 1980

8. J. Griffin, private communications.

9. J. Griffin, private communications.

J. Maclachlan, private communications.

10. A. Chao, reference 1.

11. I.S. Gradshteyn and I.M. Ryzhik, Table of Integrals, series, and Products. Academic Press.

12. See for example, M. Zisman et al., ZAP User's Manual, LBL-21270, Chap. IV, p.137 to 145.

13. C. Sogge, private communications.

W. Reid, private communications.

Figure captions

Figure 1-1. Bunch area vs. time in the Fermilab Booster.

Figure 1-2(a) Equilibrium bunch length with and without space charge force. η is the ratio between space charge force and linearized RF force. Transition happens at $x = 0$, with x the normalized time.

Figure 1-2(b) Bunch tumbling after transition due to space charge.

Figure 1-3(a) Mountain range pictures taken in the Fermilab Booster showing the pronounced "bunch tumbling" due to space charge effects.

Figure 1-3(b) Mountain range pictures taken in the Fermilab Booster showing the onset of the coupled bunch instability. The number next to each graph shows the cycle time in ms. Mode 16 starts growing around 22.3 ms.

Figure 1-4. Measured and calculated beam sizes at various times after injection. Four of the 18 cavities are off, but not shorted.

Figure 1-5. Measured and calculated beam sizes with 4 cavities shorted.

Figure 1-6. Bunch area with shorted and unshorted cavities.

Figure 1-7(a) Booster beam signal at one pickup as seen from a spectrum analyzer, showing all the modes. The first peak to the right of the rf harmonic lines is mode 16.

Figure 1-7(b) Time development of mode 16 for 20 ms, starting at 16 ms into the cycle.

Figure 1-8 Some of the "beating patterns" described at the end of Section 1-1 showing individual coupled bunch modes tracked by an input of integral multiples of the revolution frequency. The spectral analysis at the top of each graph shows the deviation of the beam signal from the input, and they all lie in the range of the dipole synchrotron oscillation frequency.

Figure 2-1. The integration contour W used in equation (2.11). The lower graph shows the closed contour used when $s < 0$.

Figure 2-2(a) Graph suggesting the map of ω into $I(\omega)$

Figure 2-2(b) Graph suggesting the time development of $A(E)Z_{\text{eff}}(E)$ in the plane of I.

Figure 2-3. Graphs showing the values of RF voltage and acceleration phase as generated by the empirical program vs. the actual value throughout the cycle.

Figure 2-4. Stability diagram of the harmonic cavity.

Figure 2-5. Stability diagram of the Landau cavity.

Figure 2-6. Time development of $A(E)Z_{\text{eff}}(E)$ for mode 45 and two resonances in the complex plane.

Figure 2-7. Growth rate (1/MeV) vs. energy (MeV) for mode 45, resonance 11.

Figure 2-8. Frequency shift magnified 1000 times (1/sec) vs. energy (MeV) for mode 45, resonance 11.

Figure 2-9. Graph showing the growth rate in a harmonic cavity with and without the anharmonic synchrotron tune spread.

Figure 3-1(a) through (h), All graphs are growth rates (1/MeV) vs. energy (MeV). The solid line corresponds to the Landau cavity and the dotted line the harmonic cavity. The headers show the mode number and serial number of the resonance as listed in Table 1.

Figure 3-2. The scaling of dE/dt actually used in the program.

Figure 4-1(a) through (g), (a) shows the growth rates (1/MeV) of the harmonic cavity (dotted line) and Landau cavity (solid line) vs. energy (MeV). The conditions are given in the header. The rest are the same except the effective impedances are scaled by the numbers given in the headers.

Figure A-1. The division of complex z-plane for the evaluation of $I(\omega)$ of harmonic cavity. The name inside each patch is the routine used. Analytic continuation is used for the lower half plane.

Figure A-2. The division of complex z-plane for the evaluation of $I(\omega)$ of Landau cavity. The name inside each patch is the routine used. Analytic continuation is used for the lower half plane and the same division is reflected about the imaginary axis. The division really extends to the real axis and covers the whole first quadrant but is not exactly shown here.

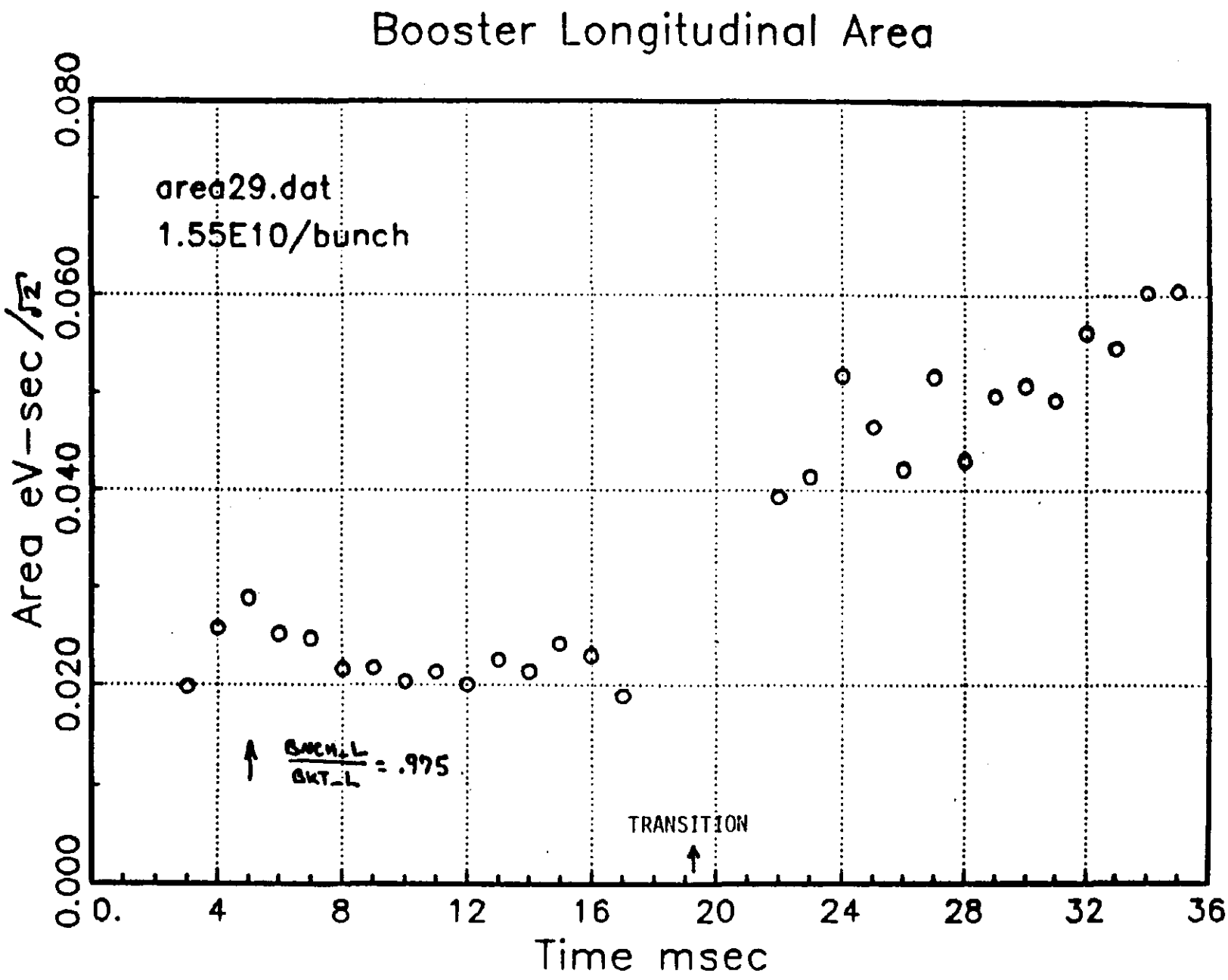

Figure 1-1 The bunch area of the Fermilab Booster increases after transition.

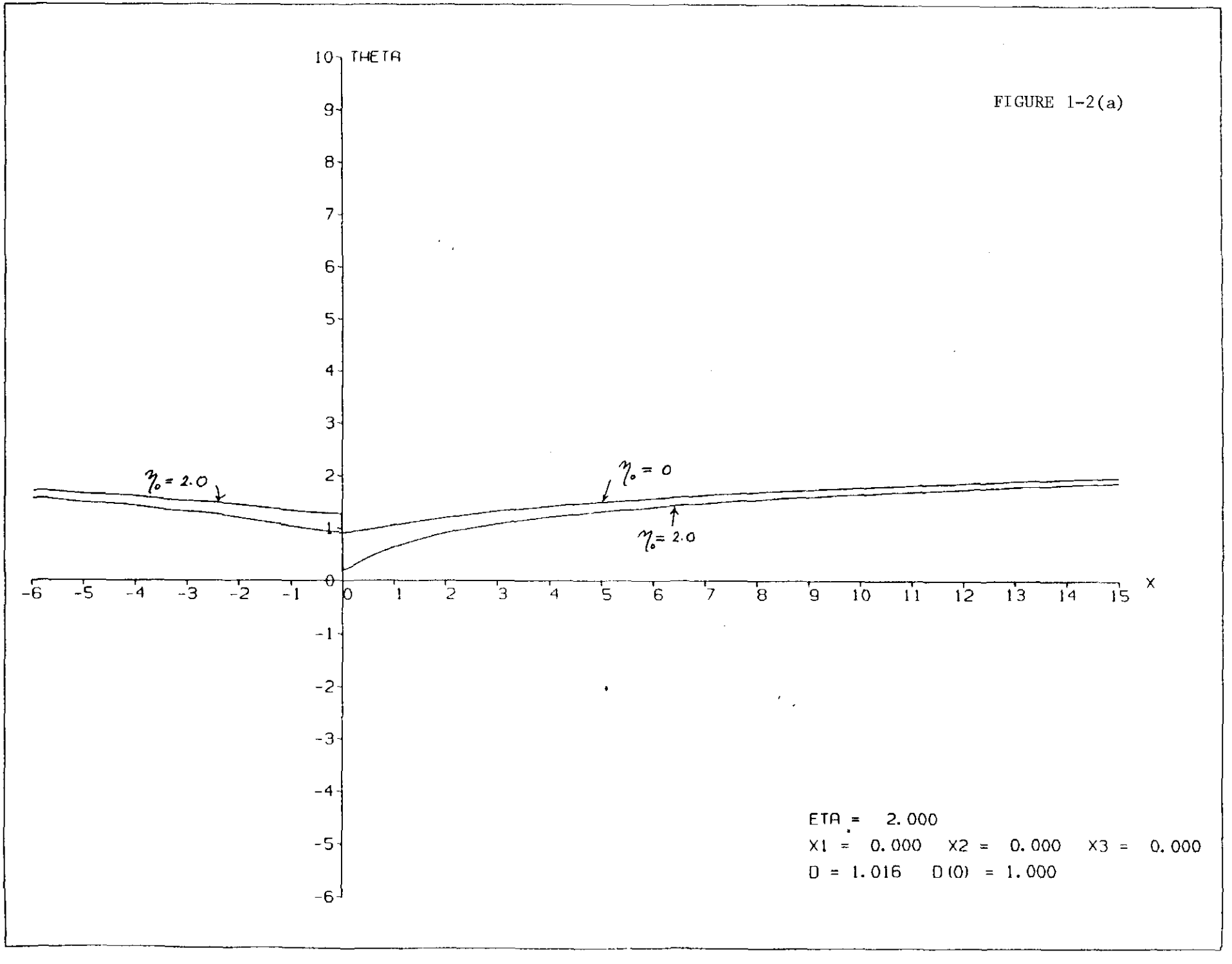
THETA
10
9
8
7
6
5
4
3
2
1
0
-1
-2
-3
-4
-5
-6
-6 -5 -4 -3 -2 -1 0 1 2 3 4 5 6 7 8 9 10 11 12 13 14 15
X
$\eta_o = 2.0$
$\eta_o = 0$
$\eta_o = 2.0$
ETA = 2.000
X1 = 0.000 X2 = 0.000 X3 = 0.000
D = 1.016 D(0) = 1.000

FIGURE 1-2(a)

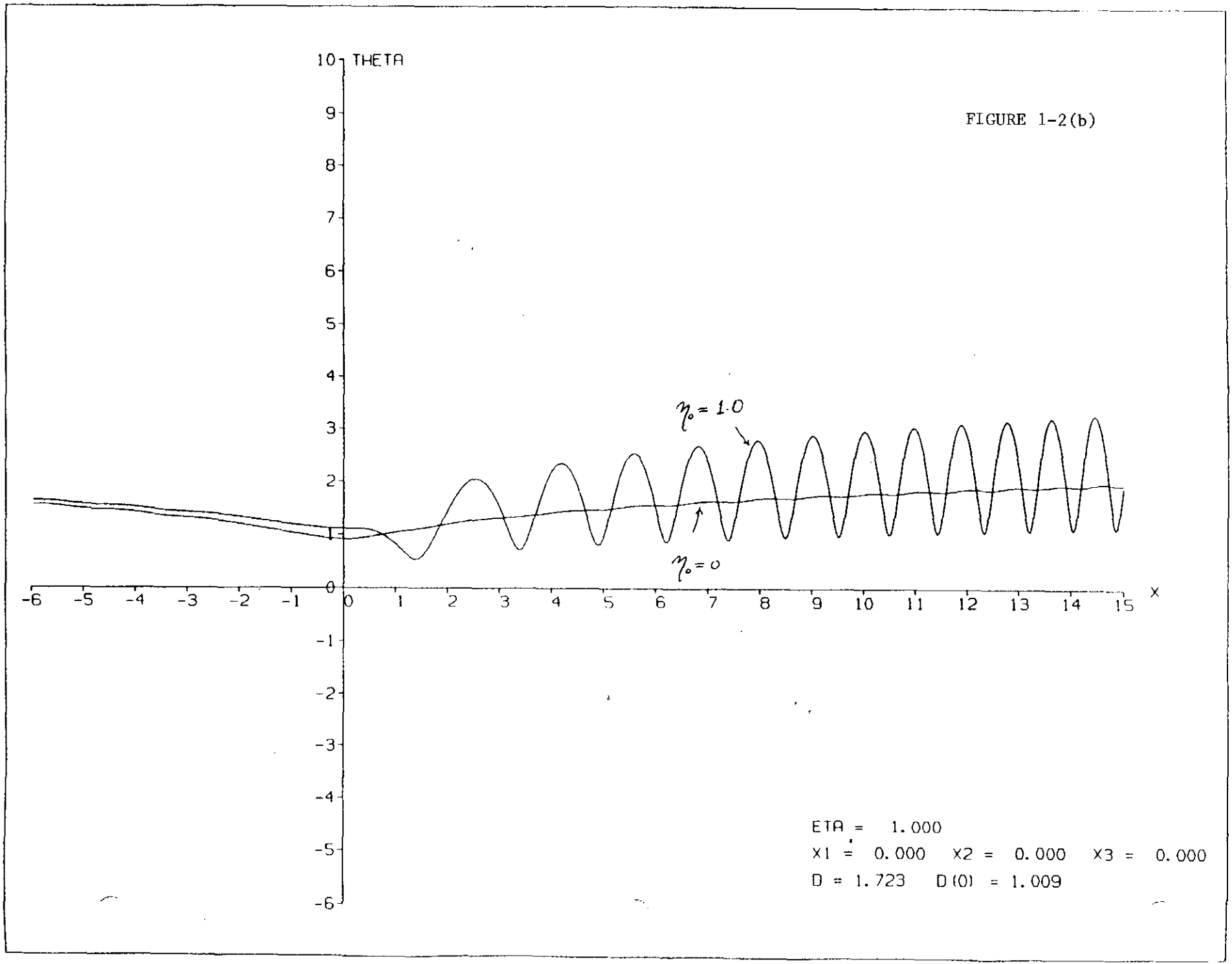
THETA
X
$\eta_o = 1.0$
$\eta_o = 0$
ETA = 1.000
X1 = 0.000 X2 = 0.000 X3 = 0.000
D = 1.723 D(0) = 1.009

FIGURE 1-2(b)

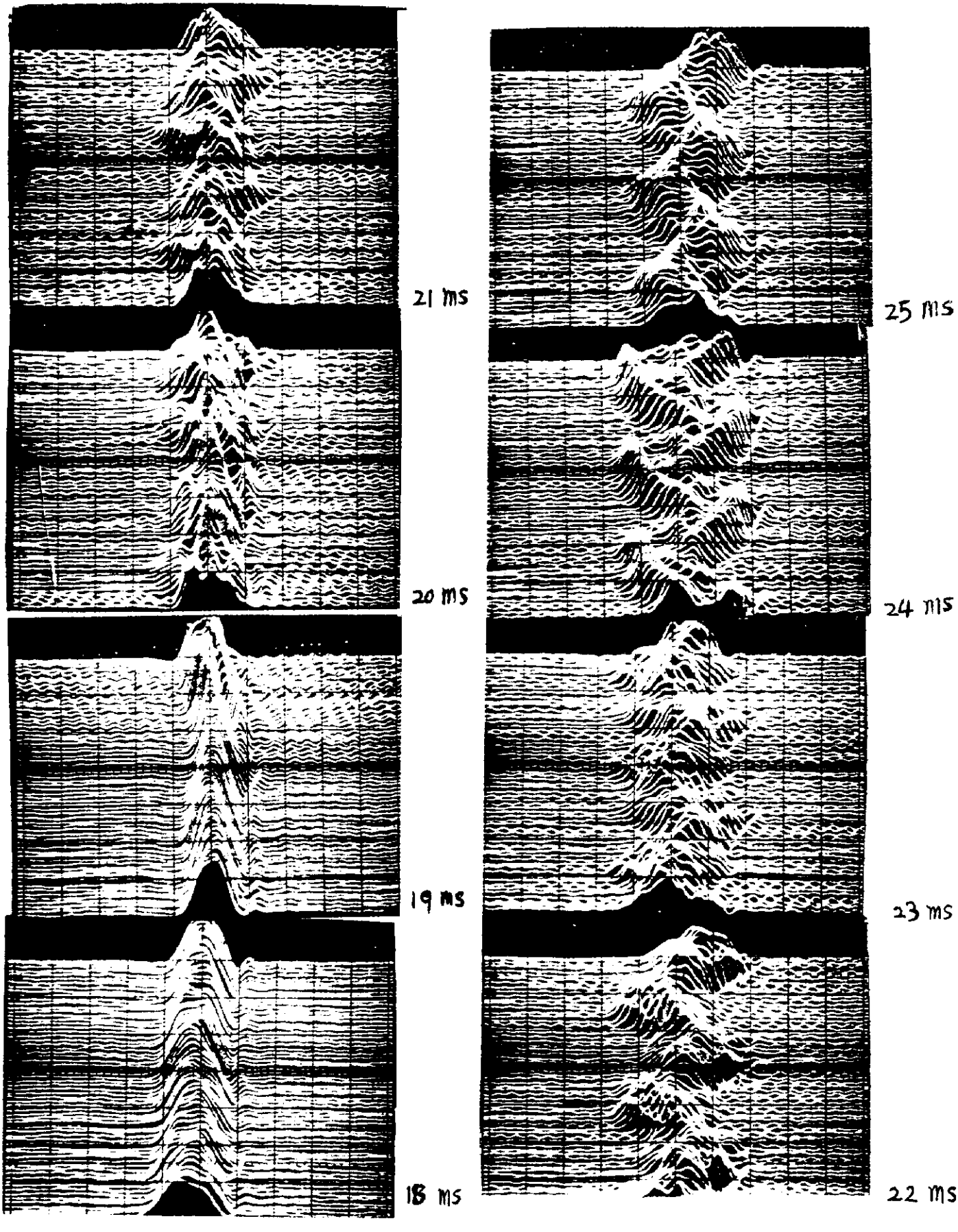

FIGURE 1-3(a)

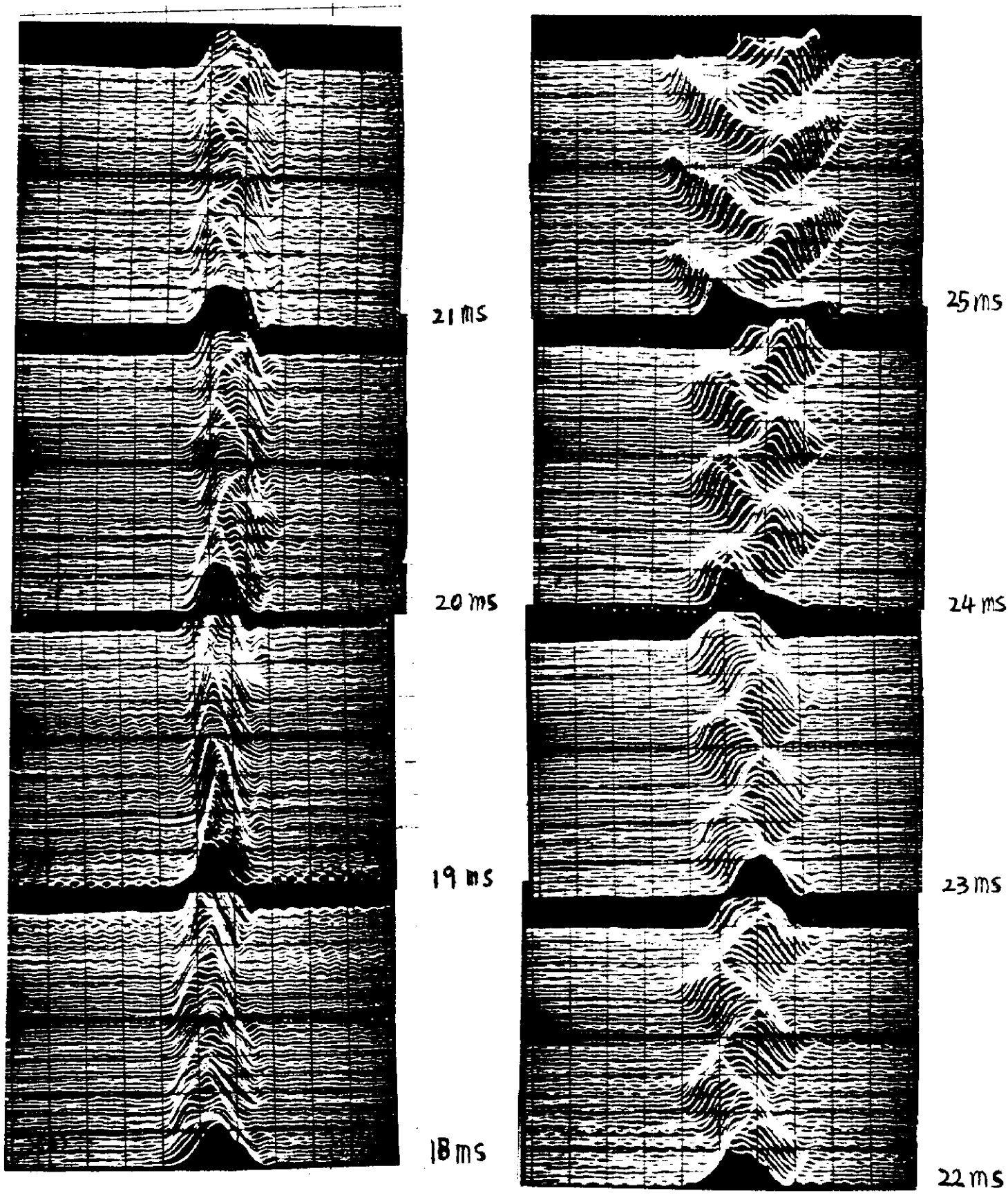

FIGURE 1-3(b)

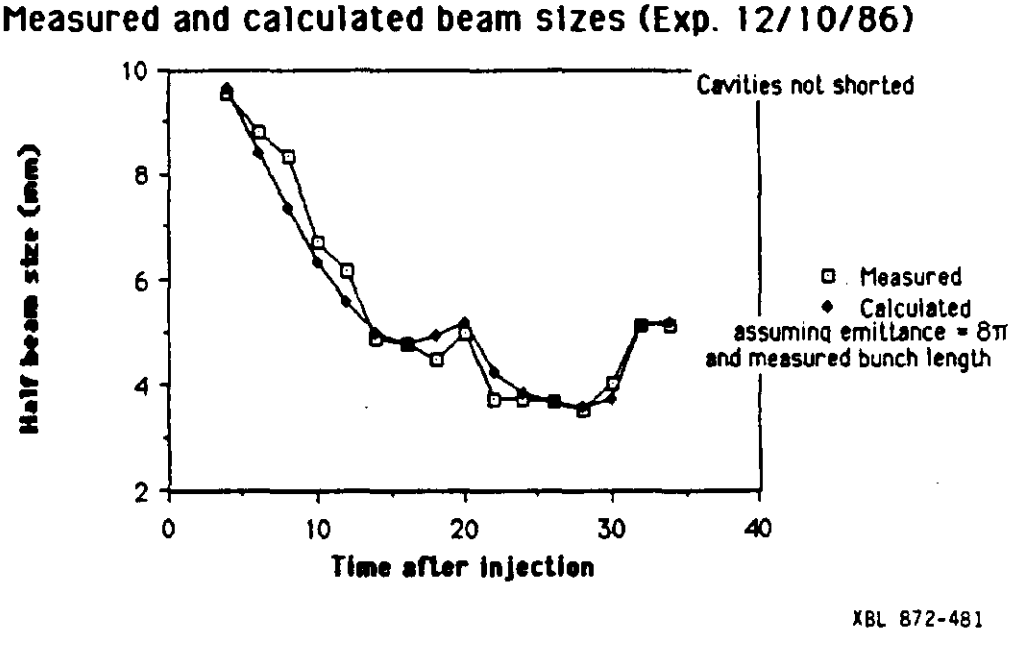

Fig. 1-4 Measured and calculated beam sizes at various times after injection. Four of the 18 cavities are off, but not shorted.

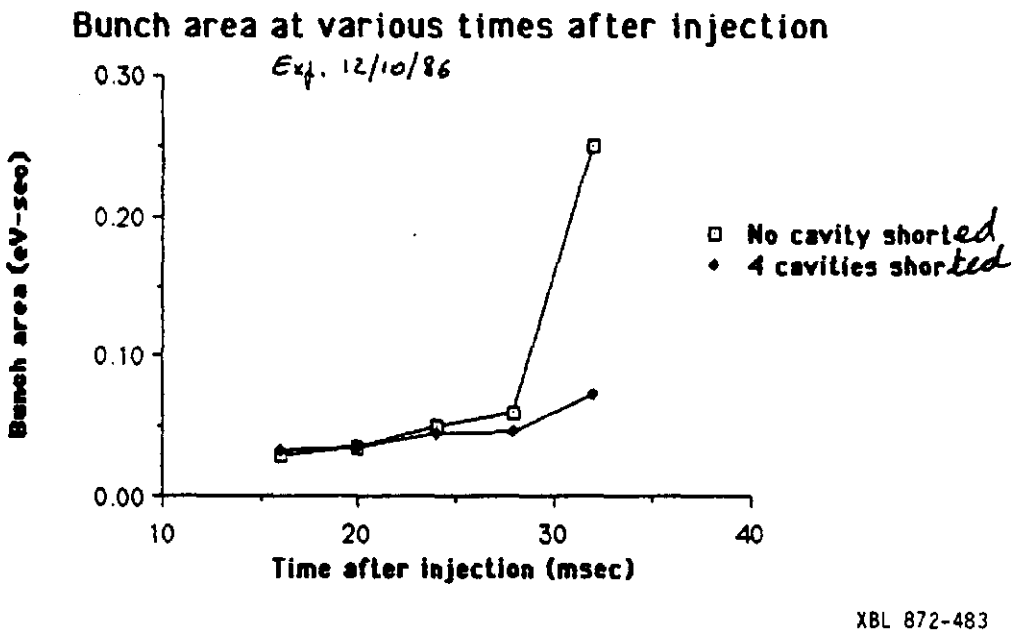

Fig. 1-6 Bunch area with shorted and unshorted cavities.

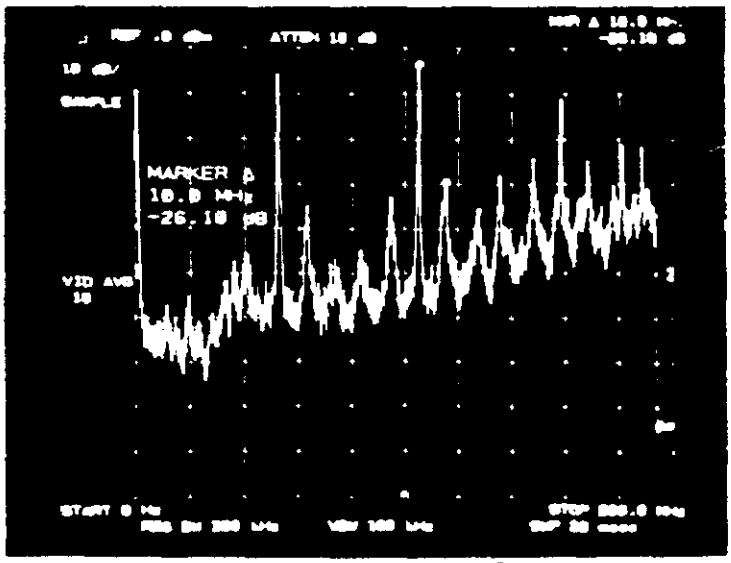

TTRX = 19500, h = 77 off, 1.65X10^12

FIGURE 1-7(a)

Mode 16

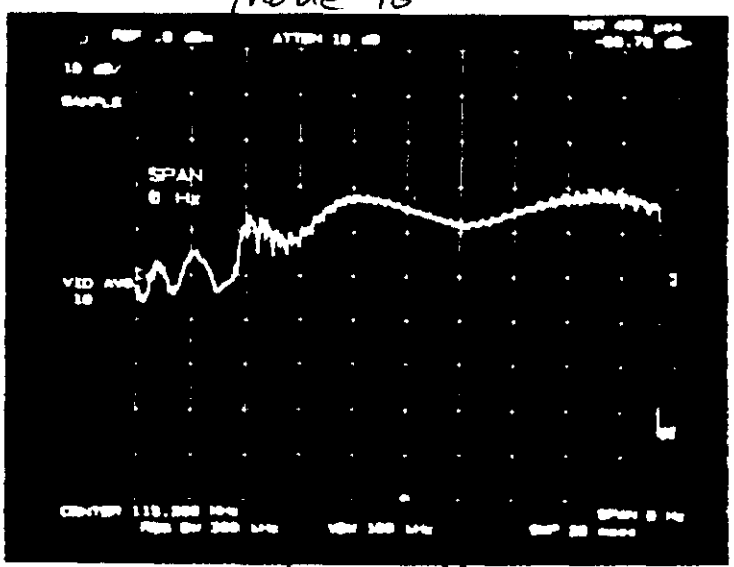

TTRX = 19500, h = 77 off, 1.65X10^12

FIGURE 1-7(b)

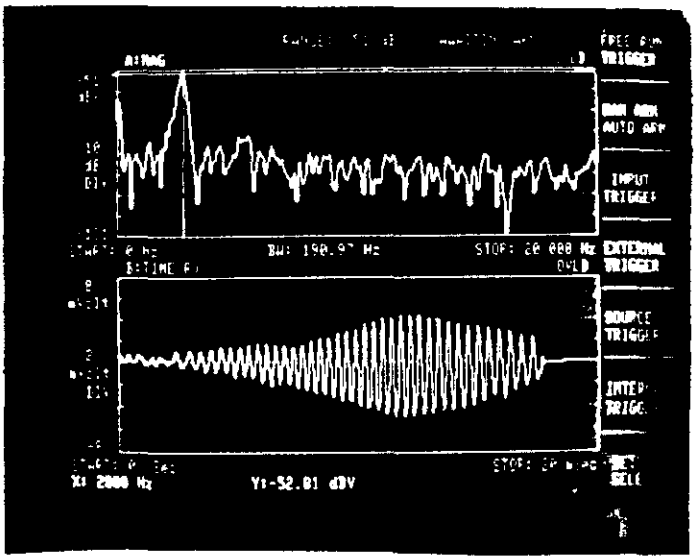

Mode 16

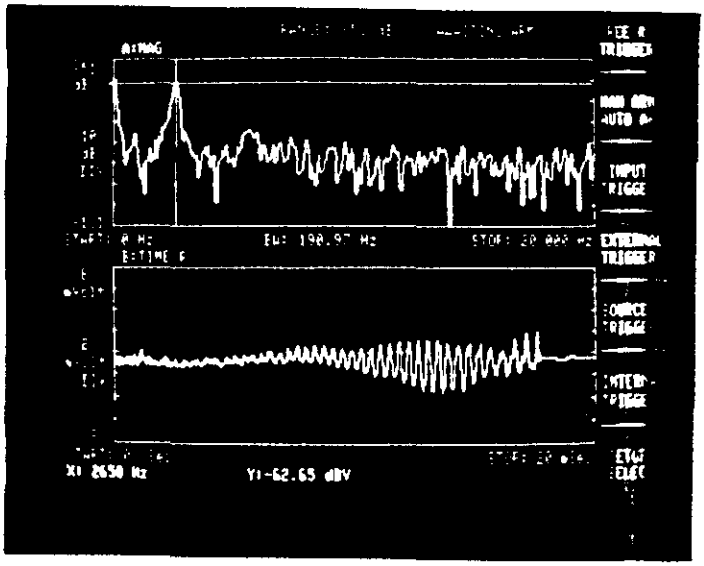

Mode 32

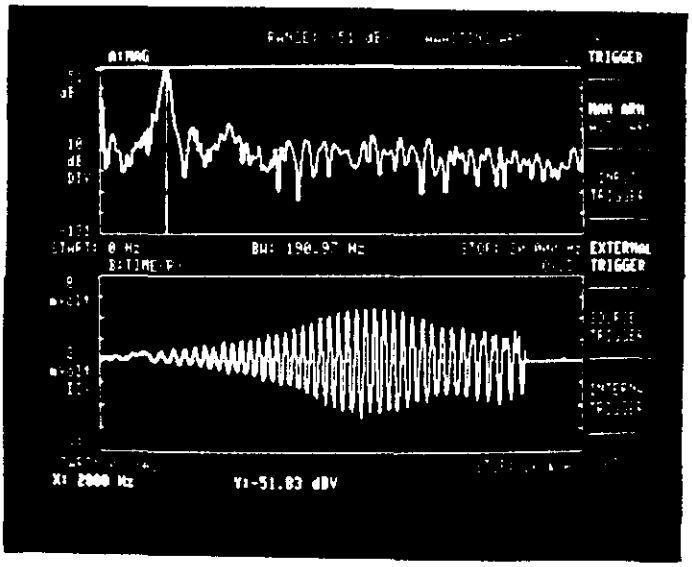

Mode 13

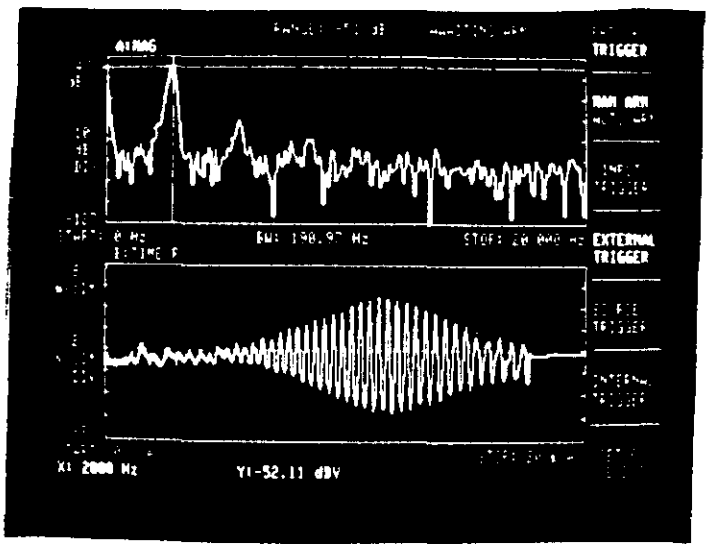

Mode 15

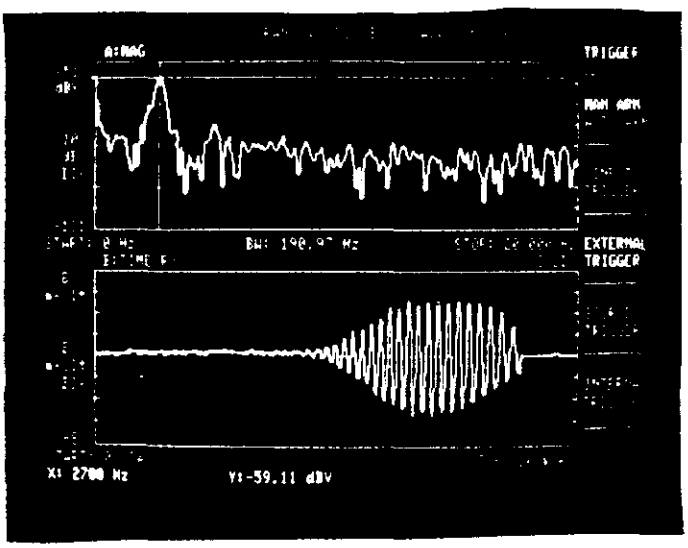

Mode 12

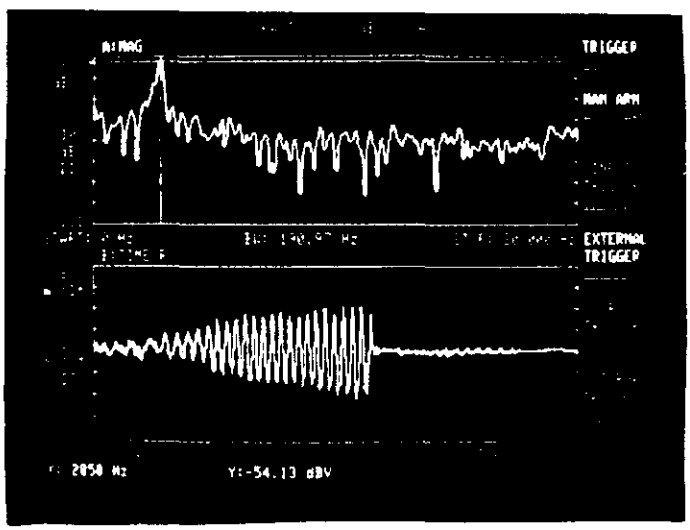

Mode 18

FIGURE 1-8

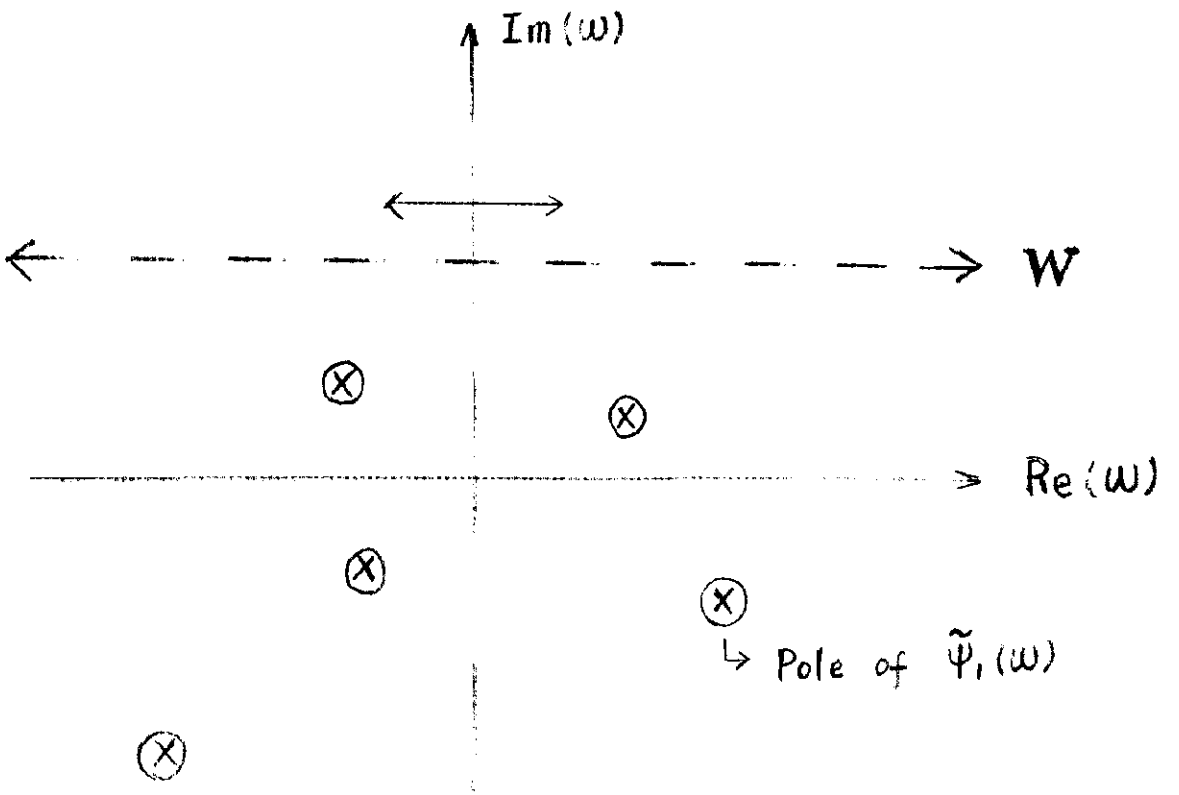

PATH OF W

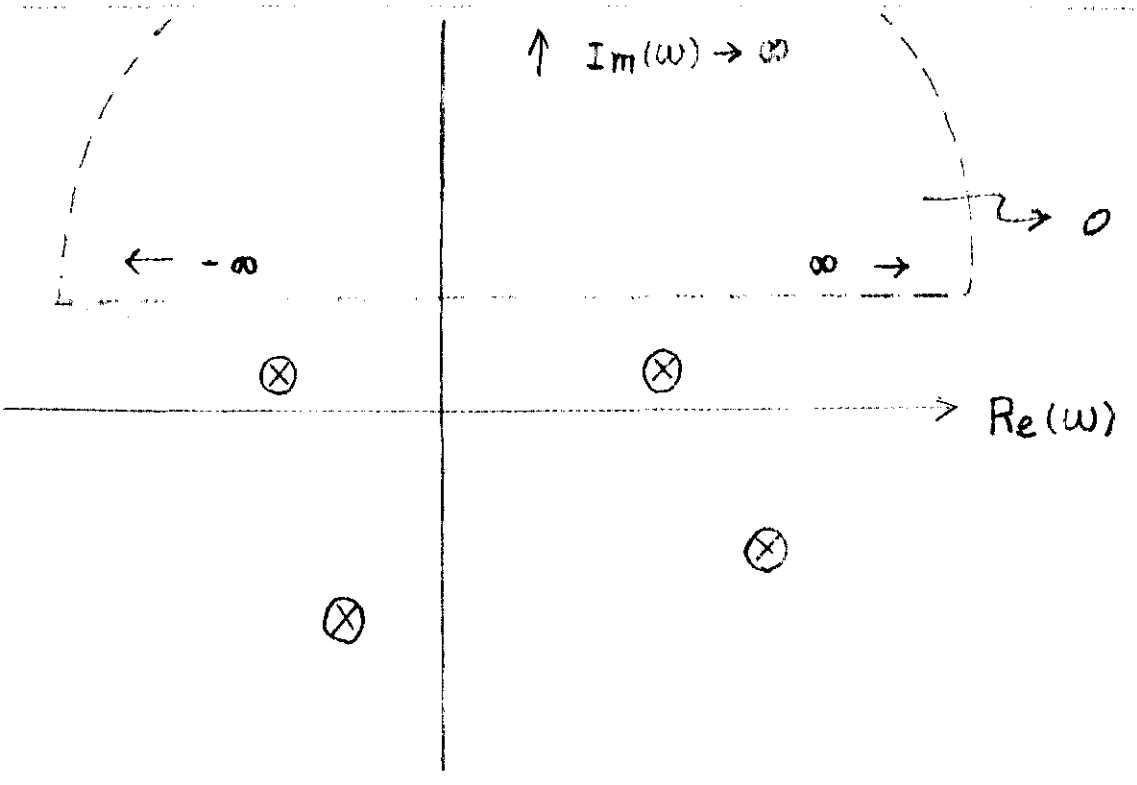

When $S<0$, Integral $= 0$

FIGURE 2-1

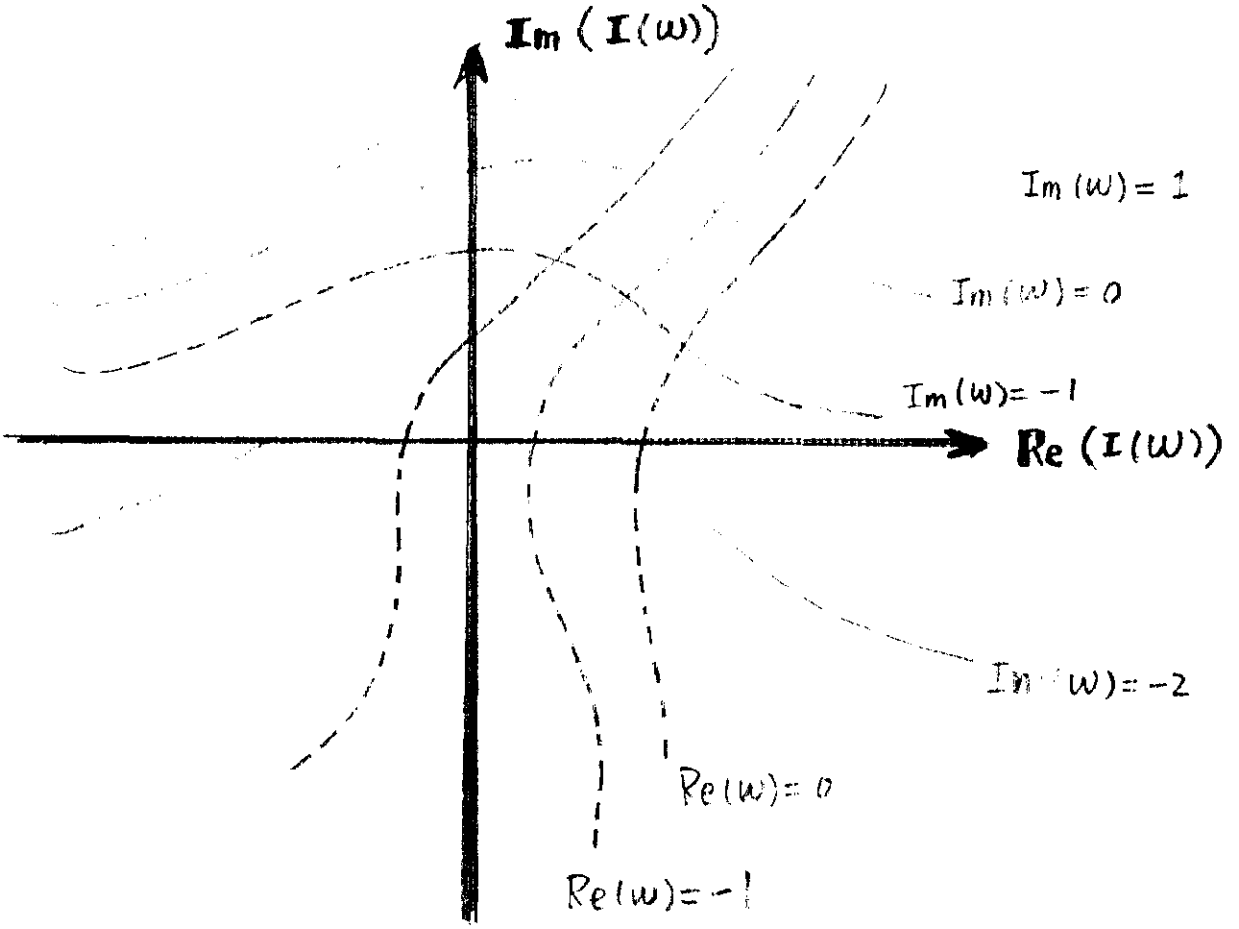

FIGURE 2-2(a)

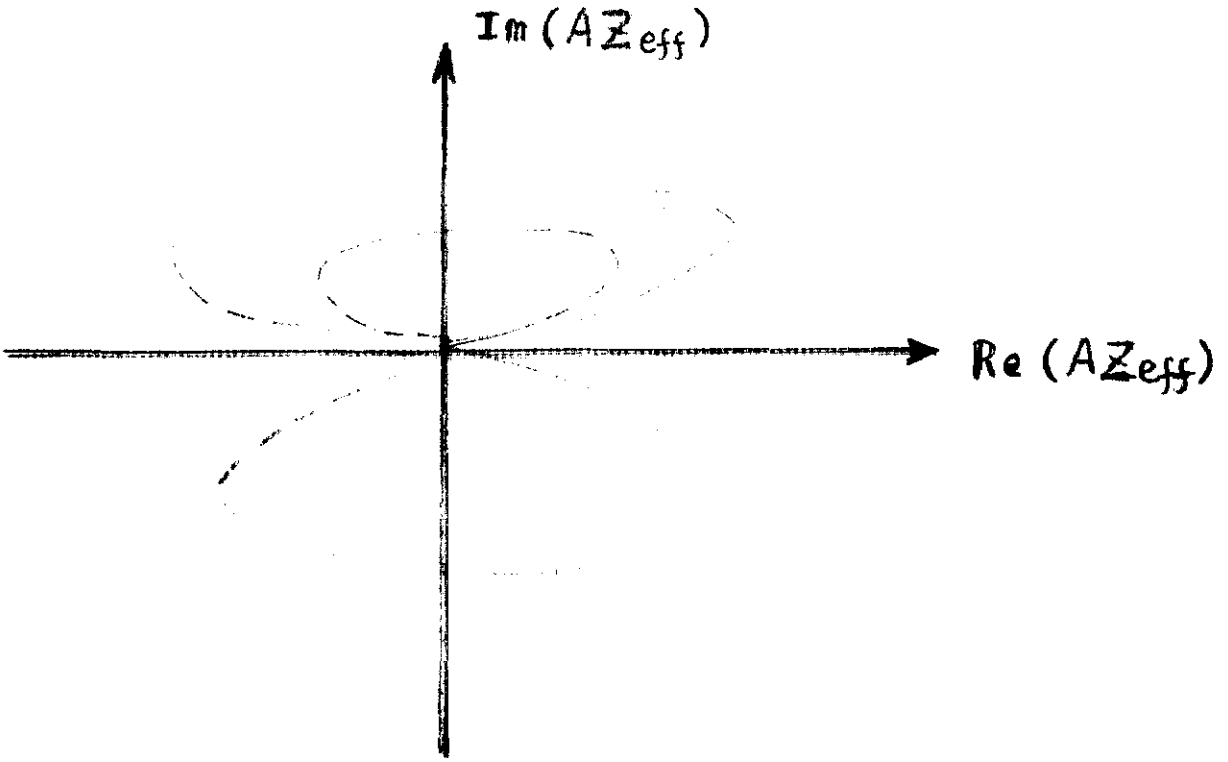

FIGURE 2-2(b)

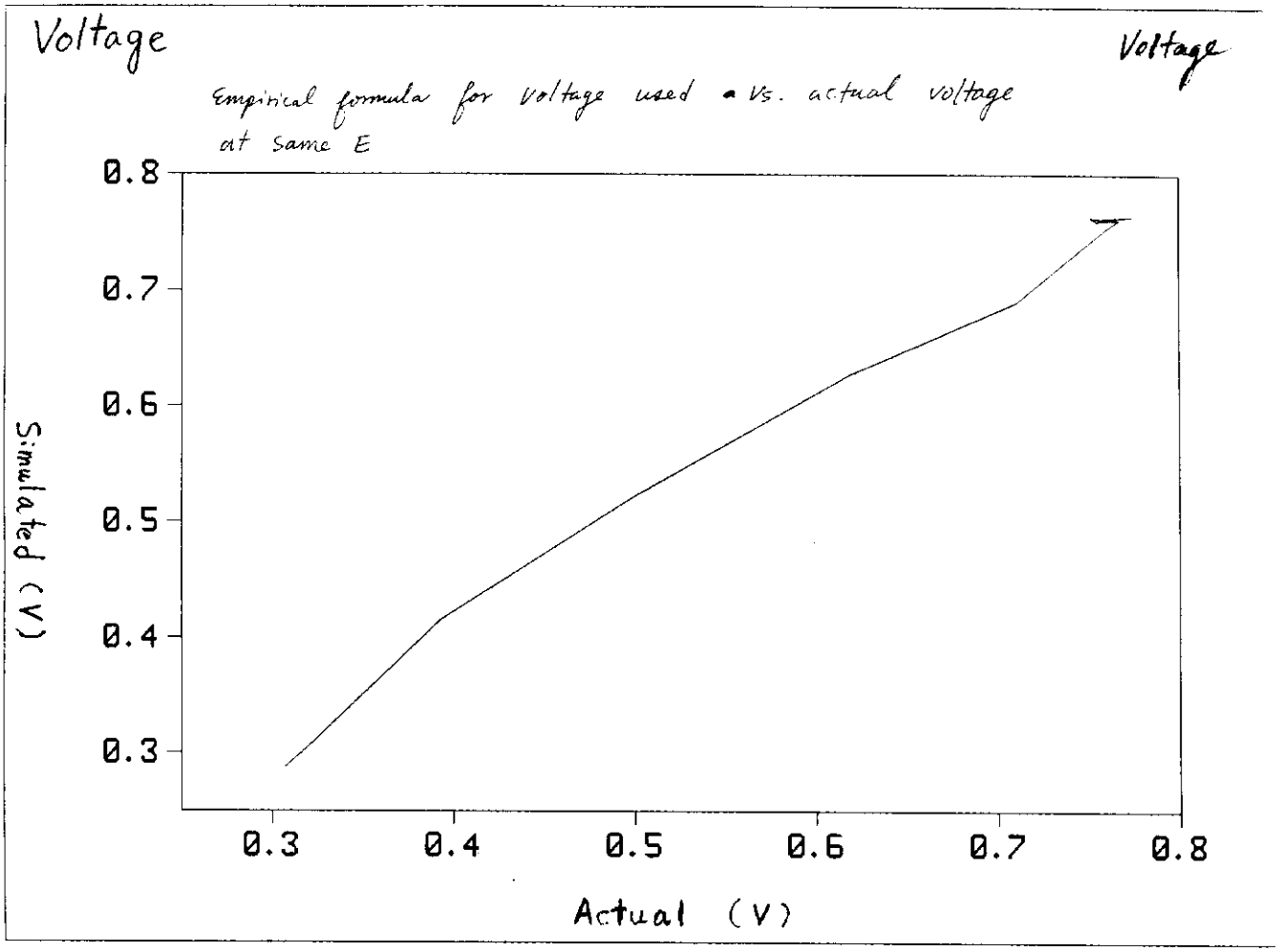
Voltage
Voltage
Empirical formula for voltage used vs. actual voltage at same E
0.8
0.7
0.6
0.5
0.4
0.3
Simulated (V)
0.3
0.4
0.5
0.6
0.7
0.8
Actual (V)

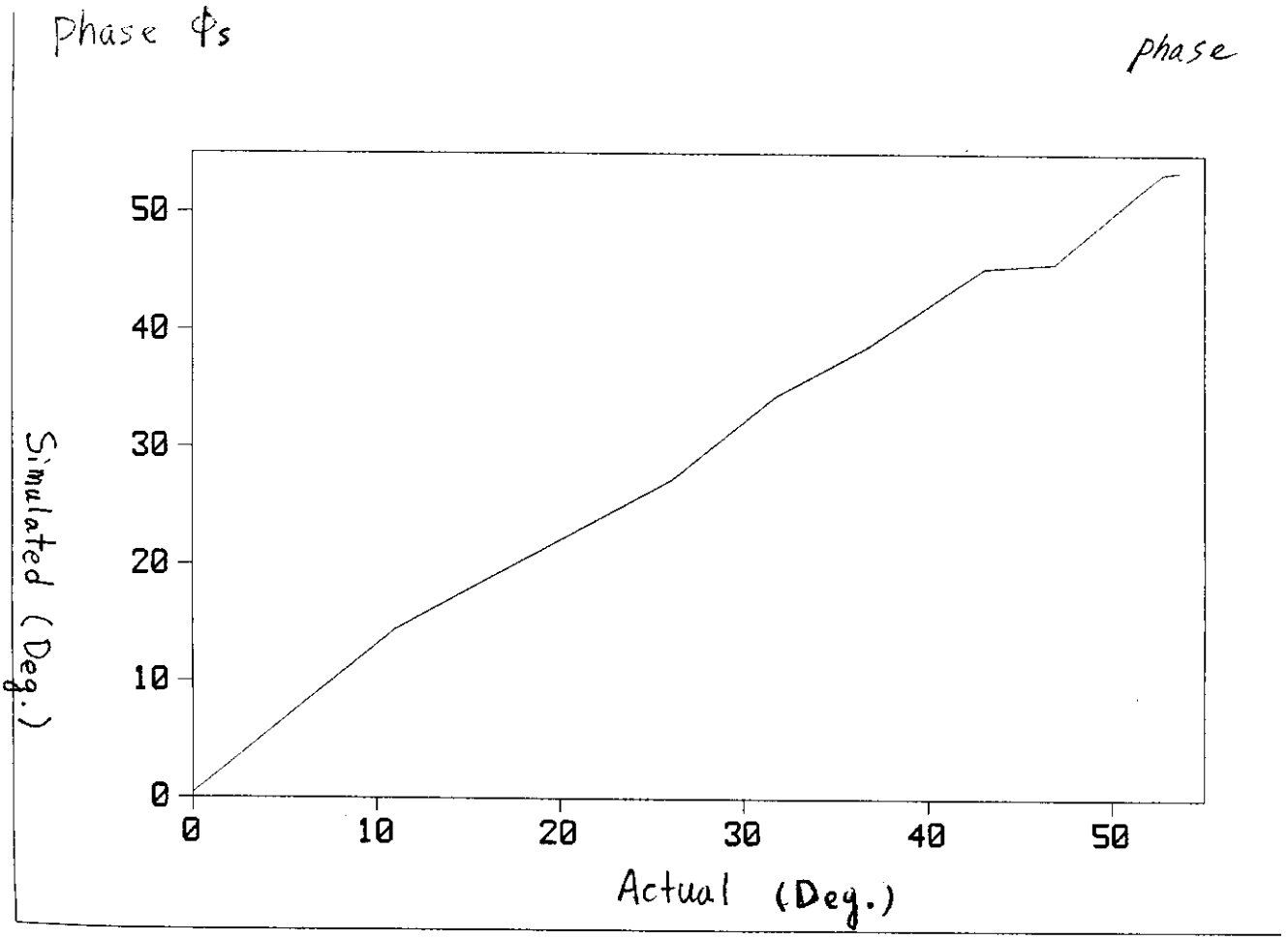
Phase ϕ_s
phase
50
40
30
20
10
0
Simulated (Deg.)
0
10
20
30
40
50
Actual (Deg.)

FIGURE 2-3

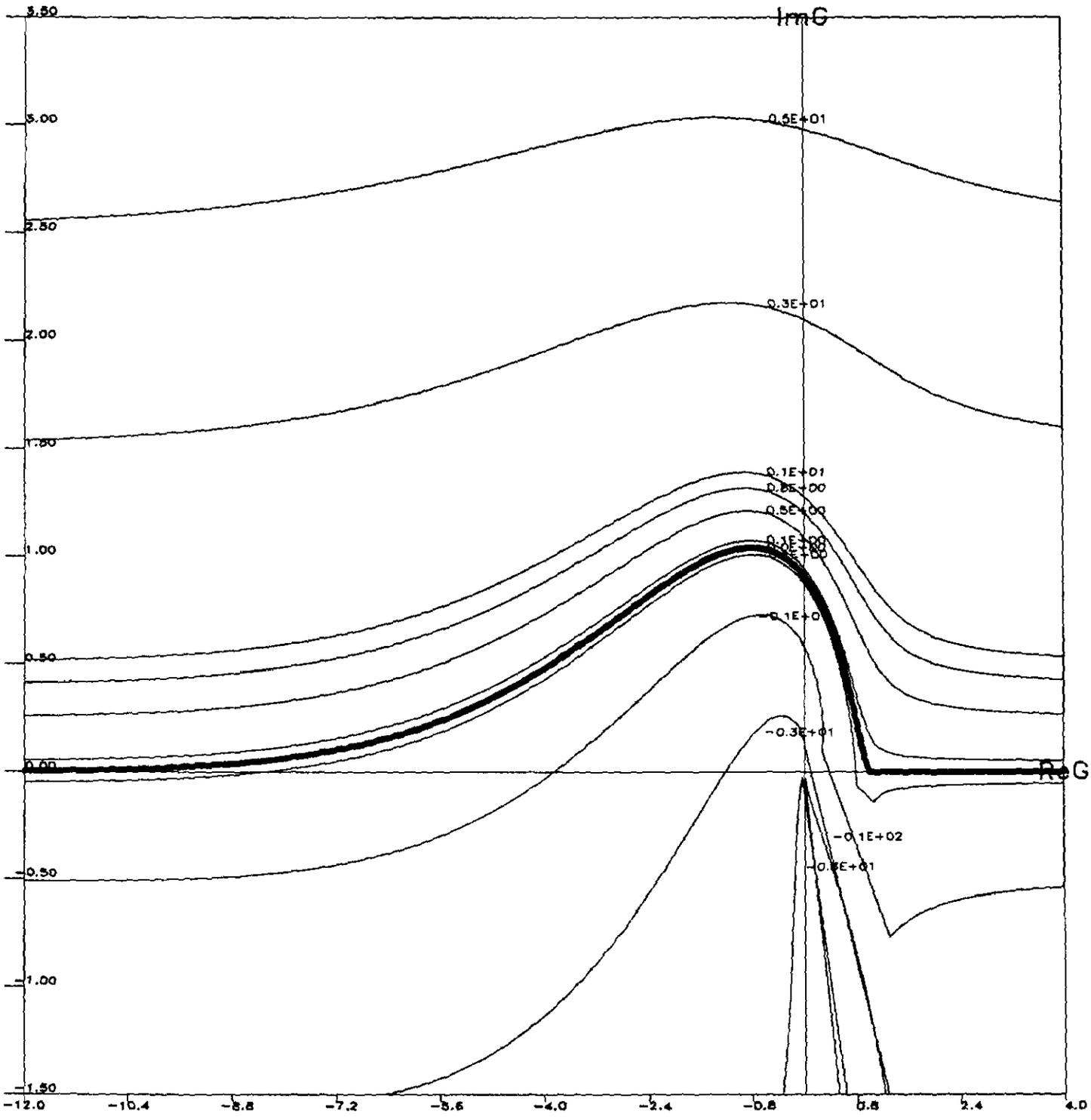
ImG
ReG
3.50
3.00
2.50
2.00
1.50
1.00
0.50
0.00
-0.50
-1.00
-1.50
-12.0
-10.4
-8.8
-7.2
-5.6
-4.0
-2.4
-0.8
0.8
2.4
4.0
0.5E+01
0.3E+01
0.1E+01
0.8E+00
0.5E+00
-0.1E+0
-0.3E+01
-0.1E+02
-0.5E+01

FIGURE 2-4

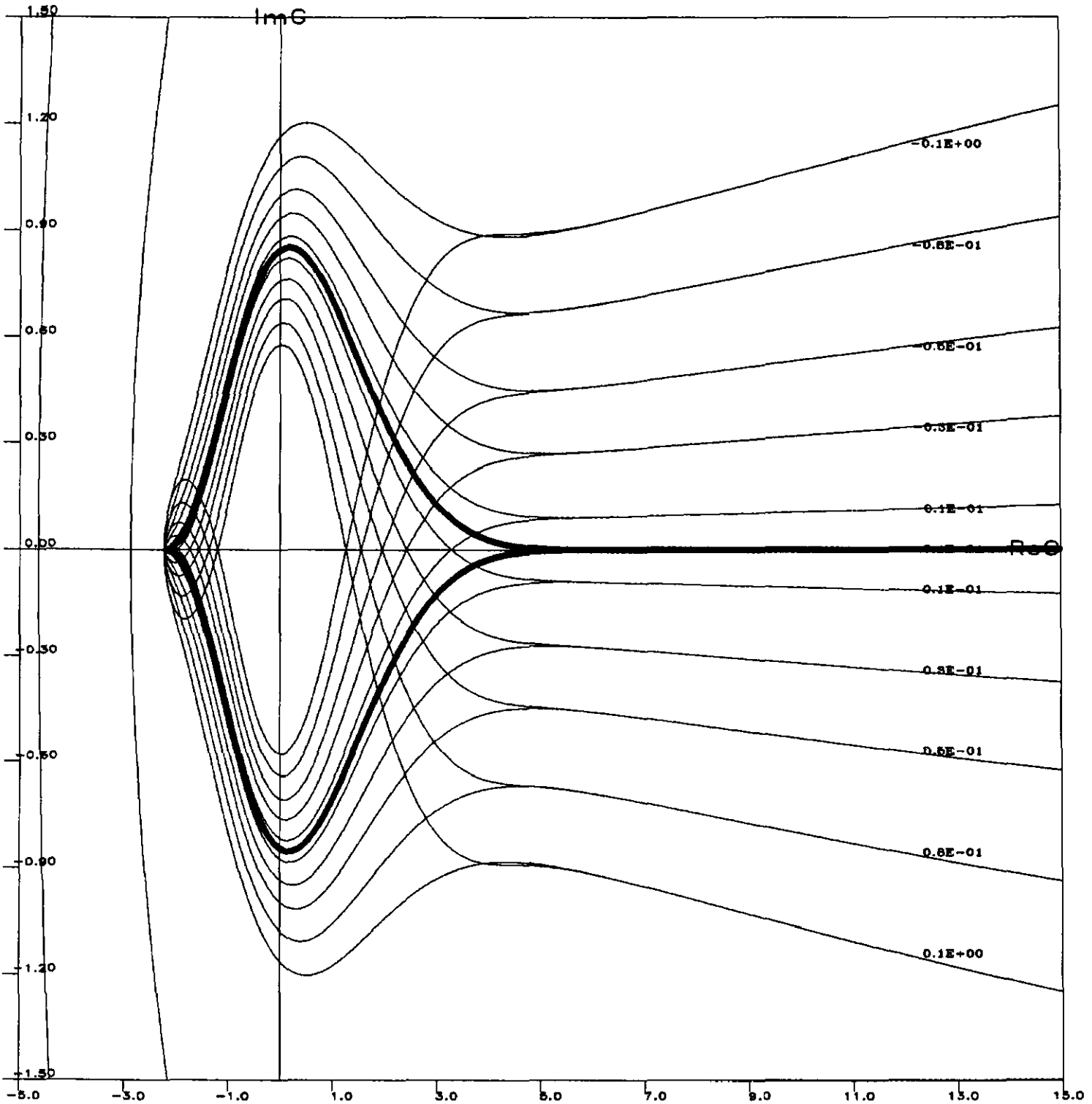
ImG
ReG
1.50
1.20
0.90
0.60
0.30
0.00
-0.30
-0.60
-0.90
-1.20
-1.50
-5.0
-3.0
-1.0
1.0
3.0
5.0
7.0
9.0
11.0
13.0
15.0
-0.1E+00
-0.8E-01
-0.6E-01
-0.3E-01
-0.1E-01
0.1E-01
0.3E-01
0.6E-01
0.8E-01
0.1E+00

FIGURE 2-5

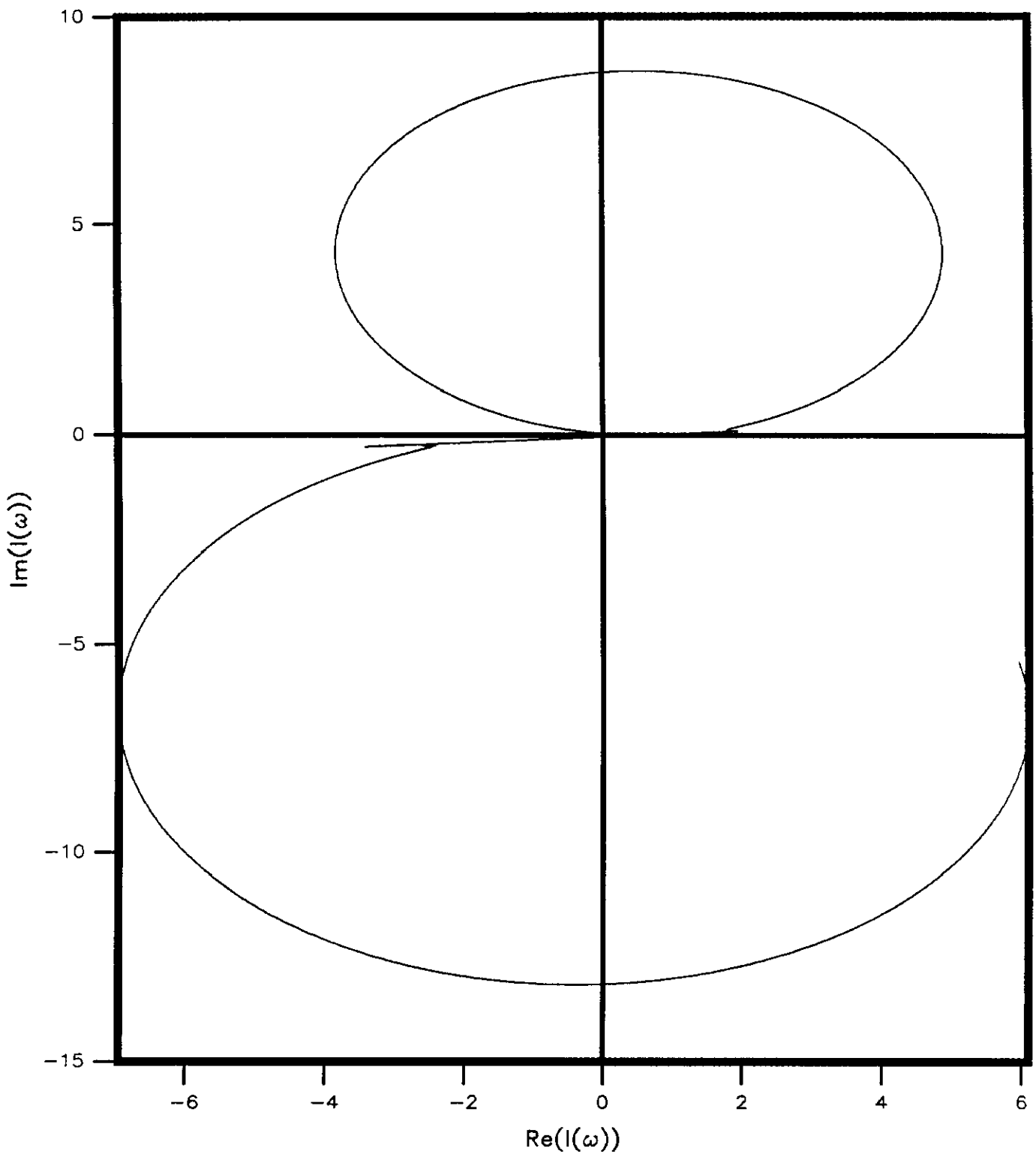

FIGURE 2-6

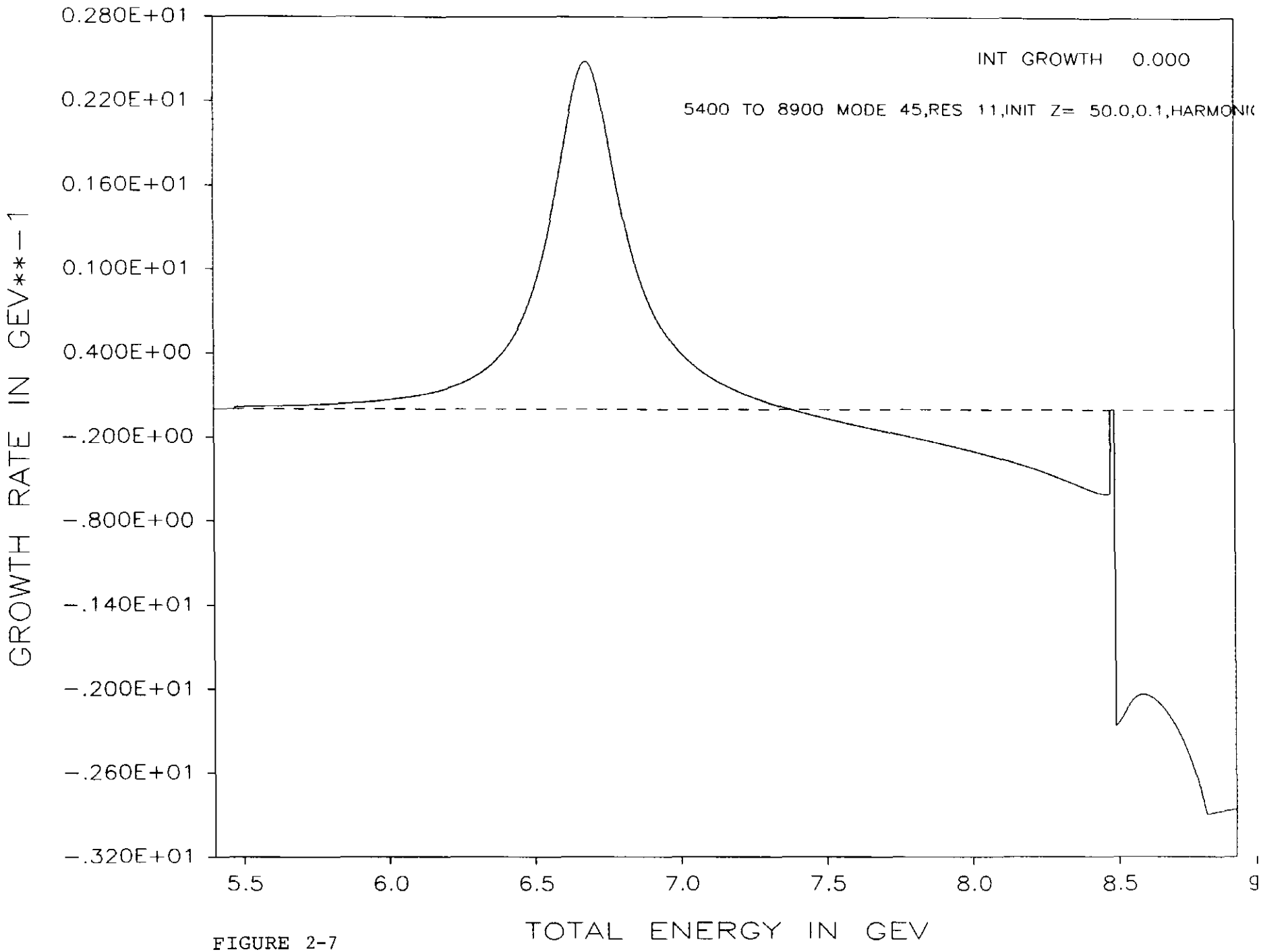
INT GROWTH 0.000
5400 TO 8900 MODE 45,RES 11,INIT Z= 50.0,0.1,HARMONI
0.280E+01
0.220E+01
0.160E+01
0.100E+01
0.400E+00
-.200E+00
-.800E+00
-.140E+01
-.200E+01
-.260E+01
-.320E+01
GROWTH RATE IN GEV**-1
5.5
6.0
6.5
7.0
7.5
8.0
8.5
TOTAL ENERGY IN GEV

FIGURE 2-7

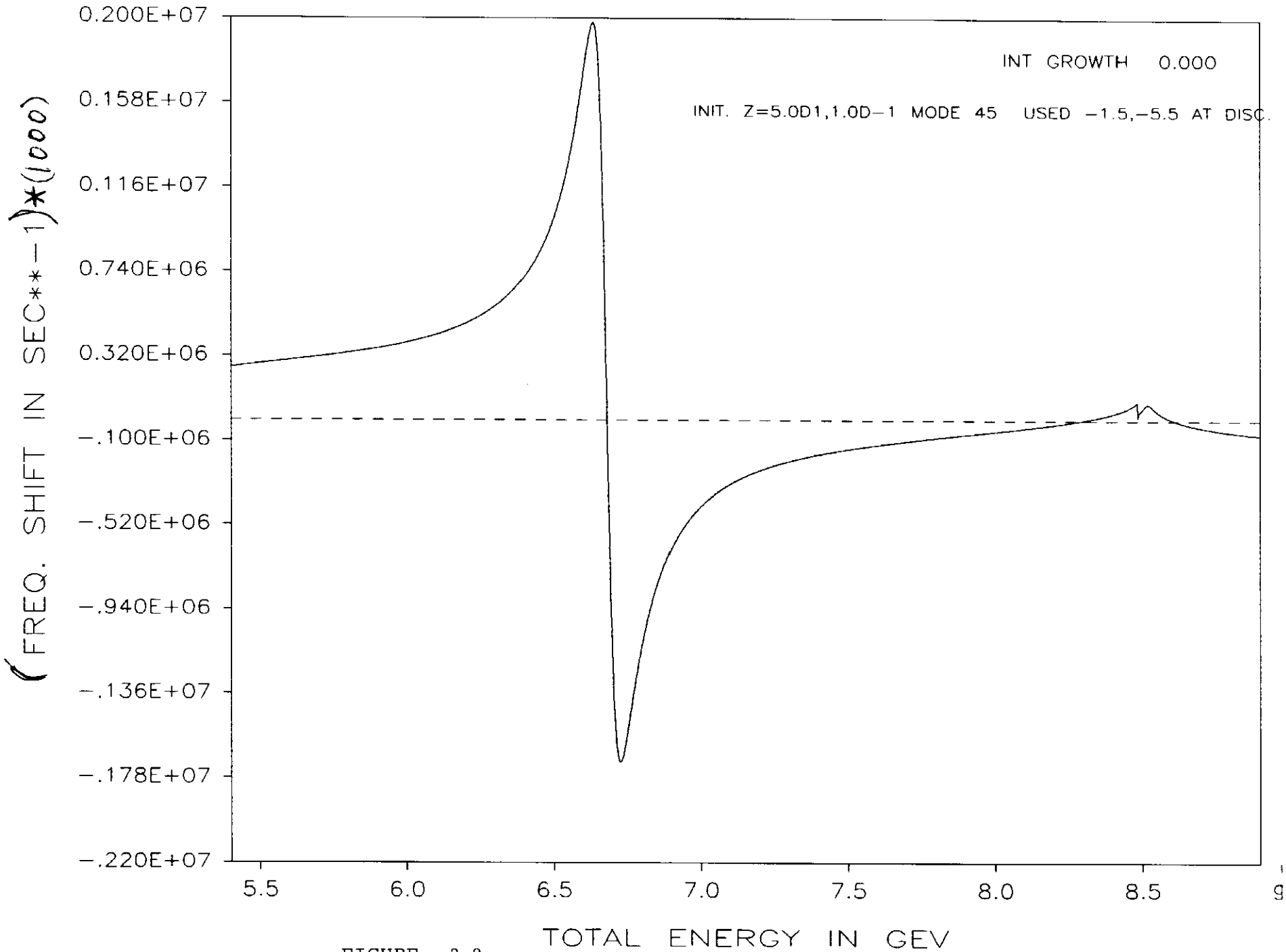
INT GROWTH 0.000
INIT. Z=5.0D1,1.0D-1 MODE 45 USED -1.5,-5.5 AT DISC.
0.200E+07
0.158E+07
0.116E+07
0.740E+06
0.320E+06
-.100E+06
-.520E+06
-.940E+06
-.136E+07
-.178E+07
-.220E+07
(FREQ. SHIFT IN SEC**-1)*(1000)
5.5
6.0
6.5
7.0
7.5
8.0
8.5
TOTAL ENERGY IN GEV

FIGURE 2-8

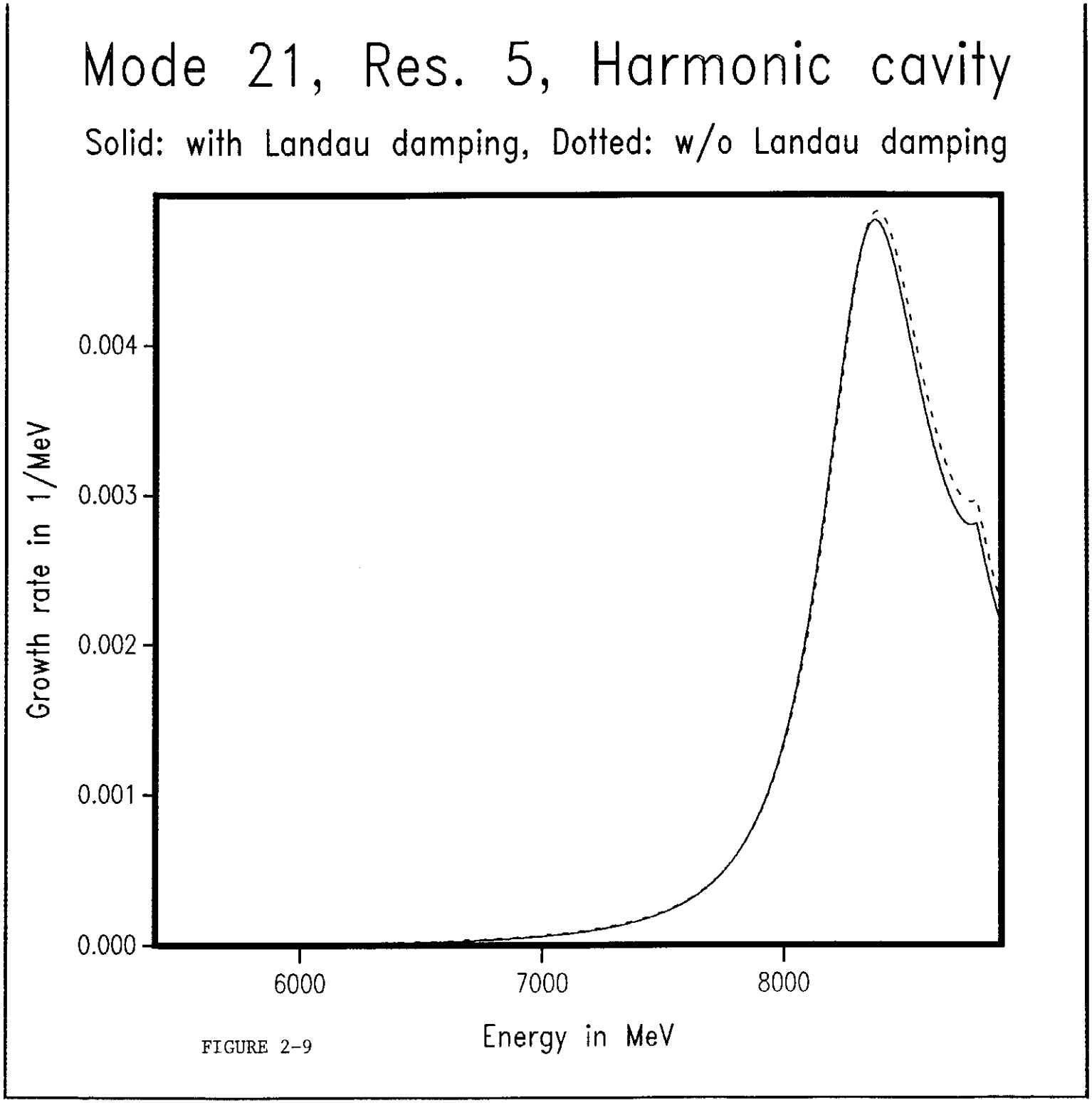
Mode 21, Res. 5, Harmonic cavity
Solid: with Landau damping, Dotted: w/o Landau damping
Growth rate in 1/MeV
0.004
0.003
0.002
0.001
0.000
6000
7000
8000
Energy in MeV

FIGURE 2-9

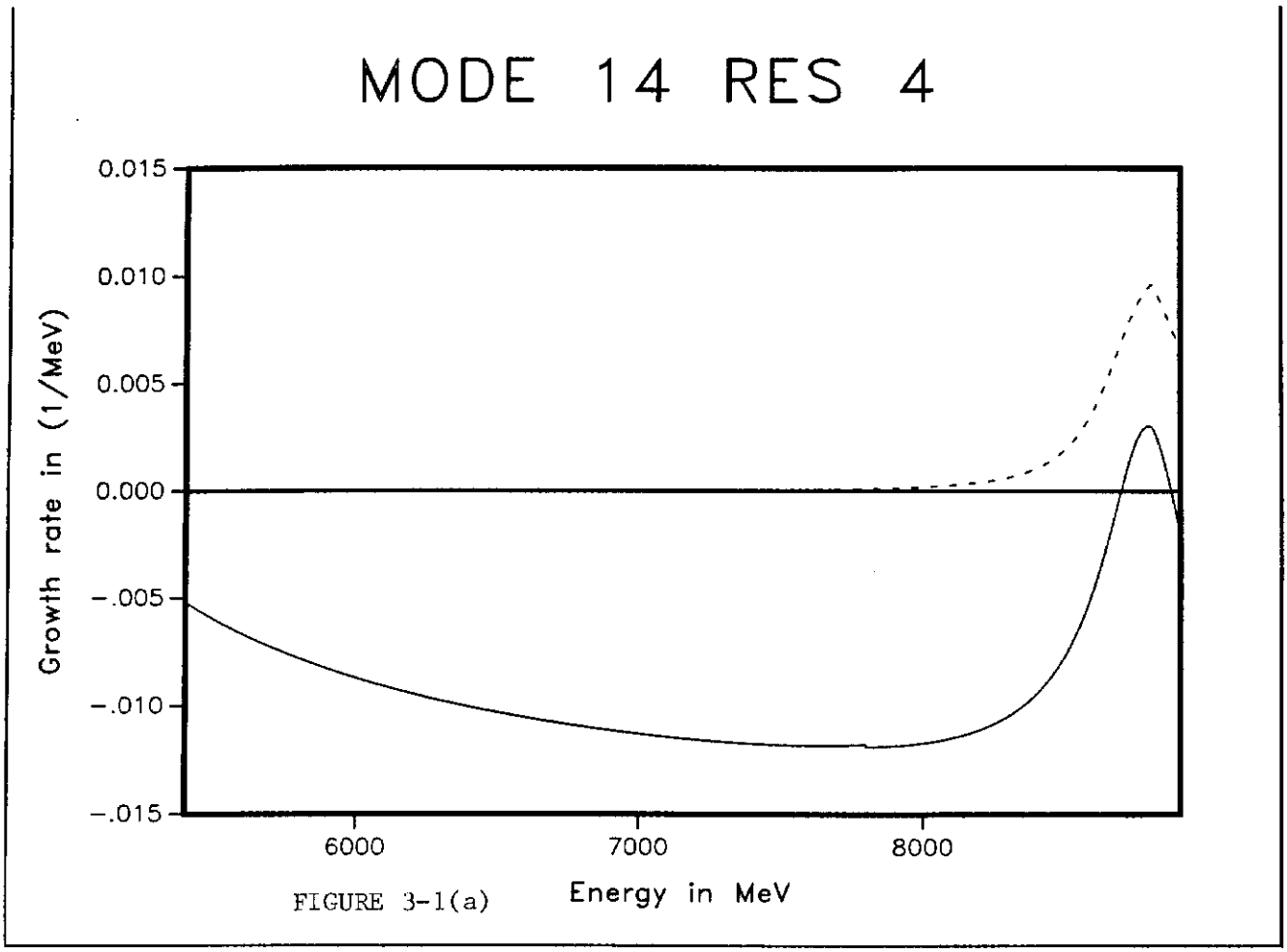

FIGURE 3-1(a)

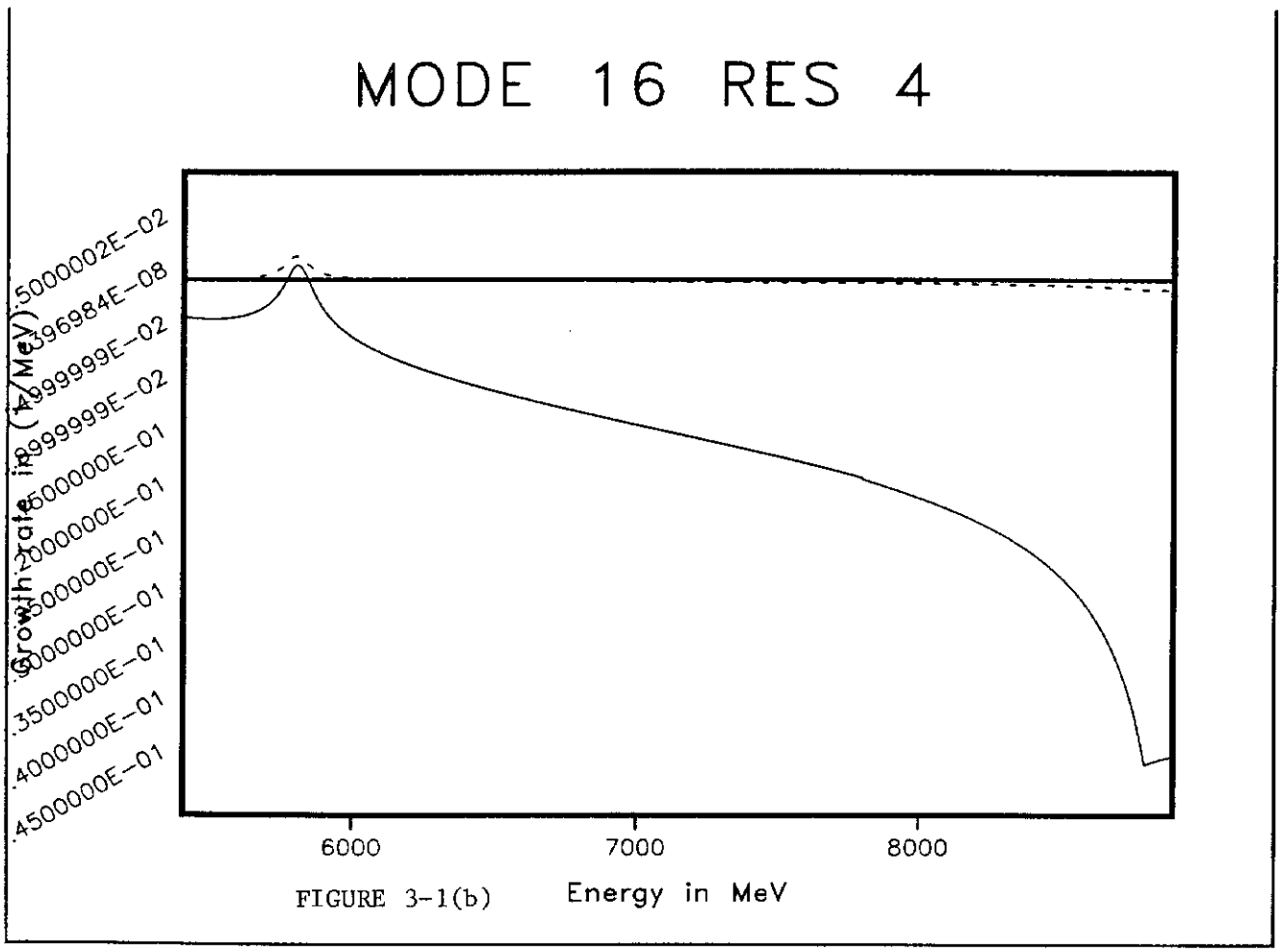

FIGURE 3-1(b)

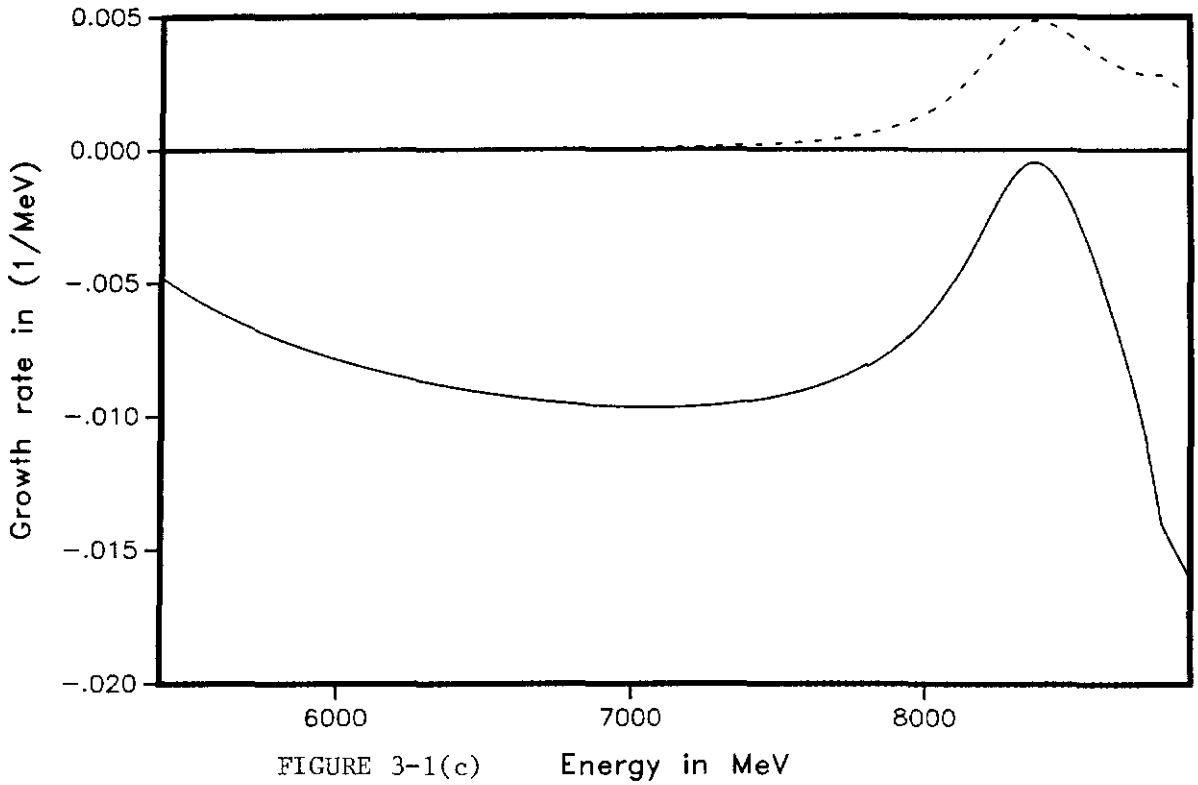

FIGURE 3-1(c)

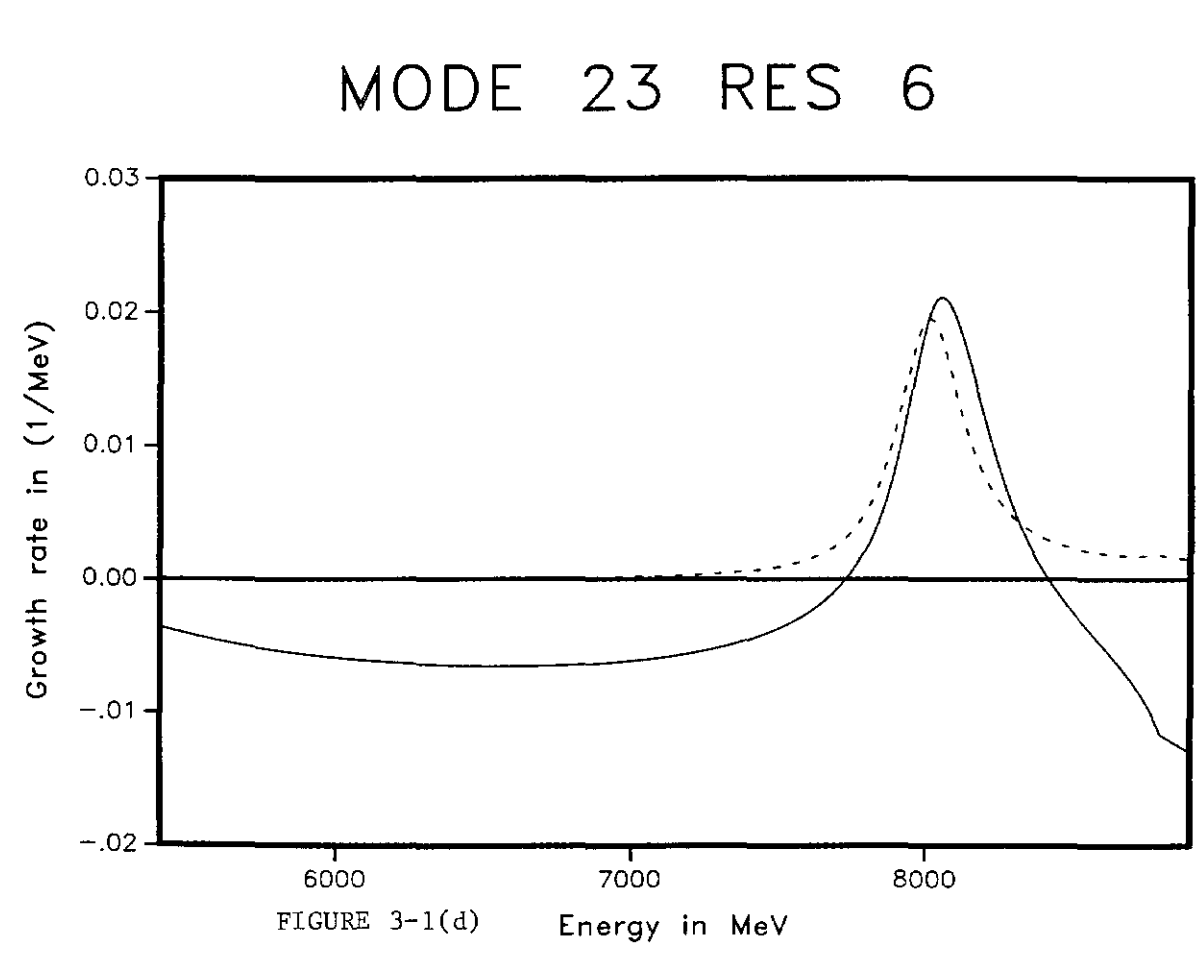

FIGURE 3-1(d)

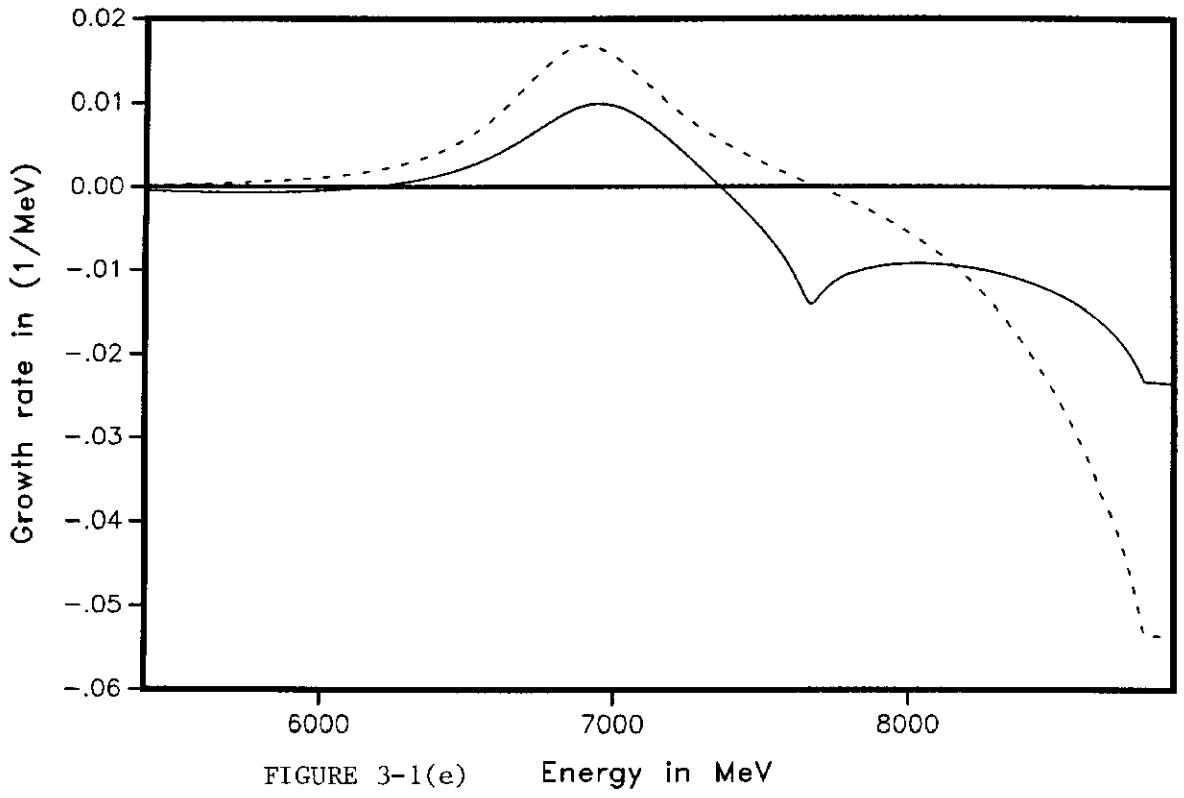

FIGURE 3-1(e)

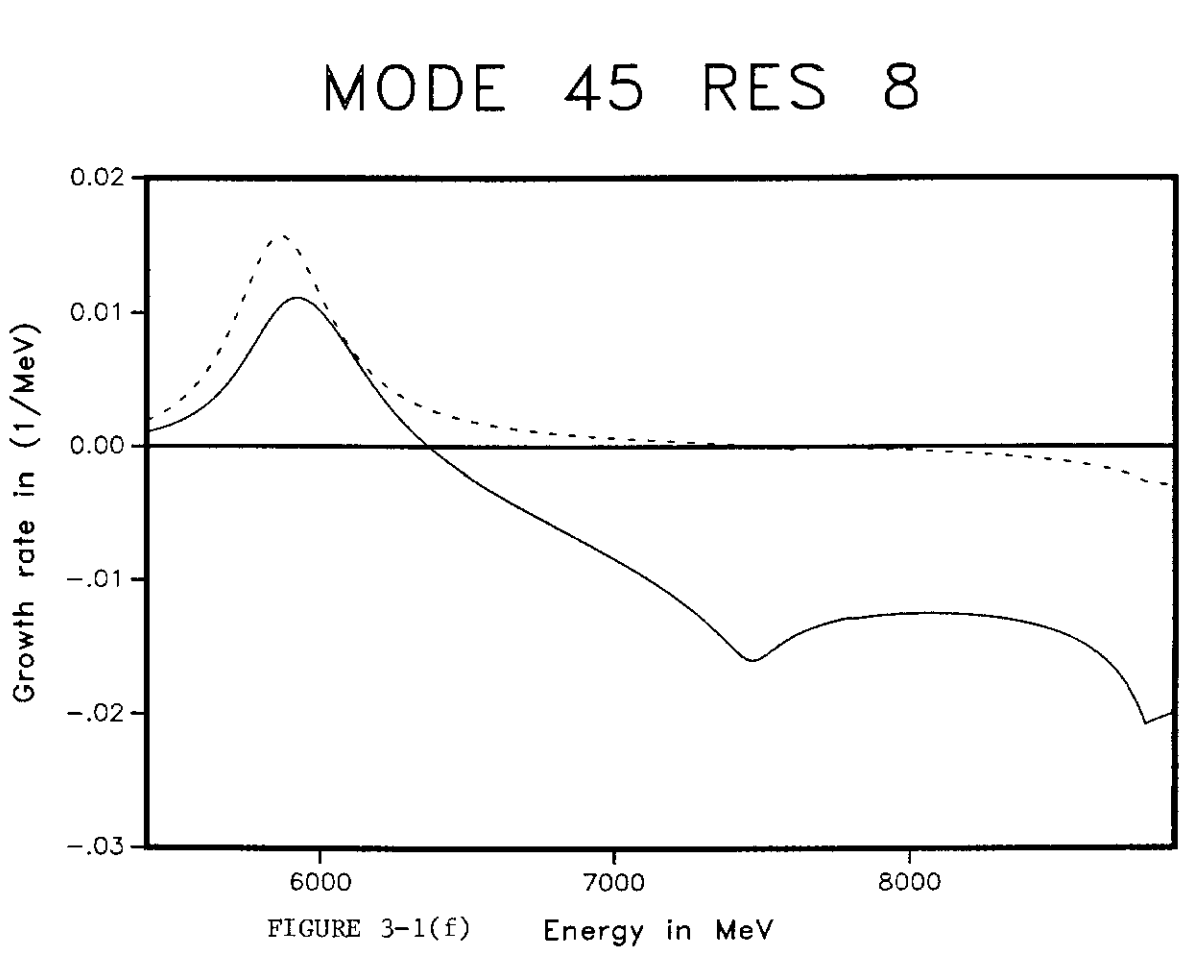

FIGURE 3-1(f)

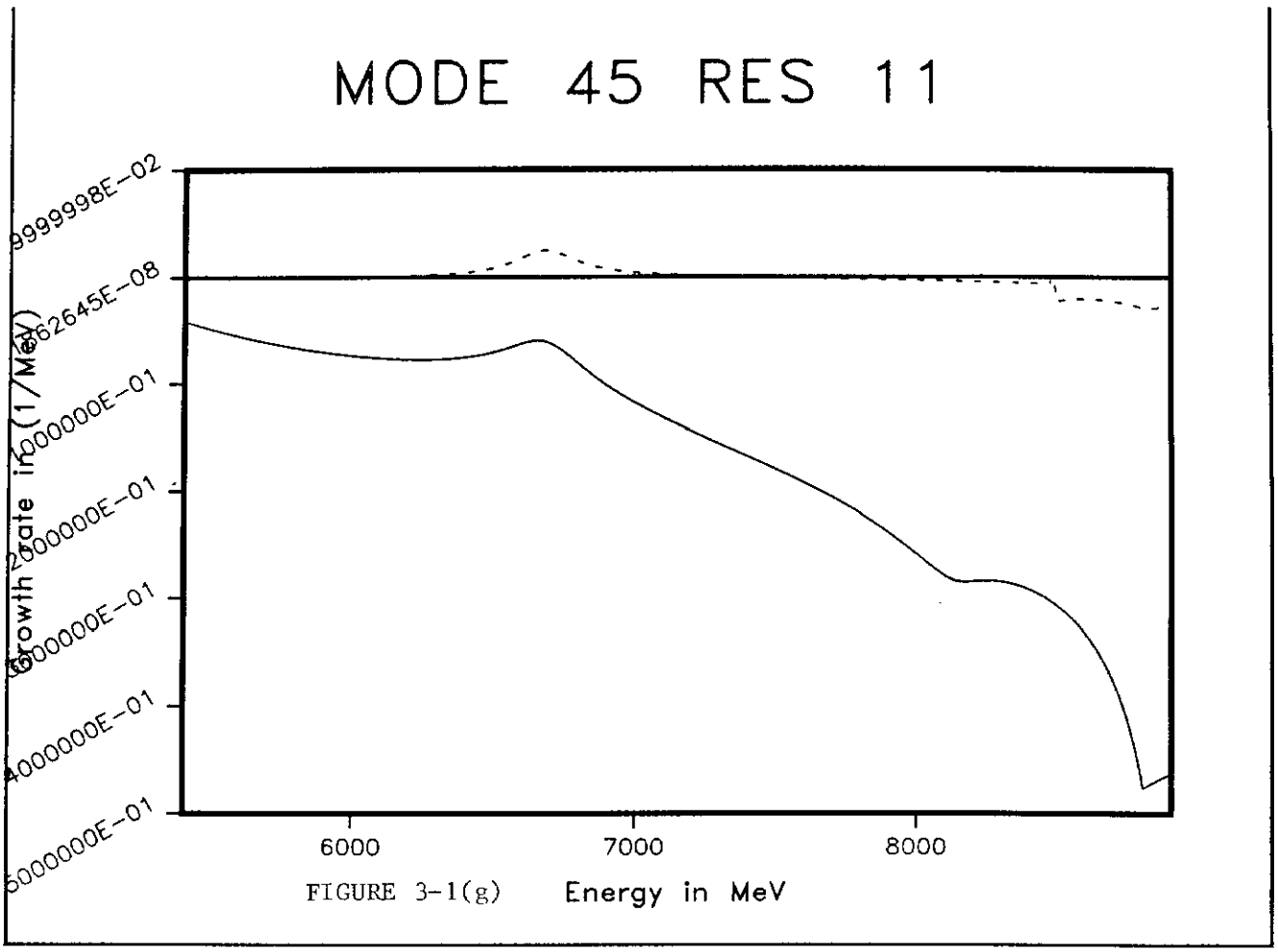

FIGURE 3-1(g)

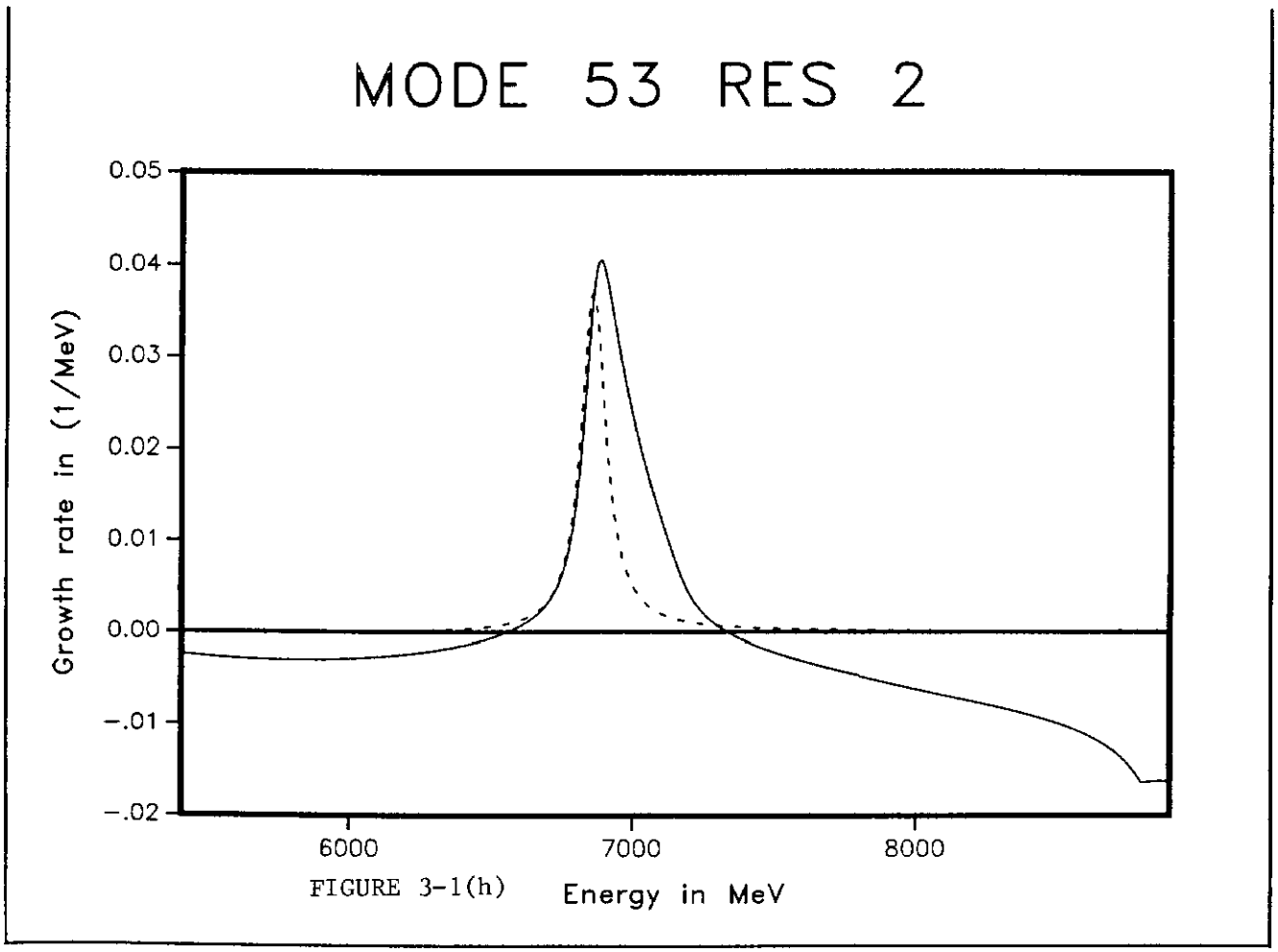

FIGURE 3-1(h)

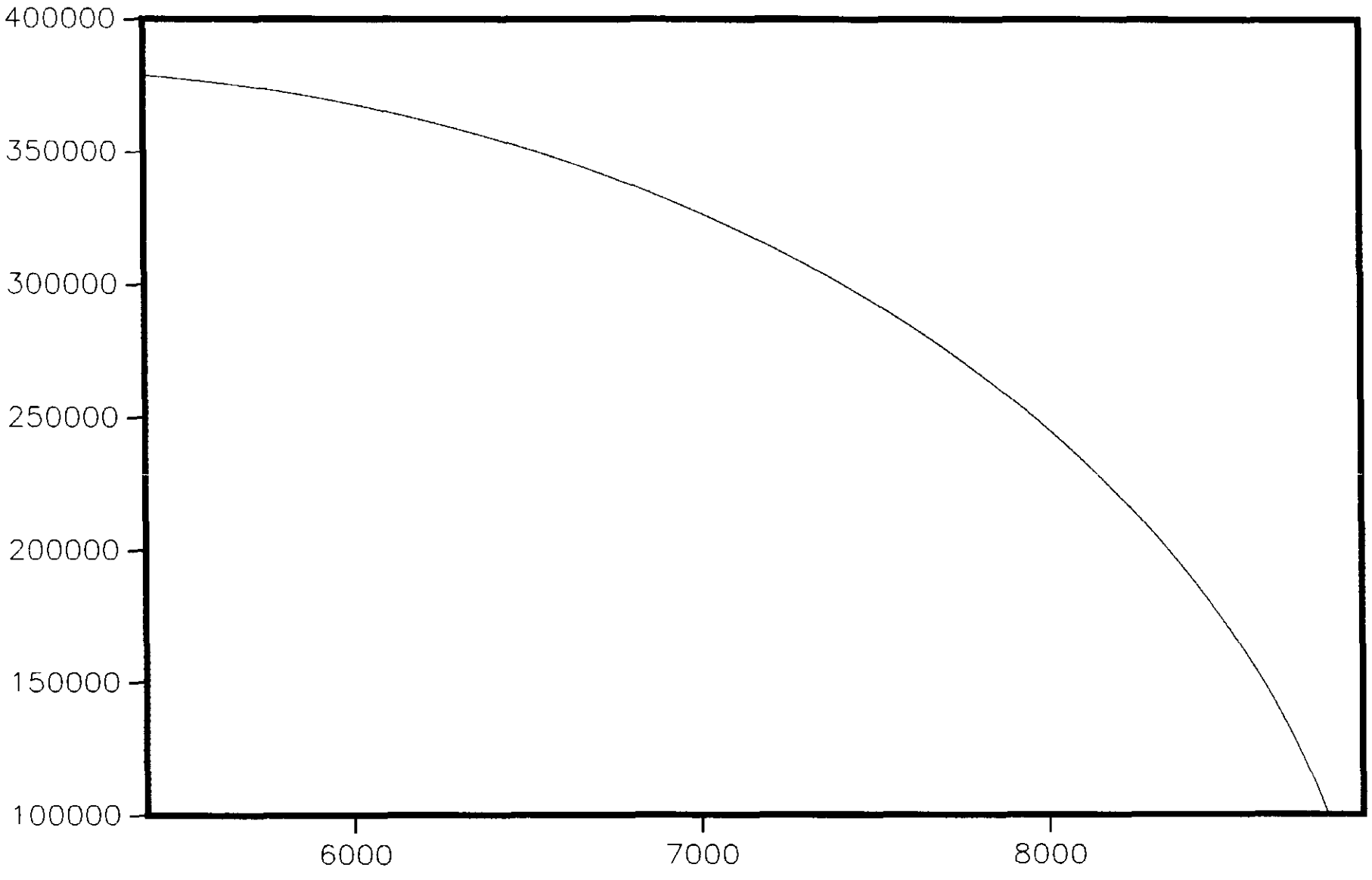
dE/dt vs. E (in terms of MeV/sec vs. Mev)
400000
350000
300000
250000
200000
150000
100000
6000
7000
8000

FIGURE 3-2

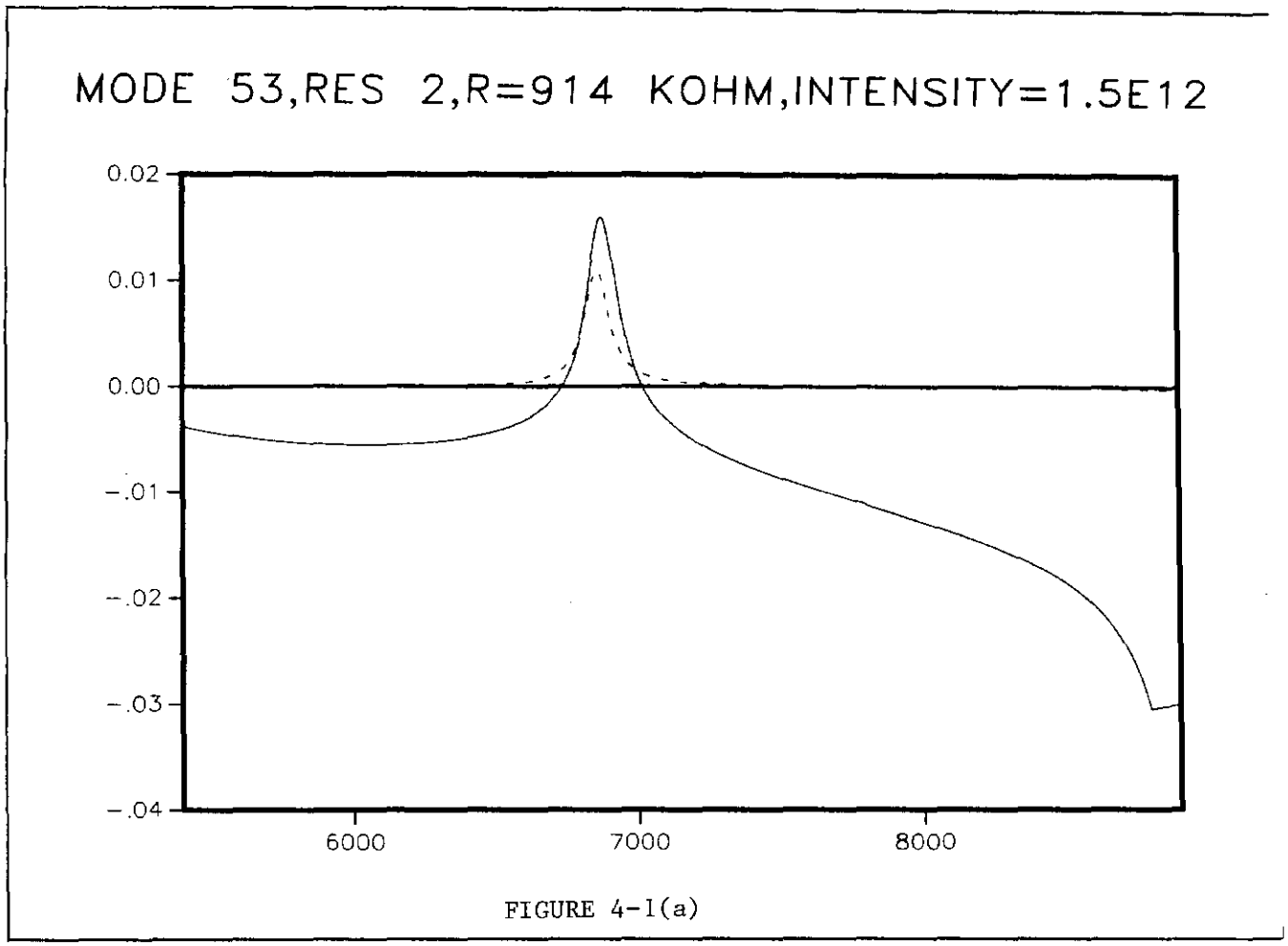

FIGURE 4-1(a)

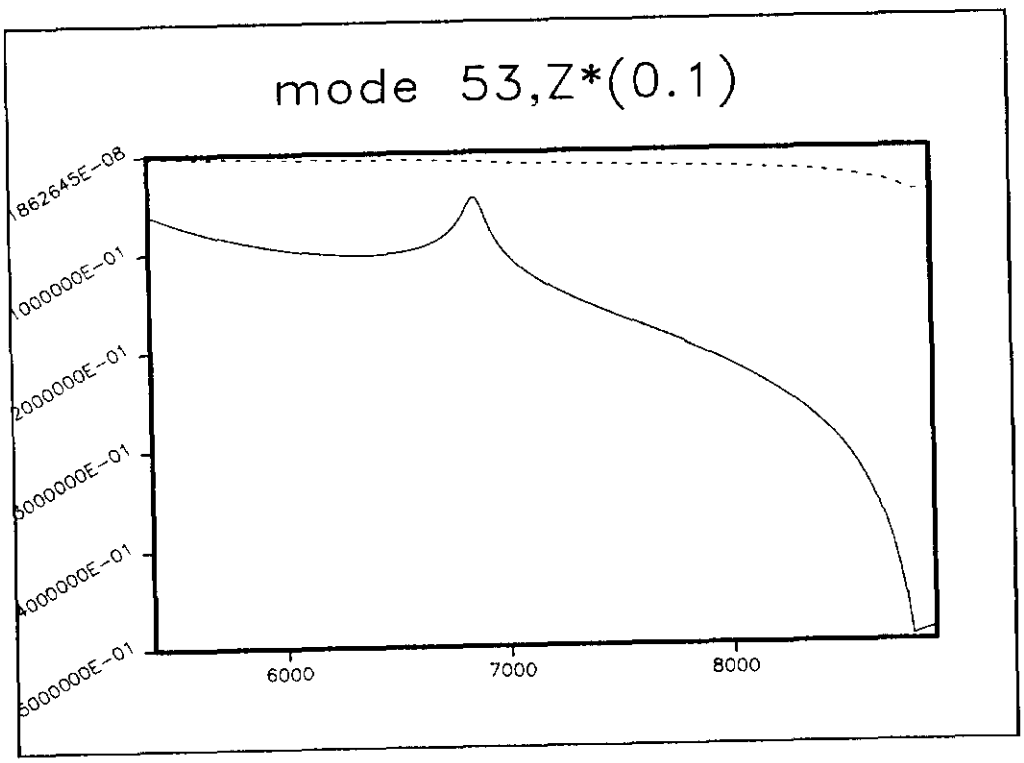

FIGURE 4-1(b)

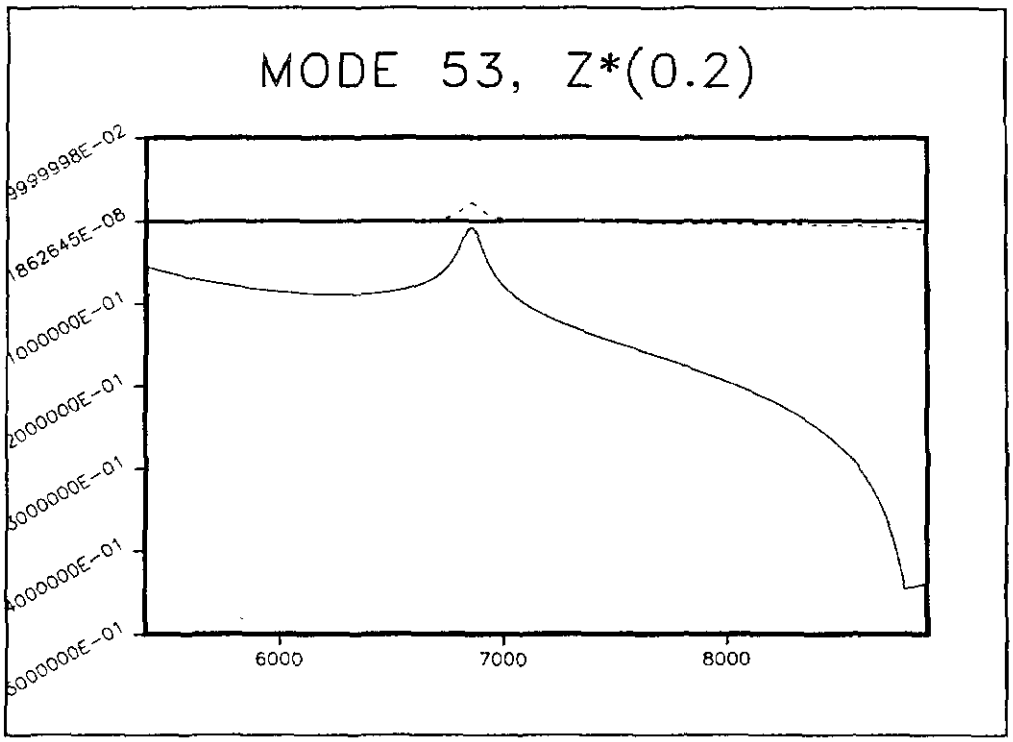

FIGURE 4-1(c)

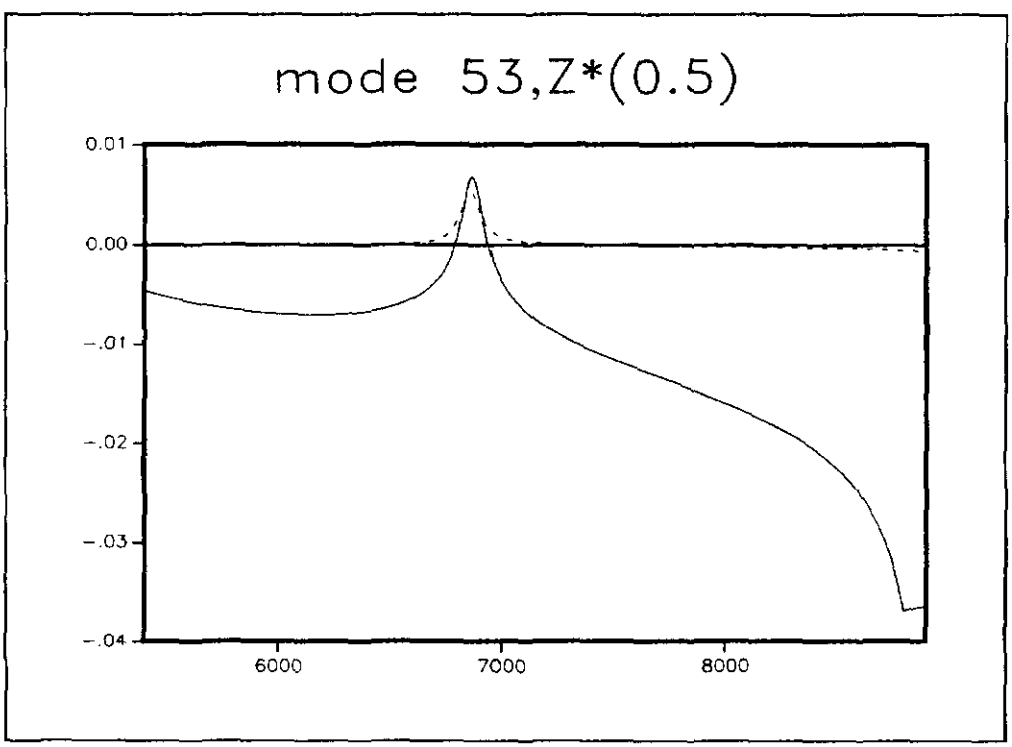

FIGURE 4-1(d)

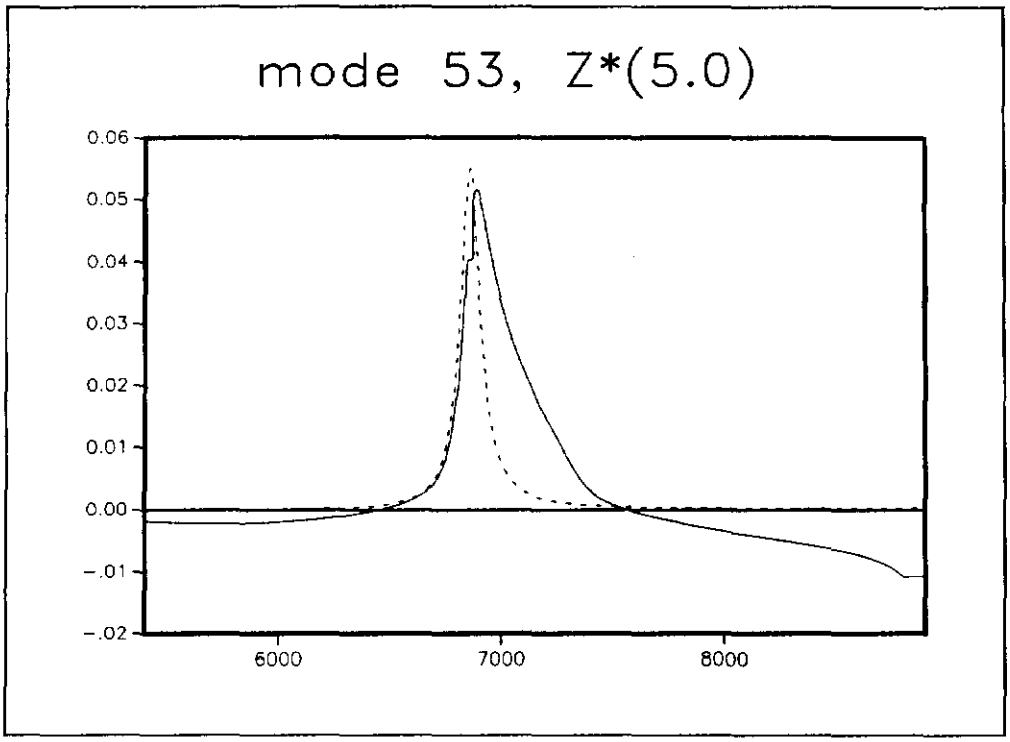

FIGURE 4-1(e)

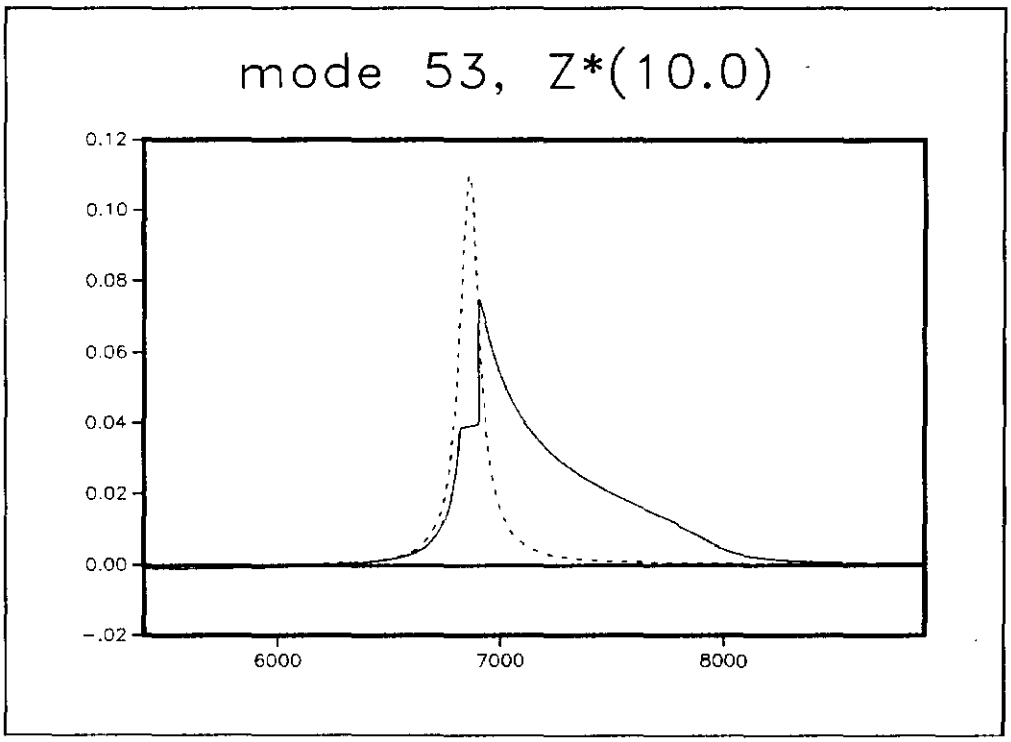

FIGURE 4-1(f)

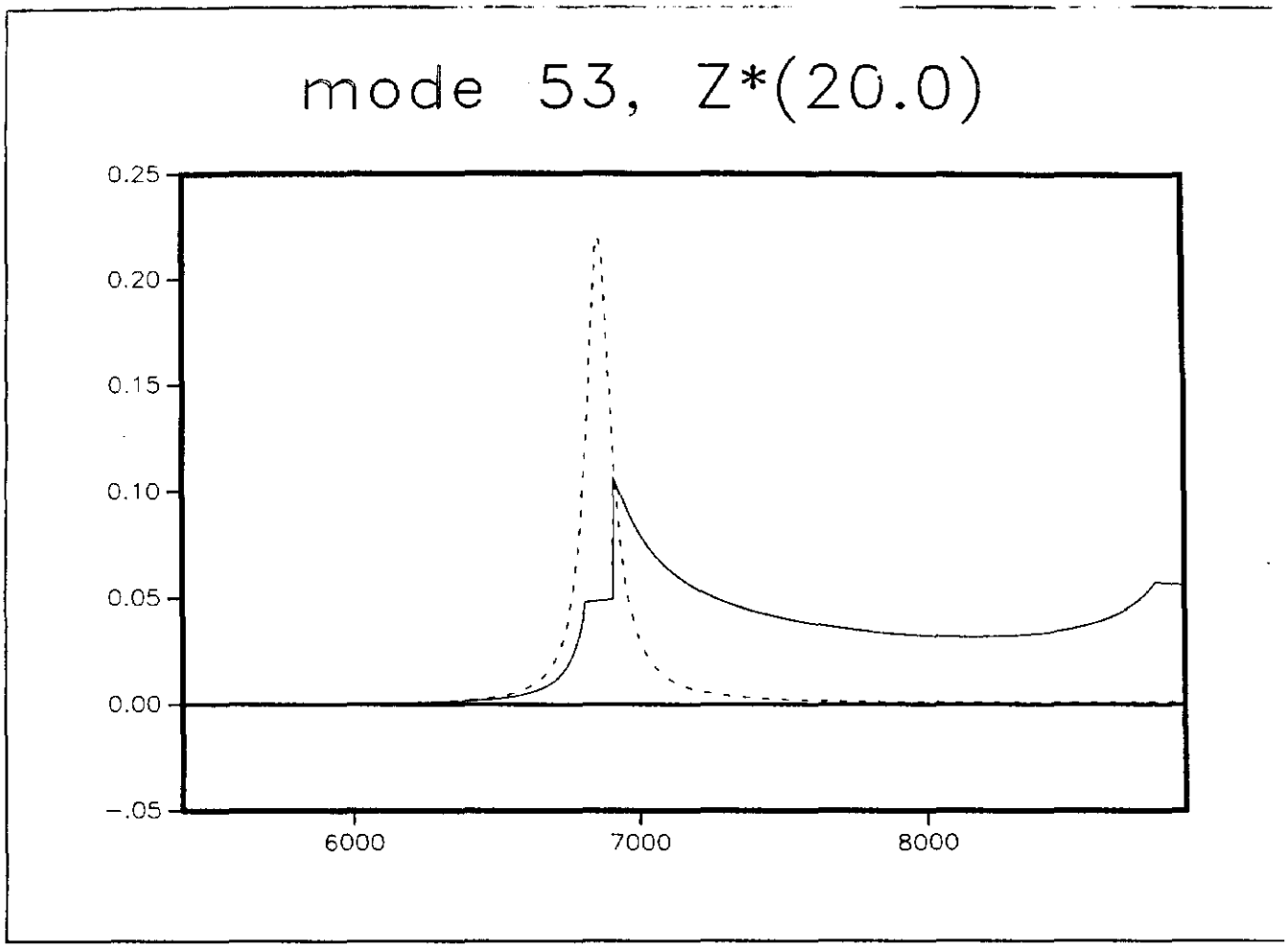

FIGURE 4-1(g)

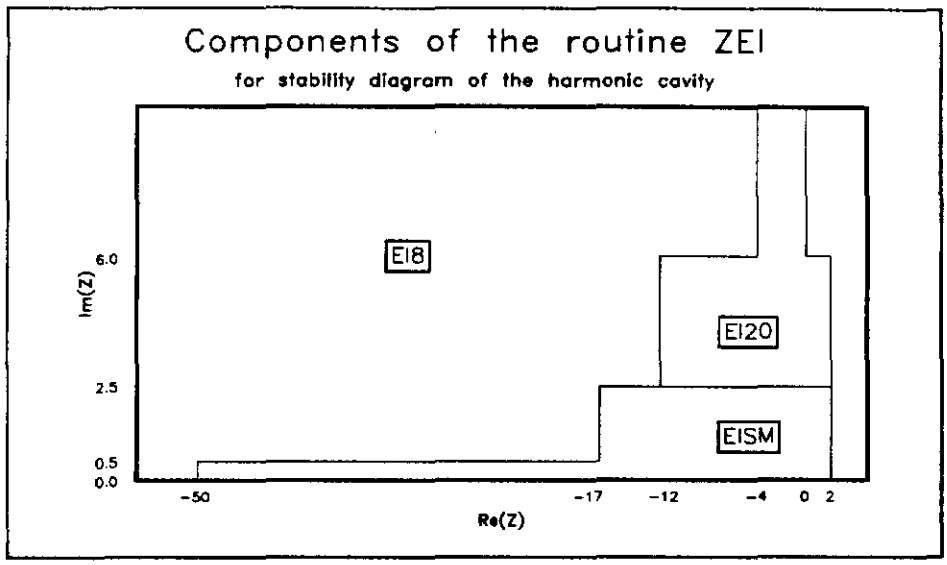

FIGURE A-1

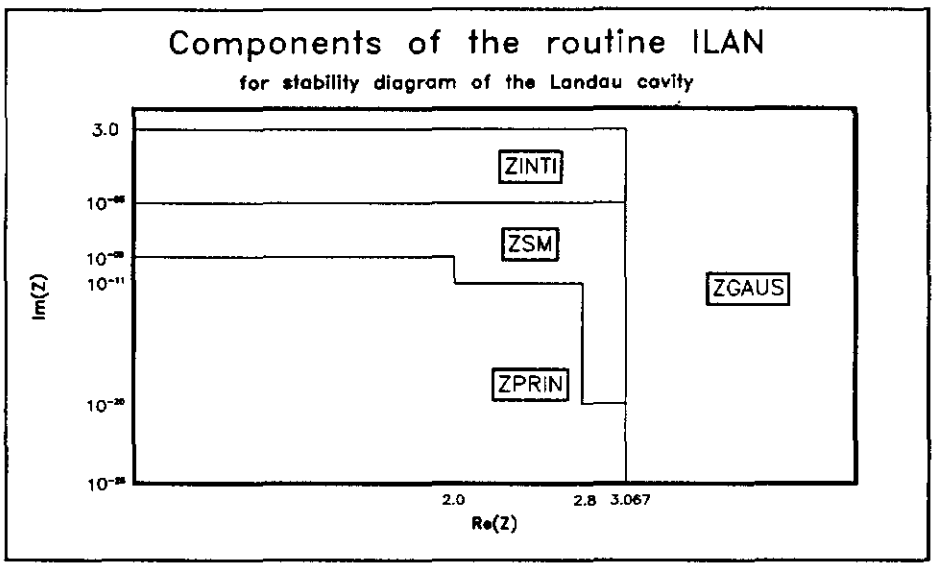

FIGURE A-2

TABLES

Resonance Number	Frequency (MHz)	Shunt Impedance (MΩ)	Q
1	52.3	0.43	1307
2	85.8	1.56	3380
3	109.7	0.15	2258
4	167.2	0.07	1960
5	171.5	0.07	1190
6	225.4	0.33	2090
7	318.1	0.09	1570
8	342.6	0.50	530
9	391.0	0.11	460
10	448.8	0.48	3590
11	448.8	0.11	1206
12	559.7	0.07	430
13	685.9	0.71	2440

Table 1: Measured resonant frequency, shunt impedance, and Q of the Booster accelerating cavities.

Mode μ	Average Growth rate in ms^{-1}	Driving Resonances	Mode μ	Average Growth rate in ms^{-1}	Driving Resonances
0	0.	(13)	34	0.793	(9)
1	0.563	(13)	35	0.618	(9)
2	0.695	(7,**13**)	36	0.506	(9)
3	0.579	(7,**13**)	37	0.429	(9)
4	0.526	(7,**13**)	38	0.371	(9)
5	0.474	(7,**13**)	39	0.326	(9)
6	0.430	(7,**13**)	40	0.288	(9)
7	0.737	(3,7,**13**)	41	3.208	(**8**,9)
8	0.404	(3,7,**13**)	42	0.	(**8**,10,11)
9	0.284	(13)	43	2.344	(**8**,10,11)
10	0.267	(13)	44	2.033	(**8**,10,11)
11	0.252	(13)	45	1.780	(**8**,10,11)
12	0.238	(13)	46	1.548	(**8**,10,11)
13			47	1.382	(**8**,10,11)
14	0.074	(4)	48	0.314	(**10**,11)
15	0.045	(4)	49	0.285	(**10**,11)
16	0.032	(4)	50	0.263	(**10**,11)
17	0.025	(4)	51	0.472	(12)
18			52	1.111	(2,**12**)
19			53	0.568	(2,**12**)
20			54	0.311	(12)
21	0.106	(5)	55	0.279	(12)
22	0.067	(5)	56	0.253	(12)
23	0.372	(5,**6**)	57	0.231	(12)
24	0.269	(5,**6**)	58	0.213	(12)
25	0.179	(6)	59	0.197	(12)
26	0.147	(6)	60	0.184	(12)
27			61	0.172	(12)
.			.		
.			.		
.			83	0.751	(13)

Table 2: Average growth rate for each mode μ. When there are more than one responsible driving resonance, the one that contributes the most is bold-faced.

Radius	75.472 M
No. of bunches	84
No. of proton per bunch	3.50E+10
Bunch area	0.0250 eV-sec
γ_t	5.373

Table 3: Fermilab Booster parameters. Stationary buckets are assumed. The particle momentum follows the curve described below:

$$P = A - B \cos G(T - H)$$

where

P is the momentum in GeV/C
T is the time in cycle in ms
$A = 4.76945$ GeV/C
$B = 4.11945$ GeV/C
$G = 0.0942478$
$H = 2.0$ ms

Mode	Res.	Harmonic			Landau		
		Total Growth	Max. Growth 1/sec	Energy MeV	Total Growth	Max. Growth 1/sec	Energy MeV
14	4	2.91E+0	9.64E+2	8798	3.33E−1	3.14E+2	8788
16	4	3.35E−1	8.10E+2	5800	6.34E−2	5.06E+2	5804
21	5	3.37E+0	9.40E+2	8379	0.00E+0	0.00E+0	
23	6	8.16E+0	4.77E+3	8012	6.74E+0	5.06E+3	8054
43	8	1.26E+1	5.58E+3	6898	5.67E+0	3.29E+3	6944
45	8	8.65E+0	5.82E+3	5860	5.27E+0	4.12E+3	5916
45	11	9.24E−1	8.54E+2	6681	0.00E+0	0.00E+0	
53	2	6.20E+0	1.24E+4	6860	9.89E+0	1.35E+4	6884

Table 4: Total growth, maximum growth rate and minimum growth rate for an assorted set of coupled bunch modes and driving resonances. Comparison is made here between harmonic and Landau cavity potentials. The detail for obtaining the total growth is described in Section 3-3. The maximum growth rates are determined according to the graphs in Figure 3-1. (Keep in mind the different units used there.) The energy values at which these happen are also listed.